

# DYNAMIC STABILITY AND PARAMETRIC RESONANCE IN CYLINDRICAL PROPELLANT TANKS

by

Daniel D. Kana  
Wen-Wha Chu  
Tom D. Dunham

## FINAL REPORT

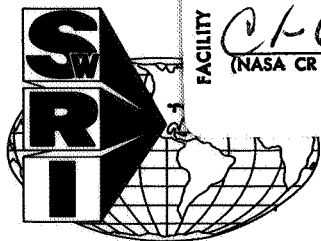
Contract No. NAS8-20329  
Control No. DCN 1-7-53-20133 (1F)  
SwRI Project No. 02-1876

Prepared for

National Aeronautics and Space Administration  
George C. Marshall Space Flight Center  
Huntsville, Alabama

17 January 1968

FACILITY FORM 602	N68-21873	
	(ACCESSION NUMBER)	(THRU)
	98	1
	(PAGES)	(CODE)
	01-61725	32
	(NASA CR OR TMX OR AD NUMBER)	(CATEGORY)



SOUTHWEST RESEARCH INSTITUTE  
SAN ANTONIO HOUSTON

SOUTHWEST RESEARCH INSTITUTE  
8500 Culebra Road, San Antonio, Texas 78228

# DYNAMIC STABILITY AND PARAMETRIC RESONANCE IN CYLINDRICAL PROPELLANT TANKS

by

Daniel D. Kana  
Wen-Wha Chu  
Tom D. Dunham

## FINAL REPORT

Contract No. NAS8-20329  
Control No. DCN 1-7-53-20133 (1F)  
SwRI Project No. 02-1876

Prepared for

National Aeronautics and Space Administration  
George C. Marshall Space Flight Center  
Huntsville, Alabama

17 January 1968



Approved:

A handwritten signature in black ink, appearing to read "H. Norman Abramson".

H. Norman Abramson, Director  
Department of Mechanical Sciences

## ABSTRACT

Dynamic stability and parametric resonance of longitudinally excited cylindrical propellant tanks are investigated to determine the significance of this form of response in launch vehicle systems. A theoretical analysis is conducted to predict the dynamic stability of a simplified model consisting of a partially liquid filled cylinder which has a rigid flat bottom, an internal ullage pressure, and a rigid top mass. Donnell equations for cylindrical shells are used to determine natural frequencies, forced axisymmetric response, and dynamic stability of the model. Numerical results are compared with experimental observations for a range of several significant parameters. Although it is found that the stability is governed by a coupled set of Mathieu-Hill equations, approximate solutions are presented which allow relatively easy determination of stability for the case of principal parametric resonance. Additional experiments are conducted for a 1/16-scale model of a Saturn-V LOX tank to determine the influence of ring stiffeners. Instabilities and many forms of nonlinear response are found to be present for tanks having less than three stiffener rings.

PRECEDING PAGE BLANK NOT FILMED.

## ACKNOWLEDGMENTS

The authors wish to express their sincere appreciation to their colleagues for help received throughout this program. Particular mention should be given to Dr. H. Norman Abramson for his counsel, Mr. Dennis C. Scheidt for conducting many of the experiments, to Mr. Robert Gonzales for computer programming, and to Mr. Victoriano Hernandez for preparing the figures.



## TABLE OF CONTENTS

	<u>Page</u>
LIST OF ILLUSTRATIONS	vii
NOTATION	ix
INTRODUCTION	1
General	1
Description of Models	2
THEORETICAL ANALYSIS	3
Shell Equations	3
Natural Frequencies of Partially-Filled Tank with Top Mass	6
Generalized Added Mass of Liquid	11
Forced Axisymmetric Response	15
Governing Equations for Dynamic Stability	20
General Formulation	20
One-Mode Approximation	25
THEORETICAL AND EXPERIMENTAL RESULTS FOR SMALL MODEL	27
Natural Frequencies of Tank with Top Mass	27
Forced Axisymmetric Response	29
Stability Boundaries	30
Nonlinear Response	32
EXPERIMENTAL RESULTS FOR LARGE MODEL WITH STIFFENERS	34
GENERAL DISCUSSION AND RECOMMENDATIONS FOR FURTHER WORK	36

## TABLE OF CONTENTS (Cont'd)

	<u>Page</u>
ILLUSTRATIONS	39
APPENDICES	71
A. Theoretical Expressions	71
B. Experimental Data for Tank A	77
C. Experimental Data for Large Model with Stiffeners	83
REFERENCES	87

## LIST OF ILLUSTRATIONS

<u>Figure</u>		<u>Page</u>
1	Coordinate System for Small Model	40
2	Dynamic Stability Apparatus for Small Model	41
3	Dynamic Stability Apparatus for Large Model	42
4	Layout of Large Tank	43
5	Configurations of Model Tanks	44
6	Natural Frequencies of Partially-Filled Tank with Top Mass	
	a. $W_0 = 34.53 \text{ lb}$	45
	b. $W_0 = 22.32 \text{ lb}$	46
	c. $W_0 = 11.48 \text{ lb}$	47
7	Effect of Top Mass on Natural Frequencies	48
8	Response of Top Mass Relative to Input Acceleration for Axisymmetric Wall Response	49
9	Influence of Liquid Depth on Stability	
	a. $h/l = 0$	50
	b. $h/l = 0.414$	51
	c. $h/l = 0.983$	52
	d. Logarithmic Plot	53
10	Influence of Ullage Pressure on Stability	
	a. $p_0 = 3 \text{ psig}$	54
	b. $p_0 = 6 \text{ psig}$	55
	c. Logarithmic Plot	56
11	Influence of Top Mass on Stability	57
12	Influence of Liquid Depth on Subharmonic Wall Response	58
13	Influence of Ullage Pressure on Subharmonic Wall Response	59
14	Influence of Top Mass on Subharmonic Wall Response	60

LIST OF ILLUSTRATIONS (Cont'd)

<u>Figure</u>		<u>Page</u>
15	Nonlinear Coupling of Tank Wall and Liquid Surface	61
16	Stability Boundaries for Tank S-0	62
17	Nonlinear Response for Tank S-0	63
18	Stability Boundaries for Tank S-1	64
19	Nonlinear Wall Response for Tank S-1	65
20	Nonlinear Response for Tank S-1	66
21	POGO Behavior in Tank S-1	67
22	Stability Boundaries for Tank S-2	68
23	Nonlinear Response for Tank S-2	69

## NOTATION

a	radius of the shell
$a_0$	inner radius of the tank
$c_0$	speed of sound in the liquid
$c_s$	$E/\rho_s$ , speed of stress waves in the shell
E	modulus of elasticity
f	excitation frequency in cps
g	standard acceleration of gravity
$g_x$	nondimensional excitation amplitude ( $\bar{x}_0\omega^2/g$ )
H	$h/a$ , nondimensional liquid depth
$H_s$	$h_s/a$ , nondimensional thickness of shell
h	depth of liquid
$h_s$	thickness of shell
$I_z$	mass moment of inertia of top weight about z axis
l	length of the shell
M	top mass
$M_s$	shell mass, $2\pi ah_s\ell\rho_s$
M**	nondimensional top mass
m	one-half of the number of circumferential nodes; $\cos(m\theta)$
$N_{xx}, N_{x\theta}, N_{\theta\theta}$	stress resultants in the shell (linearized)
$N_{xxa}, N_{\theta\theta a}$	dynamic part of initial-state stress resultants (linearized)
$N_{xxs}, N_{\theta\theta s}, N_{x\theta s}$	static part of initial-state stress resultants (linearized)

## NOTATION (Cont'd)

$n$	axial wave number; $\sin n\pi x/\ell$
$P$	nondimensional pressure, $p/E$
$P^B$	nondimensional pressure (axisymmetric) due to bottom motion in a rigid tank
$p$	pressure in the liquid
$p_0$	ullage pressure
$P_r$	pressure loading on the shell
$P_x, P_\theta$	external loads on shell in $x$ and $\theta$ direction, respectively
$Q_{0n}^B$	generalized loading due to $P^B$
$r, \theta, x$	cylindrical coordinates (space-fixed)
$t$	time
$U, V, W, X, Y$	$u, v, w, x, y$ , nondimensionalized by the radius $a$
$u, v, w$	displacements along $x, \theta, r$ direction, respectively
$w_a$	radial tank displacement at an antinode
$X_0$	nondimensional amplitude of axial excitation ( $X_0 = \hat{x}_0/a$ )
$x_0(t)$	excitation displacement
$\hat{x}_0$	displacement amplitude of axial excitation
$\lambda$	axial wavelength parameter ( $n\pi a/\ell$ )
$\nu$	Poisson's ratio
$\rho$	mass density of liquid
$\rho_s$	mass density of the shell
$\Omega$	nondimensional frequency, ( $\omega a/c_s$ )

## NOTATION (Cont'd)

$\Omega_k$	k-th eigenvalue $\omega_k a / c_s$
$\omega$	circular frequency of excitation

### Superscripts and Subscripts

$( )^c$	related to the complementary solution
$( )^p$	related to the particular solution
$( \sim )$	the amplitude of $( )$
$( \dot{\ } )$	$(d/d\tau) ( )$ , $\tau = \omega t$

# DYNAMIC STABILITY AND PARAMETRIC RESONANCE IN CYLINDRICAL PROPELLANT TANKS

By Daniel D. Kana, Wen-Hwa Chu,  
and Tom D. Dunham  
Southwest Research Institute

## INTRODUCTION

### General

Longitudinal dynamics is recognized as a very important part of the behavior of launch vehicles during flight. The interaction of liquids and their elastic containers plays a dominating role in overall vehicle response under longitudinal excitation since liquid pressures form the dominant effective masses, as well as avenues of energy feedback in a vehicle structure. As a result, the synthesis of vehicle structures into relatively simple spring-mass representations<sup>1</sup> provides only a gross approximation of vehicle response, for the overall behavior of the liquid and elastic tank can only be obtained by careful consideration of both linear and nonlinear interactions.

Various types of dynamic responses of representative vehicle-tank systems have been observed experimentally for longitudinal excitation of laboratory models, as part of the earlier effort under the present program<sup>2</sup>. For moderate and higher frequencies, three forms of response appeared to be the most significant, depending on the exact configuration of the tank and its stiffener system. Direct linear harmonic response in axisymmetric modes occurs primarily as large pressure amplifications within the liquid accompanied by very small wall responses. On the other hand, response in nonaxisymmetric modes appears in the form of relatively large harmonic wall responses accompanied by only minor pressure amplitudes. Finally, for unstiffened or lightly stiffened tanks, the dominant form of response occurs as parametric modes in which large symmetric harmonic pressure oscillations are accompanied by large-amplitude 1/2-subharmonic wall motion in nonsymmetric modes, a nonlinear response which results from instabilities in linear responses.

The first two of the above-described responses have been given considerable attention; reviews of much of the work are given in References 2 through 4. The third, nonlinear form of response has been studied only little, particularly from the launch vehicle point of view<sup>2-4</sup>. Some additional work which was recently translated from the Russian literature is given in References 5 and 6. The investigation of Bagdasaryan and Gnuni<sup>5</sup>, which deals with dynamic stability of anisotropic shells, is very closely



related to the present study for the case where the presence of stiffeners produces effective orthotropic properties in cylinders.

Dynamic instability and parametric resonance have been studied both analytically and experimentally for the case of a full tank only<sup>3, 4</sup>. On the other hand, liquid depth variations, ullage pressure, and coupled end masses were observed to exert a strong influence on the vibrational response of a propellant tank<sup>2</sup>. Therefore, the purpose of the present study is to investigate both analytically and experimentally the dynamic stability and parametric response of a longitudinally-excited, partially-filled elastic cylinder subject to both ullage pressure and a rigid top mass. To facilitate comparison between theory and experiment, results are obtained for an unstiffened, flat-bottom cylinder. Subsequent experimental results are then obtained for a more representative tank model to indicate the influence of longitudinal stiffeners and ring baffles on the dynamic instability mechanism.

### Description of Models

Most of the work herein was conducted in a liquid-tank system such as that shown in the schematic of Figure 1, where the analytical coordinate system is also defined. This configuration is designated as Tank A for the purpose of this report. A photograph of Tank A and its associated apparatus is shown in Figure 2. The tank is fabricated of 0.005-inch thick type 302 stainless steel sheet which was rolled and butt-welded along a longitudinal seam. The lower end is spot welded to a rigid flange which, in turn, is bolted to a flat, rigid base which forms the tank bottom, as well as the attachment to the electrodynamic shaker armature. The upper end is spot welded to a rigid end disk which also forms a mount for and part of the top mass. Two rows of 0.020-inch diameter spot welds are used at each end. Spots are spaced 1/8-inch apart with 1/8 inch between rows. Both ends are sealed with epoxy cement to form an airtight system. Several different annular top masses were fabricated to fit the top support. Water is used as the model liquid.

The instrumentation for Tank A, as shown in Figure 2, is essentially the same as that used for studying elastic-tank responses in the earlier work<sup>2</sup>; therefore, it will not be described here. The only different features are in the mechanical support for the tank wall displacement transducer, and these can clearly be seen in the photograph. As before, this system allows radial displacement to be monitored at all points on the tank wall.

Some additional experiments were conducted in the 1/16-scale model of the S-IC LOX tank which was fabricated earlier in the program. Complete details of this tank and its associated instrumentation system were given in the results of that work<sup>2</sup>. However, for convenience, a photograph and schematic of this tank are given in Figures 3 and 4, respectively. It may be

noted that no top mass is used with this tank. For the present purposes, it is designated as Tank S-0, S-1, etc., depending on the number of ring baffles installed. A complete schematic of all tank configurations used in the present study is given in Figure 5.

Experimental procedures used for both of the above tanks consisted of observing radial wall response and liquid pressure at the center of the tank bottom for various input accelerations and frequencies. Detailed procedures for obtaining stability boundaries, as well as nonlinear responses, are the same as in the previous work<sup>2</sup>.

## THEORETICAL ANALYSIS

Dynamic stability of the system shown in Figure 1 will be analyzed using bending theory of cylindrical shells. From earlier work, as well as preliminary experiments, it is found that instability and parametric resonance occurs in the liquid-tank system in a certain pattern. That is, first the system responds in axisymmetric linear modes which can be called the initial state. Then, under certain conditions of excitation, nonaxisymmetric perturbations which are superimposed on the initial state become unstable and, subsequently, grow into a nonlinear parametric response called the final state. The dominant form of displacement in the final state is that previously described in which the shell wall responds in a nonsymmetric 1/2-subharmonic motion referred to as the principal parametric resonance.

A detailed analytical description of the instability mechanism for a full tank has been given by Kana and Craig<sup>3, 4</sup> by the use of the perturbation method of Bolotin<sup>7</sup>. The qualitative aspects of this description also apply in the present case. Thus, if one separates the initial-state shell motion from that of the nonlinear final state, the perturbed motion remains. The analysis of only the initial state, and the perturbed motion is carried out for the present system. The formulation is logically separated into several parts, with the final part giving the equations governing dynamic stability.

### Shell Equations

Sanders<sup>8, 9</sup> has derived a set of nonlinear equations for a general shell based on the Donnell-Mushitari-Vlasov approximations. Similar equations for cylindrical shells have been given by Bieniek, et al.<sup>10</sup>. These equations provide a description of the nonlinear final-state displacements of the present system as follows:

$$\begin{aligned} \frac{\partial^2 u}{\partial x^2} + \frac{\nu}{a} \frac{\partial^2 v}{\partial x \partial \theta} + \frac{\nu}{a} \frac{\partial w}{\partial x} + \frac{1-\nu}{2a^2} \left( \frac{\partial^2 u}{\partial \theta^2} + a \frac{\partial^2 v}{\partial x \partial \theta} \right) + \frac{\partial w}{\partial x} \frac{\partial^2 w}{\partial x^2} + \frac{\nu}{a^2} \frac{\partial w}{\partial \theta} \frac{\partial^2 w}{\partial x \partial \theta} \\ + \frac{(1-\nu)}{2a^2} \left( \frac{\partial^2 w}{\partial x \partial \theta} \frac{\partial w}{\partial \theta} + \frac{\partial w}{\partial x} \frac{\partial^2 w}{\partial \theta^2} \right) = \frac{1-\nu^2}{Eh_s} \left( -p_x + \rho_s h_s \frac{\partial^2 u}{\partial t^2} \right) \end{aligned} \quad (1a)$$

$$\begin{aligned} \frac{\partial^2 v}{\partial \theta^2} + \frac{\partial w}{\partial \theta} + a\nu \frac{\partial^2 u}{\partial x \partial \theta} + a^2 \frac{(1-\nu)}{2} \left( \frac{\partial^2 v}{\partial x^2} + \frac{1}{a} \frac{\partial^2 u}{\partial x \partial \theta} \right) + \frac{1}{a} \frac{\partial w}{\partial \theta} \frac{\partial^2 w}{\partial \theta^2} \\ + a \frac{(1-\nu)}{2} \left( \frac{\partial^2 w}{\partial x^2} \frac{\partial w}{\partial \theta} + \frac{\partial w}{\partial x} \frac{\partial^2 w}{\partial x \partial \theta} \right) + a\nu \frac{\partial w}{\partial x} \frac{\partial^2 w}{\partial x \partial \theta} \\ = a^2 \frac{(1-\nu^2)}{Eh_s} \left( -p_\theta + \rho_s h_s \frac{\partial^2 v}{\partial t^2} \right) \end{aligned} \quad (1b)$$

$$\begin{aligned} -\frac{1}{a} \left\{ \frac{1}{a} \frac{\partial v}{\partial \theta} + \frac{w}{a} + \frac{1}{2a^2} \left( \frac{\partial w}{\partial \theta} \right)^2 + \nu \left[ \frac{\partial u}{\partial x} + \frac{1}{2} \left( \frac{\partial w}{\partial x} \right)^2 \right] \right\} \\ + \frac{1-\nu^2}{Eh_s} \left[ \frac{\partial}{\partial x} \left( N_{xx1} \frac{\partial w}{\partial x} \right) + \frac{1}{a} \frac{\partial}{\partial x} \left( N_{x\theta 1} \frac{\partial w}{\partial \theta} \right) + \frac{1}{a} \frac{\partial}{\partial \theta} \left( N_{x\theta 1} \frac{\partial w}{\partial x} \right) \right. \\ \left. + \frac{1}{a^2} \frac{\partial}{\partial \theta} \left( N_{\theta\theta 1} \frac{\partial w}{\partial \theta} \right) \right] - \frac{h_s^2}{12} \left[ \frac{\partial^4 w}{\partial x^4} + \frac{2}{a^2} \frac{\partial^4 w}{\partial x^2 \partial \theta^2} + \frac{1}{a^4} \frac{\partial^4 w}{\partial \theta^4} \right] \\ = \frac{1-\nu^2}{Eh_s} \left( -p_r + \rho_s h_s \frac{\partial^2 w}{\partial t^2} \right) \end{aligned} \quad (1c)$$

Further, the nonlinear forms of stress resultants are

$$N_{xx1} = \frac{Eh_s}{1-\nu^2} \left\{ \left[ \frac{\partial u}{\partial x} + \frac{1}{2} \left( \frac{\partial w}{\partial x} \right)^2 \right] + \nu \left[ \frac{1}{a} \frac{\partial v}{\partial \theta} + \frac{w}{a} + \frac{1}{2} \left( \frac{\partial w}{a\partial \theta} \right)^2 \right] \right\} \quad (2a)$$

$$N_{x\theta 1} = \frac{Eh_s}{1+\nu} \left\{ \frac{1}{2} \left( \frac{\partial u}{\partial x} + \frac{\partial v}{a\partial \theta} \right) + \frac{1}{2} \frac{\partial w}{\partial x} \frac{\partial w}{a\partial \theta} \right\} \quad (2b)$$

$$N_{\theta\theta 1} = \frac{Eh_s}{1-\nu^2} \left\{ \left[ \frac{\partial v}{a\partial \theta} + \frac{w}{a} + \frac{1}{2} \left( \frac{\partial w}{a\partial \theta} \right)^2 \right] + \nu \left[ \frac{\partial u}{\partial x} + \frac{1}{2} \left( \frac{\partial w}{\partial x} \right)^2 \right] \right\} \quad (2c)$$

Equations (1) are in agreement with Equations (7) through (9) of Bieniek, et al.,<sup>10</sup> except that  $N_{xx1}$ ,  $N_{x\theta 1}$ ,  $N_{\theta\theta 1}$  in Equation (1c) appears inside the differentiation signs. Since the radial component of force due to  $N_{xx1}$  is

$N_{xx1} (\partial w / \partial x)$ , the net radial force due to  $N_{xx1}$  is  $\partial / \partial x [N_{xx1} (\partial w / \partial x)]$  as indicated in Equation (1c).

It should be emphasized that Equations (1) contain nonlinear terms contributed by two sources. The underlined terms result from geometrical nonlinearities caused by rotations of the shell elements. This source of nonlinearity is described in detail on page 196 of Bolotin<sup>7</sup>. The remaining nonlinear terms result from the use of the nonlinear strain-displacement relations. For the present study, we will follow the philosophy of Bolotin and assume that the geometrical nonlinearities alone are sufficient for determining dynamic stability.\* As a result, the governing shell equations reduce to

$$L_{11}(u) + L_{12}(v) + L_{13}(w) = \frac{1 - \nu^2}{EH_s} \left( -p_x + \rho_s h_s \frac{\partial^2 u}{\partial t^2} \right) \quad (3a)$$

$$L_{21}(u) + L_{22}(v) + L_{23}(w) = \frac{1 - \nu^2}{EH_s} \left( -p_\theta + \rho_s h_s \frac{\partial^2 v}{\partial t^2} \right) \quad (3b)$$

$$\begin{aligned} L_{31}(u) + L_{32}(v) + L_{33}(w) - \frac{1 - \nu^2}{EH_s} \left[ \frac{\partial}{\partial x} \left( N_{xx} \frac{\partial w}{\partial x} \right) + \frac{1}{a^2} \frac{\partial}{\partial \theta} \left( N_{\theta\theta} \frac{\partial w}{\partial \theta} \right) \right. \\ \left. + \frac{1}{a} \frac{\partial}{\partial x} \left( N_{x\theta} \frac{\partial w}{\partial \theta} \right) + \frac{1}{a} \frac{\partial}{\partial \theta} \left( N_{x\theta} \frac{\partial w}{\partial x} \right) \right] \\ = - \frac{1 - \nu^2}{EH_s} \left( -p_r + \rho_s h_s \frac{\partial^2 w}{\partial t^2} \right) \end{aligned} \quad (3c)$$

where the  $L_{ij}$  are the corresponding linear operators in Equations (1), and the stress resultants  $N_{xx}$ ,  $N_{x\theta}$ ,  $N_{\theta\theta}$  are given by the corresponding linearized forms of Equations (2). Equations (3) can be used to study all aspects of the present vibration problem, so long as the details of the aforementioned perturbation process is understood.

Thus, for free vibrations, we set

$$N_{xx} = N_{xxs}, \quad N_{x\theta} = N_{x\theta s}, \quad N_{\theta\theta} = N_{\theta\theta s} \quad (4)$$

and use homogeneous boundary conditions at the base of the tank. Both symmetric and nonsymmetric natural modes can then be determined.

---

\*We emphasize, however, that to determine the character and amplitude of the subsequent nonlinear motion of the final state requires the use of the complete form of Equations (1).

For linear forced axisymmetric vibration, which comprises the initial state, we again use Equations (4) but impose a forced displacement at the base of the tank. Only a symmetric response results. The solution of this state then allows calculation of the dynamic components  $N_{xxa}$ ,  $N_{x\theta a}$ ,  $N_{\theta\theta a}$  by the use of the linearized form of Equations (2).

Finally, Equations (3) are used to determine dynamic stability of perturbed motion by setting

$$N_{xx} = N_{xxs} + N_{xxa}, \quad N_{x\theta} = N_{x\theta s} + N_{x\theta a}, \quad N_{\theta\theta} = N_{\theta\theta s} + N_{\theta\theta a} \quad (5)$$

using homogeneous boundary conditions at the base of the tank, and analyzing the stability of the resulting equations.

In all of the above cases, the shell loads  $p_x$  and  $p_\theta$  will be neglected.

### Natural Frequencies of Partially-Filled Tank with Top Mass

This section deals with vibrational modes whose radial displacements are proportional to  $\cos m\theta$ . The case of axisymmetric vibration is contained as a special case with  $m = 0$ . Expanding the axial displacement into a Fourier cosine series in  $x$  plus a quadratic polynomial to satisfy the two end conditions, and circumferential and radial displacements into Fourier sine series in  $x$ , there results

$$U = \left[ \frac{1}{2} B_2 X^2 + B_1 \left( X - \frac{\ell}{a} \right) + B_{m0} + \sum_{h=1}^{\infty} B_{mnh} \cos \left( \frac{n\pi x}{\ell} \right) \right] \cos(m\theta) \cos(\omega t) \quad (6a)$$

$$V = \sum_{n=1}^{\infty} C_{mn} \sin \left( \frac{n\pi x}{\ell} \right) \sin(m\theta) \cos(\omega t) \quad \begin{array}{l} 0 \leq x \leq \ell \\ 0 \leq \theta \leq 2\pi \end{array} \quad (6b)$$

$$W = \sum_{n=1}^{\infty} A_{mn} \sin \left( \frac{n\pi x}{\ell} \right) \cos(m\theta) \cos(\omega t) \quad (6c)$$

The boundary conditions are:

• At  $X = 0$ :

$$U = 0, \quad W = 0, \quad V = 0, \quad \frac{\partial^2 W}{\partial X^2} = 0 \quad (7 \text{ a, b, c, d})$$

• At  $X = \ell/a$ :

$$\frac{\partial U}{\partial X} = M^{**} \Omega_k^2 U, \quad W = 0, \quad V = 0, \quad \frac{\partial^2 W}{\partial X^2} = 0 \quad (7 \text{ e, f, g, h})$$

where

$$M^{**} = \frac{M(1 - \nu^2)}{2\pi\rho_s a^3 H_s} \quad \text{for } m = 0$$

$$M^{**} = \frac{1}{4} \frac{(1 - \nu^2) I_z}{\rho_s h_s a^5} \quad \text{for } m = 1$$

$$M^{**} = \infty \quad \text{for } m \geq 2$$

A very large number can be used for  $M^{**}$  when  $m \geq 2$ .

To satisfy the boundary conditions on axial displacement, one has, from Equation (7a),

$$B_1 \frac{\ell}{a} = B_{m0} + \sum_{n=1}^{\infty} B_{mn}$$

and, from Equation (7e),

$$B_2 \left(\frac{\ell}{a}\right)^2 = \frac{\left(-\frac{a}{\ell} + M^{**}\Omega_k^2\right) B_{m0} + \sum_{n=1}^{\infty} \left(-\frac{a}{\ell} + (-1)^n M^{**}\Omega_k^2\right) B_{mn}}{\frac{a}{\ell} - \frac{1}{2} M^{**}\Omega_k^2}$$

By Fourier expansion, the x-independent Fourier coefficient ( $n' = 0$ ) of the axial equation of motion (3a) yields

$$B_{m0} = \sum_{n=1}^{\infty} N_{0mn} B_{mn}$$

$$B_1 = \sum_{n=1}^{\infty} N_{1mn} B_{mn} \quad (8)$$

$$B_2 = \sum_{n=1}^{\infty} N_{2mn} B_{mn}$$

where

$$N_{0mn} = - \left\{ \left( \frac{a}{l} \right)^2 \left[ \frac{2 + (1 - \nu^2) \Omega_k^2 \chi_{20} - m^2 \frac{1 - \nu}{2} \chi_{20}}{2(1 - \nu^2) \Omega_k^2} \right] \frac{\left[ - \left( \frac{a}{l} \right) + (-1)^n M^{**} \Omega_k^2 \right]}{\left[ \frac{a}{l} - \frac{1}{2} M^{**} \Omega_k^2 \right]} \right. \\ \left. - \left( 1 - \frac{a}{l} \chi_{10} \right) \left( 1 - \frac{m^2}{2(1 + \nu) \Omega_k^2} \right) \right\} \left\{ 1 + \left( \frac{a}{l} \right)^2 \left[ \frac{-\frac{a}{l} + M^{**} \Omega_k^2}{\frac{a}{l} - \frac{1}{2} M^{**} \Omega_k^2} \right] \right. \\ \left. \left[ \frac{2 + (1 - \nu^2) \Omega_k^2 \chi_{20} - m^2 \frac{1 - \nu}{2} \chi_{20}}{2(1 - \nu^2) \Omega_k^2} \right] - \left( 1 - \frac{a}{l} \chi_{10} \right) \left( 1 - \frac{m^2}{2(1 + \nu) \Omega_k^2} \right) \right\}^{-1}$$

$$N_{1mn} = \frac{a}{l} (1 + N_{0mn})$$

$$N_{2mn} = \left( \frac{a}{l} \right)^2 \frac{\left( -\frac{a}{l} + M^{**} \Omega_k^2 \right) N_{0mn} + \left( -\frac{a}{l} + (-1)^n M^{**} \Omega_k^2 \right)}{\frac{a}{l} - \frac{1}{2} M^{**} \Omega_k^2}$$

and

$$\chi_{20} = \frac{1}{3} \left( \frac{l}{a} \right)^2, \quad \chi_{10} = \frac{1}{2} \left( \frac{l}{a} \right)$$

$$\chi_{1n} = \frac{2a}{l} \int_0^{l/a} X \cos \left( \frac{n\pi a}{l} X \right) dX$$

$$\chi_{2n} = \frac{2a}{l} \int_0^{l/a} X^2 \cos \left( \frac{n\pi a}{l} X \right) dX$$

To be used later, one can similarly define

$$\chi_{3n'n} = \frac{2a}{l} \int_0^H (H - X) \sin(\lambda_n X) \sin(\lambda_{n'} X) dX; \quad \lambda_n = \frac{n\pi a}{l}$$

Note that this term includes the effects of hydrostatic pressure.

Similarly, for  $n' > 1$ , the  $\cos(n'\pi x/l)$  coefficient of the axial Equation (3a) yields

$$\begin{aligned}
& - \sum_{n=1}^{\infty} \left( \lambda_n^2 + \frac{1-\nu}{2} m^2 \right) B_{mn} \delta_{n'n} + \sum_{n=1}^{\infty} \frac{1+\nu}{2} m \lambda_n C_{mn} \delta_{n'n} \\
& + \nu \sum_{n=1}^{\infty} \lambda_n A_{mn} \delta_{n'n} - m^2 \frac{1-\nu}{2} \sum_{n=1}^{\infty} \left( \frac{1}{2} B_2 \chi_{2n} + B_1 \chi_{1n} \right) \\
& = - (1 - \nu^2) \Omega_k^2 \left[ \frac{1}{2} \sum_{n=1}^{\infty} N_{2mn} (\Omega_k^2) \chi_{2n'} B_{mn} \right. \\
& \quad \left. + \sum_{n=1}^{\infty} N_{1mn} (\Omega_k^2) \chi_{1n'} B_{mn} + \sum_{n=1}^{\infty} B_{mn} \delta_{n'n} \right] \quad (9)
\end{aligned}$$

The  $\sin(n'\pi x/l)$  coefficient of the circumferential Equation (3b) yields

$$\begin{aligned}
& - \left\{ \frac{1+\nu}{2} m \sum_{n=1}^{\infty} (\tilde{\chi}_{1n'} N_{2mn} + \tilde{\chi}_{0n'} N_{1mn}) B_{mn} - \sum_{n=1}^{\infty} m \frac{1+\nu}{2} \lambda_n \delta_{n'n} B_{mn} \right. \\
& \quad \left. + \sum_{n=1}^{\infty} \left( \frac{1-\nu}{2} \lambda_n^2 + m^2 \right) C_{mn} \delta_{n'n} + \sum_{n=1}^{\infty} m A_{mn} \delta_{n'n} \right\} \\
& = - (1 - \nu^2) \Omega_k^2 \sum_{n=1}^{\infty} C_{mn} \delta_{n'n} \quad (10)
\end{aligned}$$

The  $\sin(n'\pi x/l)$  coefficient of the radial Equation (3c) yields

$$\begin{aligned}
& - \left\{ \nu \sum_{n=1}^{\infty} (\tilde{\chi}_{1n'} N_{2mn} + \tilde{\chi}_{0n'} N_{1mn} - \lambda_n \delta_{n'n}) B_{mn} + \sum_{n=1}^{\infty} m C_{mn} \delta_{n'n} \right. \\
& \quad + \sum_{n=1}^{\infty} \left[ 1 + \frac{H_s^2}{12} (\lambda_n^2 + m^2)^2 \right] A_{mn} \delta_{n'n} + \sum_{n=1}^{\infty} \frac{1-\nu^2}{H_s} \left[ \frac{P_0}{2E} \lambda_n^2 \right. \\
& \quad \left. + m^2 \frac{P_0}{E} \right] \delta_{n'n} + \sum_{n=1}^{\infty} \frac{\rho g a}{E} m^2 \chi_{3n'} \left. \right\} \\
& = - (1 - \nu^2) \Omega_k^2 \sum_{n=1}^{\infty} A_{mn} (\delta_{n'n} + M_{mn'}) \quad (11)
\end{aligned}$$



where, for Equations (9) through (11), we define

$$\lambda_n = \frac{n\pi a}{\ell} \quad , \quad \lambda_{n'} = \frac{n'\pi a}{\ell}$$

$$\tilde{\chi}_{1n'} = \frac{2a}{\ell} \int_0^{\ell/a} X \sin\left(\frac{n'\pi a}{\ell} X\right) dX \quad , \quad \tilde{\chi}_{0n'} = \frac{2a}{\ell} \int_0^{\ell/a} \sin\left(\frac{n'\pi a}{\ell} X\right) dX$$

and, in Equation (3c), for the added mass pressure [obtained from Equations (18) in the next section] we have used

$$P = - \sum_{n'=1}^{\infty} \sum_{n=1}^{\infty} \Omega_k^2 A_{mn} M_{mn'n} \sin\left(\frac{n'\pi a}{\ell} X\right) \cos(m\theta)$$

The effects of the ullage pressure appear in Equation (11). Thus, in the radial Equation (3c), the effect of initial tension due to the ullage pressure, the hydrostatic pressure, and top weight are included.

Equations (9) through (11) can be cast into the following matrix form

$$\left\{ \begin{array}{l} \left[ \begin{array}{ccc} [U_1] & [V_1] & [W_1] \\ [U_2] & [V_2] & [W_2] \\ [U_3] & [V_3] & [W_3] \end{array} \right] \\ \underbrace{\hspace{10em}}_{3N \times 3N} \end{array} \right\} - \tilde{\Omega}_k^2 \left\{ \begin{array}{l} \left[ \begin{array}{ccc} [R_1] & [S_1] & [T_1] \\ [R_2] & [S_2] & [T_2] \\ [R_3] & [S_3] & [T_3] \end{array} \right] \\ \underbrace{\hspace{10em}}_{3N \times 3N} \end{array} \right\} \left\{ \begin{array}{l} \{A_m\} \\ \{B_m\} \\ \{C_m\} \end{array} \right\} = 0 \quad (12)$$

where all series have been truncated to N-terms. Further,

$$\tilde{\Omega}_k^2 = (1 - \nu^2) \Omega_k^2$$

and each submatrix of the square matrices is an  $N \times N$  matrix. The submatrices of the column matrix are each a column matrix given by

$$\{A_m\} = \begin{Bmatrix} A_{m1} \\ A_{m2} \\ \vdots \\ A_{mN} \end{Bmatrix} \quad , \quad \{B_m\} = \begin{Bmatrix} B_{m1} \\ B_{m2} \\ \vdots \\ B_{mN} \end{Bmatrix} \quad , \quad \{C_m\} = \begin{Bmatrix} C_{m1} \\ C_{m2} \\ \vdots \\ C_{mN} \end{Bmatrix} \quad (13a)$$

The elements of the  $N \times N$  submatrices are given in Appendix A.1.

Natural frequencies can be determined by a trial and error method from the condition that the determinant of the coefficient matrix in Equation (12) be zero. Then, subsequently, components of the natural modes can be determined from matrix inversion of Equation (12). These components can then be normalized with respect to  $A_{m1}$  and expressed in the form

$$\begin{aligned}
 U_k &= \left[ \frac{1}{2} B_{2k} X^2 + B_{1k} \left( X - \frac{\ell}{a} \right) + B_{m0k} + \sum_{n=1}^N B_{mnk} \cos \left( \frac{n\pi x}{\ell} \right) \right] \cos m\theta \\
 V_k &= \sum_{n=1}^N C_{mnk} \sin \left( \frac{n\pi x}{\ell} \right) \sin m\theta \\
 W_k &= \sum_{n=1}^N A_{mnk} \sin \left( \frac{n\pi x}{\ell} \right) \cos m\theta
 \end{aligned} \tag{13b}$$

#### Generalized Added Mass of Liquid

For radial shell vibrations that are proportional to  $\cos m\theta$ , the liquid exerts a radial pressure which may be regarded as an apparent mass  $M_{mn}'$  which is added to the cylinder mass. We now derive an expression for this quantity.

The fluid is assumed to be nonviscous, irrotational, but compressible. The velocity potential corresponding to the  $mn$ -th component of shell motion for small disturbances is governed by the wave equation which for periodic motion is

$$\nabla^2 \phi_{mn} + \frac{\omega^2}{c_0^2} \phi_{mn} = 0$$

The boundary condition on the wall is

$$\frac{\partial \phi_{mn}}{\partial r} = \frac{\partial w_{mn}}{\partial t} \quad \text{at } r = a \text{ (} w_{mn} \text{ outward positive)} \tag{14}$$

where the  $mn$ -th component of radial shell motion is

$$w_{mn} = \tilde{A}_{mn}(t) f_n(x) \cos(m\theta) \tag{15}$$

and we assume that  $f_n(x)$  is an orthogonal set of functions in the interval  $[0, \ell]$ . The boundary condition at the bottom is:

$$\frac{\partial \phi_{mn}}{\partial x} = 0 \quad \text{at} \quad x = 0 \quad (16)$$

When frequency of excitation is much higher than the leading few liquid surface sloshing frequencies, the free surface condition can be approximated by

$$\phi_{mn} = 0 \quad \text{at} \quad x = h \quad (17)$$

By separation of variables, a particular solution can be constructed to satisfy the boundary conditions on the wetted surface [Eqs. (14) and (16)] as

$$\phi^p = \sum_{k=0}^{\infty} D_{kn} R_{mk} \left( \frac{r}{a}, \omega \right) \cos \left( \frac{k\pi x}{h} \right) \cos(m\theta) \left( a \frac{d\tilde{A}_{mn}}{dt} \right)$$

with Fourier expansion of  $f_n(x)$  being

$$f_n(x) = \sum_{k=0}^{\infty} D_{kn} \cos \left( \frac{k\pi x}{h} \right)$$

where

$$D_{kn} = \int_0^h f_n(x) \cos \left( \frac{k\pi x}{h} \right) dx \cdot \frac{2}{1 + \delta_{0n}}$$

and

$$R_{mk} = \frac{I_m \left( \xi_k \frac{r}{a} \right)}{\xi_k I'_m(\xi_k)} \quad \text{for} \quad k \geq \frac{\omega h}{\pi c_0}$$

$$R_{mk} = \frac{J_m \left( \xi_k \frac{r}{a} \right)}{\xi_k J'_m(\xi_k)} \quad \text{for} \quad k \leq \frac{\omega h}{\pi c_0}$$

where

$$\xi_k = \left[ \left( \frac{k\pi a}{h} \right)^2 - \frac{\omega^2 a^2}{c_0^2} \right]^{\frac{1}{2}}$$

One can then add a complementary solution, satisfying homogeneous boundary conditions on the wetted surfaces so that the net velocity potential satisfies the approximate free-surface condition:

$$\phi^c = \left[ \sum_{j=1}^{\infty} \tilde{B}_{mjn} J_m \left( \mu_{mj} \frac{r}{a} \right) C_j \left( \frac{x}{a}, \omega \right) \cos(m\theta) + \delta_{m0} \tilde{B}_{00n} \cos \left( \frac{\omega a}{c_0} \frac{x}{a} \right) \right] \left( -a \frac{d\tilde{A}_{mn}}{dt} \right)$$

where

$\mu_{mj}$  is the  $j$ -th root of  $J'_m(\mu_{mj}) = 0$

$$C_j \left( \frac{x}{a}, \omega \right) = \cosh \left( \eta_{mj} \frac{x}{a} \right) \quad \text{for} \quad \mu_{mj} \geq \frac{\omega a}{c_0}$$

and

$$C_j \left( \frac{x}{a}, \omega \right) = \cos \left( \eta_{mj} \frac{x}{a} \right) \quad \text{for} \quad \mu_{mj} < \frac{\omega a}{c_0}$$

where

$$\eta_{mj} = \left[ \left| \mu_{mj}^2 - \frac{\omega^2 a^2}{c_0^2} \right| \right]^{\frac{1}{2}}$$

$$E_{kj} = \frac{\int_0^1 \frac{r}{a} R_{mk} \left( \frac{r}{a}, \omega \right) J_m \left( \mu_{mj} \frac{r}{a} \right) d \left( \frac{r}{a} \right)}{\int_0^1 \frac{r}{a} J_m^2 \left( \mu_{mj} \frac{r}{a} \right) d \left( \frac{r}{a} \right)}$$

$$E_{k0} = 2 \int_0^1 \frac{r}{a} R_{0k} \left( \frac{r}{a}, \omega \right) d \left( \frac{r}{a} \right)$$

$$\tilde{B}_{mjn} = \frac{\sum_{k=0}^{\infty} (-1)^k D_{kn} E_{kj}}{C_j \left( \frac{h}{a}, \omega \right)}$$

$$\tilde{B}_{00n} = \frac{\sum_{k=0}^{\infty} (-1)^k D_{kn} E_{k0}}{\cos\left(\frac{\omega h}{c_0}\right)}$$

The linearized pressure is given by the Bernoulli equation:

$$p_{mn} = -\rho \frac{\partial \phi_{mn}}{\partial t}$$

The  $n'$ -th component of generalized force is given by integration of the loading with a weighting function  $f_{n'}(x)$ :

$$\frac{q_{mn'n}}{\rho_s h_s} = \frac{1}{\rho_s h_s} \int_0^l f_{n'}(x) p_{mnd} dx$$

from which the generalized apparent mass can be shown as

$$M_{mn'n} = \frac{\rho a}{\rho_s h_s} \left\{ \sum_{k=1}^{\infty} R_{mk}(1, \omega) D_{kn} \tilde{D}_{kn'} - \left[ \sum_{k=1}^{\infty} E_{k0} D_{kn} (-1)^k \tilde{E}_{n'} \delta_{0m} / \cos\left(\frac{\omega h}{c_0}\right) \right] + \left[ \frac{2}{\xi_0^2} \frac{\tilde{E}_{n'}}{\cos\frac{\omega h}{c_0}} - \frac{J_0(\xi_0)}{\xi_0 J_1(\xi_0)} \tilde{D}_{0n'} \right] D_{0n} \delta_{m0} + (1 - \delta_{m0}) \left[ D_{0n} \tilde{D}_{0n'} \cdot \frac{J_m(\xi_0)}{\xi_0 J'_m(\xi_0)} \right] - \sum_{j=1}^{\infty} J_m(\mu_{mj}) \tilde{C}_{nj} \tilde{B}_{mjn} \right\} \quad (18a)$$

in which

$$\tilde{D}_{kn'} = \frac{\int_0^h \cos\left(\frac{k\pi x}{h}\right) f_{n'}(x) dx}{\int_0^l f_{n'}^2(x) dx}$$

$$\tilde{C}_{n'j} = \frac{\int_0^h C_j\left(\frac{x}{a}, \omega\right) f_{n'}(x) dx}{\int_0^{\ell} f_{n'}^2(x) dx}$$

$$\tilde{E}_{n'} = \frac{\int_0^h \cos\left(\frac{\omega x}{c_0}\right) f_{n'}(x) dx}{\int_0^{\ell} f_{n'}^2(x) dx} = \tilde{D}_{0n'}$$

Note then that the mn-th component of pressure is

$$p = P_{mn} = \sum_{n'=1}^N \rho_s h_s M_{mn'n} \cos(m\theta) f_{n'}(x) \frac{d^2 \tilde{A}_{mn}}{dt^2} \quad (18b)$$

Thus,  $M_{mn'n}$  is the coefficient of  $(d^2/dt^2) (\tilde{A}_{mn})$  in the  $n'$ -th component of shell motion exhibiting a  $\cos(m\theta)$  mode of vibration. To use this generalized coefficient in Equation (11), we note from Equation (6c) that  $f_n(x)$  assumes the form

$$f_n(x) = \sin\left(\frac{n\pi x}{\ell}\right)$$

#### Forced Axisymmetric Response

Now, assume the tank is excited axially. The same shell displacement forms [Eqs. (6)] are again used. The boundary conditions on axial displacement become

$$\text{At } X = 0, \quad U = -X_0 \cos(\omega t) \quad (19)$$

$$\text{At } X = \frac{\ell}{a}, \quad \frac{\partial U}{\partial X} = M^{**} \Omega^2 U \quad (20)$$

To satisfy these conditions\*, one has, from Equation (6a):

\* $m = 0$  is assumed throughout this section. Further, superscript p designates particular solutions.

$$B_1 \frac{\ell}{a} = X_0 + B_{m0} + \sum_{n=1}^{\infty} B_{mn}$$

$$B_2 \left(\frac{\ell}{a}\right)^2 = \frac{\left(-\frac{a}{\ell} + M^{**}\Omega^2\right) B_{m0} + \sum_{n=1}^{\infty} \left(-\frac{a}{\ell} + (-1)^n M^{**}\Omega^2\right) B_{mn} - \frac{a}{\ell} X_0}{\frac{a}{\ell} - \frac{1}{2} M^{**}\Omega^2}$$

A Fourier method similar to that in the previous section is now utilized. Thus, the x-independent Fourier coefficient ( $n' = 0$ ) of Equation (3a) yields

$$B_{m0} = -\frac{2 + (1 - \nu^2) \Omega^2 \chi_{20} - m^2 \frac{1 - \nu}{2} \chi_{20}}{2(1 - \nu^2) \Omega^2} B_2 + \left(\frac{\ell}{a} - \chi_{10}\right) \left(1 - \frac{m^2}{2(1 + \nu) \Omega^2}\right) B_1$$

After collecting  $B_{m0}$  terms, one finds

$$B_{m0} = \sum_{n=1}^{\infty} N_{0mn}(\Omega) B_{mn} + X_{m0} X_0,$$

$$B_1 = \sum_{n=1}^{\infty} N_{1mn}(\Omega) B_{mn} + X_{m1} X_0, \quad B_2 = \sum_{n=1}^{\infty} N_{2mn}(\Omega) B_{mn} + X_{m2} X_0$$

$$N_{0mn}(\Omega) = [N_{0mn}(\Omega_k)]_{\Omega_k = \Omega}, \quad N_{1mn}(\Omega) = [N_{1mn}(\Omega_k)]_{\Omega_k = \Omega},$$

$$N_{2mn}(\Omega) = [N_{2mn}(\Omega_k)]_{\Omega_k = \Omega},$$

$$\begin{aligned} X_{m0} = & \left\{ \left(\frac{a}{\ell}\right)^2 \left( \frac{2 + (1 - \nu^2) \Omega^2 \chi_{20} - m^2 \frac{1 - \nu}{2} \chi_{20}}{2(1 - \nu^2) \Omega^2} \right) \frac{\left(\frac{a}{\ell}\right)}{\left(\frac{a}{\ell} - \frac{1}{2} M^{**}\Omega^2\right)} \right. \\ & \left. + \left(1 - \frac{a}{\ell} \chi_{10}\right) \left(1 - \frac{m^2}{2(1 + \nu) \Omega^2}\right) \right\} / \left\{ 1 + \right. \\ & \left. + \left( \frac{2 + (1 - \nu^2) \Omega^2 \chi_{20} - m^2 \frac{1 - \nu}{2} \chi_{20}}{2(1 - \nu^2) \Omega^2} \right) \left(\frac{a}{\ell}\right)^2 \left( \frac{-\frac{a}{\ell} + M^{**}\Omega^2}{\frac{a}{\ell} - \frac{1}{2} M^{**}\Omega^2} \right) \right. \\ & \left. - \left(1 - \frac{a}{\ell} \chi_{10}\right) \left(1 - \frac{m^2}{2(1 + \nu) \Omega^2}\right) \right\} \end{aligned}$$

$$X_{m1} = \frac{a}{\ell} (1 + X_{m0}) , \quad X_{m2} = \left(\frac{a}{\ell}\right)^2 \left[ \frac{-\left(\frac{a}{\ell}\right)}{\frac{a}{\ell} - \frac{1}{2} M^{**} \Omega^2} + \frac{\left(-\frac{a}{\ell} + M^{**} \Omega^2\right)}{\left(\frac{a}{\ell} - \frac{1}{2} M^{**} \Omega^2\right)} X_{m0} \right]$$

For  $n' \geq 1$ , the axial Equation (3a) yields

$$\begin{aligned} & - \sum_{n=1}^{\infty} \left( \lambda_n^2 + \frac{1-\nu}{2} m^2 \right) B_{mn} \delta_{n'n} + \sum_{n=1}^{\infty} \nu \lambda_n A_{mn} \delta_{n'n} \\ & + \sum_{n=1}^{\infty} \frac{1+\nu}{2} m \lambda_n C_{mn} \delta_{n'n} - m^2 \frac{1-\nu}{2} \left( \frac{1}{2} B_2 \chi_{2n} + B_1 \chi_{1n} \right) \\ & = - (1 - \nu^2) \Omega^2 \left[ \sum_{n=0}^{\infty} \left( \frac{1}{2} B_2 \chi_{2n} + B_1 \chi_{1n} \right) \delta_{n'n} - B_1 \frac{\ell}{a} \delta_{0n'} \right. \\ & \quad \left. + B_{m0} \delta_{0n'} + \sum_{n=1}^{\infty} B_{mn} \delta_{n'n} \right] \quad (21) \end{aligned}$$

The circumferential Equation (3b) yields

$$\begin{aligned} & - m^2 \sum_{n=1}^{\infty} C_{m0} \delta_{n'n} - \sum_{n=1}^{\infty} A_{mn} m \delta_{n'n} - m \frac{1+\nu}{2} \left[ B_2 \tilde{\chi}_{1n'} + B_1 \tilde{\chi}_{0n'} + \right. \\ & \quad \left. + \sum_{n=1}^{\infty} (-\lambda_n) B_{mn} \delta_{n'n} \right] + \frac{1-\nu}{2} \sum_{n=1}^{\infty} (-\lambda_n^2) C_{mn} \delta_{n'n} \\ & = - (1 - \nu^2) \Omega^2 \sum_{n=1}^{\infty} C_{mn} \delta_{n'n} \quad (22) \end{aligned}$$

Finally, the radial Equation (3c), along with Equations (18), yields:



$$\begin{aligned}
& - \nu \left[ B_2 \tilde{\chi}_{1n'} + B_1 \tilde{\chi}_{0n'} - \sum_{n=1}^{\infty} \lambda_n B_{mn} \delta_{n'n} \right] - \sum_{n=1}^{\infty} m C_{mn} \delta_{n'n} \\
& - \sum_{n=1}^{\infty} A_{mn} \delta_{n'n} + \frac{1-\nu^2}{H_s} \left\{ \sum_{n=1}^{\infty} (-\lambda_n^2) A_{mn} \left[ \frac{P_0}{2E} - \frac{Mg}{2\pi a^2 E} \right] \delta_{n'n} \right. \\
& \left. - \sum_{n=1}^{\infty} (m^2) \frac{P_0}{E} A_{mn} \delta_{n'n} - \sum_{n=1}^{\infty} (m^2) \frac{\rho g a}{E} \chi_{3n'n} A_{mn} \right\} \\
& - \frac{H_s^2}{12} \sum_{n=1}^{\infty} (\lambda_n^2 + m^2)^2 A_{mn} \delta_{n'n} = - (1 - \nu^2) \Omega^2 \left[ \sum_{n=1}^{\infty} A_{mn} \delta_{n'n} \right. \\
& \left. + \sum_{n=1}^{\infty} M_{mn'n} A_{mn} \right] - (1 - \nu^2) \hat{Q}_{0n'}^B \quad (23)
\end{aligned}$$

Coefficients for Equations (21) through (23) are given in Appendix A. 2.

As a result of the axial motion of the tank bottom, the liquid exerts a generalized radial pressure  $q_{0n}^B$  on the tank wall. This pressure can be derived from a one-dimensional velocity potential which satisfies the wave equation along with the boundary conditions

$$\phi^B = 0 \quad \text{at} \quad x = h$$

$$\frac{\partial \phi^B}{\partial x} = \hat{x}_0 \omega \sin \omega t \quad \text{at} \quad x = 0$$

The velocity potential which satisfies these conditions can be found as

$$\phi^B = \frac{-\omega \hat{x}_0 \sin \omega t \sin \left[ \frac{\omega}{c_0} (h - x) \right]}{\frac{\omega}{c_0} \cos \left( \frac{\omega h}{c_0} \right)}$$

Thus, the generalized loading (which results from the application of the Fourier process) relative to the  $n'$ -th tank-displacement component can be expressed as:

$$Q_{0n'}^B = \frac{q_{0n'}^B}{EH_s} = \frac{1}{\alpha_{n'}^2} \int_0^h \frac{\rho \omega^2 \hat{x}_0 \cos(\omega t) \sin\left(\frac{\omega}{c_0}(h-x)\right) f_{n'}(X)}{EH_s \frac{\omega}{c_0} \cos\left(\frac{\omega h}{c_0}\right)} \frac{dx}{a}$$

where

$$\alpha_{n'}^2 = \frac{1}{2} \frac{\ell}{a}$$

The amplitude of this loading becomes

$$\hat{Q}_{0n'}^B = \frac{1}{\alpha_{n'}^2} \frac{\rho a}{\rho_s h_s} \Omega \cdot \left(\frac{c_0}{c_s}\right) \frac{I_{0n'}}{\cos\left(\Omega H \frac{c_s}{c_0}\right)} \quad (24)$$

where we define

$$I_{0n'} = \frac{1}{\alpha_{n'}^2} \int_0^H \sin\left[\frac{\omega a}{c_0}(H-X)\right] \sin(\lambda_{n'} X) dX ; \quad \lambda_{n'} = \frac{n' \pi a}{\ell}$$

In matrix form, for N-term series expressions it follows that

$$\{[\tilde{U}] - \tilde{\Omega}^2 [\tilde{R}]\} \{\hat{A}^P\} = \{\hat{F}\} ; \quad \tilde{\Omega}^2 = (1 - \nu^2) \Omega^2 \quad (25)$$

where

$$[\tilde{U}] = \left\{ \begin{array}{l} [U_1] [V_1] [W_1] \\ [U_2] [V_2] [W_2] \\ [U_3] [V_3] [W_3] \end{array} \right\}_{m=0}^{\Omega_k \rightarrow \Omega}, \quad [\tilde{R}] = \left\{ \begin{array}{l} [R_1] [S_1] [T_1] \\ [R_2] [S_2] [T_2] \\ [R_3] [S_3] [T_3] \end{array} \right\} \quad (26 \text{ a, b})$$

Each of these is a  $3N \times 3N$  square matrix whose nine elements are each  $N \times N$  square submatrices. The submatrices are the same as those appearing in Equation (12), the elements of which are given in Appendix A.1. Also

$$\{\hat{A}^P\} = \left\{ \begin{array}{l} [\hat{A}_m^P] \\ [\hat{B}_m^P] \\ [\hat{C}_m^P] \end{array} \right\}_{m=0}^{\infty}, \quad \{\hat{F}\} = \left\{ \begin{array}{l} [\hat{F}_r] \\ [\hat{F}_a] \\ [\hat{F}_c] \end{array} \right\} \quad (27 \text{ a, b})$$

Each of these is a  $3N \times 1$  column matrix whose three elements are each  $N \times 1$  column submatrices. Elements of the submatrices of Equations (27) are given in Appendix A.3. The elements are different from those of Equations (13a) since Equations (25a) represent displacements for forced oscillation (i. e., particular solution).

The amplitude of the force response is determined by the inversion of Equation (25); i. e.,

$$\{\hat{A}^P\} = \{[\tilde{U}] - \tilde{\Omega}^2 [\tilde{R}]\}^{-1} \{\hat{F}\} \quad (28)$$

### Governing Equations for Dynamic Stability

General Formulation. - We now expand the shell displacements in terms of the natural modes determined by Equations (13b). The displacements, therefore, are

$$U \cong \sum_{k=1}^{3N} a_k(\tau) \left[ \frac{1}{2} B_{2k} X^2 + B_{1k} \left( X - \frac{\ell}{a} \right) + B_{m0k} + \sum_{n=1}^N B_{mnk} \cos \frac{n\pi x}{\ell} \right] \cos(m\theta) \quad (29)$$

$$V \cong \sum_{k=1}^{3N} a_k(\tau) \sum_{n=1}^N C_{mnk} \sin \left( \frac{n\pi x}{\ell} \right) \sin(m\theta)$$

$$W \cong \sum_{k=1}^{3N} a_k(\tau) \sum_{n=1}^N A_{mnk} \sin \left( \frac{n\pi x}{\ell} \right) \cos(m\theta)$$

For the present study, the stability of nonsymmetric ( $m \geq 2$ ) responses only will be investigated. Again, using a Fourier\* procedure as in the previous sections, the  $n' = 0$  component of the axial Equation (3a) yields

$$\sum_{k=1}^{3N} a_k B_{2k} = \sum_{k=1}^{3N} (1 - \nu^2) \ddot{a}_k \Omega^2 \left[ \frac{1}{2} B_{2k} X_{20} + B_{1k} X_{10} + B_{m0k} - \frac{\ell}{a} B_{1k} \right]$$

and, using Equations (8) and (9), this reduces to

$$\sum_{k=1}^{3N} (1 - \nu^2) (\ddot{a}_k \Omega^2 + \Omega_k^2 a_k) \left[ \frac{1}{2} B_{2k} X_{20} + B_{1k} X_{10} + B_{m0k} - \frac{\ell}{a} B_{1k} \right] = 0 \quad (30)$$

\*Note that the standard Galerkin procedure could also be used here, since the coordinate functions (13b) satisfy all boundary conditions.

The  $n' \geq 1$  component of the axial Equation (3a) yields

$$\begin{aligned} \sum_{k=1}^{3N} a_k \sum_{n=1}^N - \left( \lambda_n^2 + \frac{1-\nu}{2} m^2 \right) B_{mnk} \delta_{n'n} + \frac{1+\nu}{2} m \lambda_m C_{mnk} \delta_{n'n} \\ + \nu \lambda_n A_{mnk} \delta_{n'n} = \sum_{k=1}^{3N} (1 - \nu^2) \ddot{a}_k \Omega^2 \sum_{n=1}^N \left[ \frac{1}{2} B_{2k} \chi_{2n'} \right. \\ \left. + B_{1k} \chi_{1n'} + B_{mnk} \delta_{n'n} \right] \end{aligned}$$

and, using Equations (8) and (9), this reduces to

$$\sum_{k=1}^{3N} \left\{ (1 - \nu^2) (\ddot{a}_k \Omega^2 + \Omega_k^2 a_k) \sum_{n=1}^N \left[ \frac{1}{2} B_{2k} \chi_{2n'} + B_{1k} \chi_{1n'} + B_{mnk} \delta_{n'n} \right] \right\} = 0 \quad (31)$$

The circumferential Equation (3b) yields

$$\begin{aligned} \sum_{k=1}^{3N} a_k \left\{ - \frac{1+\nu}{2} m (B_{2k} \tilde{\chi}_{1n'} + B_{1k} \tilde{\chi}_{0n'}) - \sum_{n=1}^N m \lambda_n \frac{1+\nu}{2} B_{mnk} \delta_{n'n} \right. \\ \left. + \sum_{n=1}^N \left( \frac{1-\nu^2}{2} \lambda_n^2 + m^2 \right) C_{mnk} \delta_{n'n} + \sum_{n=1}^N m A_{mnk} \delta_{n'n} \right\} \\ = \sum_{k=1}^{3N} \left\{ (1 - \nu^2) \ddot{a}_k \sum_{n=1}^N C_{mnk} \delta_{n'n} \right\} \end{aligned}$$

and, using Equations (8) and (10), this reduces to

$$\sum_{k=1}^{3N} \left\{ (1 - \nu^2) (\Omega_k^2 \ddot{a}_k + \Omega_k^2 a_k) \sum_{n=1}^N C_{mnk} \delta_{n'n} \right\} = 0 \quad (32)$$

Finally, the radial Equation (3c), along with Equations (18), yields:

$$\begin{aligned}
& \sum_{k=1}^{3N} a_k \left\{ \sum_{n=1}^N \nu (B_{2k} \tilde{\chi}_{1n'} + B_{1k} \tilde{\chi}_{0n'} - \lambda_n \delta_{n'n}) B_{mnk} + \sum_{n=1}^N m C_{mnk} \delta_{n'n} \right. \\
& + \sum_{n=1}^N \left[ 1 + \frac{H_s^2}{12} (\lambda_n^4 + 2\lambda_n^2 m^2 + m^4) \right] A_{mnk} \delta_{n'n} \\
& + \frac{(1-\nu^2)}{H_s} \sum_{n=1}^N \left[ \frac{p_0}{E} \left( \frac{1}{2} \lambda_n^2 + m^2 \right) \delta_{n'n} + \frac{\rho g a}{E} m^2 \chi_{3n'n} \delta_{n'n} \right. \\
& - \left. \frac{Mg}{2\pi a^2 E} \lambda_n^2 \delta_{n'n} \right] A_{mnk} \left. \right\} + \sum_{k=1}^{3N} a_k \sum_{n=1}^N \left\{ \left[ \lambda_n^2 \sum_{n''=1}^N N_{1n''} \right. \right. \\
& + \left. \lambda_n \sum_{n''=1}^N N_{3n''} \frac{e_{n''n'n}}{d_{n''n'n}} + m^2 \sum_{n''=1}^N N_{2n''} \right] d_{n''n'n} \\
& + \left. \lambda_n \overset{p}{B}_2 e_{0n'n} \right\} A_{mnk} X_0 \cos(\omega t) = (1-\nu^2) \ddot{a}_k \Omega^2 \sum_{n=1}^N [\delta_{n'n} \\
& + M_{mn'n}(\Omega)] A_{mnk}
\end{aligned}$$

Then, in view of Equations (8) and (9), this reduces to

$$\begin{aligned}
& \sum_{k=1}^{3N} \left\{ (1-\nu^2) \left[ \ddot{a}_k \Omega^2 \sum_{n=1}^N [\delta_{n'n} + M_{mn'n}(\Omega)] A_{mnk} \right. \right. \\
& + \left. \left. a_k \Omega_k^2 \sum_{n=1}^N [\delta_{n'n} + M_{mn'n}(\Omega_k)] A_{mnk} \right] - a_k \sum_{n=1}^N T_{n'nk} X_0 \cos(\omega t) \right\} \\
& = 0 \quad (33)
\end{aligned}$$

where the tension terms are

$$\begin{aligned}
T_{n'nk} = & \left\{ \left[ \sum_{n''=1}^N \left( \lambda_n^2 N_{1n''} + \lambda_n N_{3n''} \frac{e_{n''n'n}}{d_{n''n'n}} + m^2 N_{2n''} \right) d_{n''n'n} \right. \right. \\
& \left. \left. + \lambda_n \overset{p}{B}_2 e_{0n'n} \right] A_{mnk} \right\} \quad (34)
\end{aligned}$$

along with

$$d_{n''n'n} = \frac{1}{a^2} \int_0^{\ell/a} \sin(\lambda_n X) \sin(\lambda_{n'} X) \sin(\lambda_{n''} X) dX ;$$

$$e_{n''n'n} = \frac{1}{a^2} \int_0^{\ell/a} \cos(\lambda_{n''} X) \cos(\lambda_n X) \sin(\lambda_{n'} X) dX$$

Additional coefficients in expression (34) are now considered. To derive the initial-state dynamic stress resultants, consider the particular axisymmetric ( $m = 0$ ) solution due to axial excitation, with the following components of displacement:

$$\hat{W}_0^p = \sum_{n=1}^{\infty} \hat{A}_{mn}^p \sin(\lambda_n X) \quad (35a)$$

$$\hat{U}_0^p = \frac{1}{2} \hat{B}_2^p X^2 + \hat{B}_1^p \left( X - \frac{\ell}{a} \right) + \hat{B}_{m0}^p + \sum_{n=1}^{\infty} \hat{B}_{mn}^p \cos(\lambda_n X) \quad (35b)$$

These displacements are obtained from Equation (27a) after solving Equation (28). The dynamic initial-state stress resultants are then obtained by substituting Equations (35) into the linearized form of Equations (2). For the axial dynamic component, there results

$$\hat{N}_{xxa} = \frac{Eh_s}{1 - \nu^2} \sum_{n''=1}^{\infty} [\hat{B}_2^p \tilde{\chi}_{1n''} + \hat{B}_1^p \tilde{\chi}_{0n''} - \hat{B}_{mn''}^p \lambda_n + \nu \hat{A}_{mn''}^p] \sin(\lambda_{n''} X)$$

which, for convenience, can be expressed as

$$\hat{N}_{xxa}^* = \frac{\hat{N}_{xxa} (1 - \nu^2)}{Eh_s} = \sum_{n''=1}^{\infty} N_{1n''} \sin(\lambda_{n''} X)$$

Thus,

$$N_{1n''} = \hat{B}_2^p \tilde{\chi}_{1n''} + \hat{B}_1^p \tilde{\chi}_{0n''} - \lambda_{n''} \hat{B}_{mn''}^p + \nu \hat{A}_{mn''}^p \quad (36)$$

The derivative of the axial dynamic component of the initial-state stress resultant is:

$$\frac{\partial \hat{N}_{xxa}}{\partial X} = \frac{Eh_s}{1-\nu^2} \left\{ \hat{B}_2^p + \sum_{n''=1}^{\infty} [(-\lambda_{n''}^2) \hat{B}_{mn''}^p \cos(\lambda_{n''}X) + \nu \lambda_{n''} \hat{A}_{mn''}^p \cos(\lambda_{n''}X)] \right\}$$

or

$$\frac{\partial \hat{N}_{xxa}}{\partial X} \frac{1-\nu^2}{Eh_s} = \frac{\partial \hat{N}_{xxa}^*}{\partial X} = \sum_{n''=1}^{\infty} N_{3n''} \cos(\lambda_{n''}X) + \hat{B}_2^p$$

Thus,

$$N_{3n''} = -\lambda_{n''}^2 \hat{B}_{mn''}^p + \nu \lambda_{n''} \hat{A}_{mn''}^p, \quad n'' \geq 1 \quad (37)$$

Finally, the circumferential dynamic component of the initial-state stress resultant is

$$\hat{N}_{\theta\theta a} = \frac{Eh_s}{1-\nu^2} \left\{ \sum_{n''=1}^{\infty} \hat{A}_{mn''}^p \sin(\lambda_{n''}X) + \nu \sum_{n=1}^{\infty} (\hat{B}_2^p \tilde{\chi}_{1n''} + \hat{B}_1^p \tilde{\chi}_{0n''} - \lambda_{n''} \hat{B}_{mn''}^p) \sin(\lambda_{n''}X) \right\}$$

or

$$\hat{N}_{\theta\theta a}^* = \frac{\hat{N}_{\theta\theta a} (1-\nu^2)}{Eh_s} = \sum_{n''=1}^{\infty} N_{2n''} \sin(\lambda_{n''}X)$$

Therefore,

$$N_{2n''} = \hat{A}_{mn''}^p + \nu [\hat{B}_2^p \tilde{\chi}_{1n''} + \hat{B}_1^p \tilde{\chi}_{0n''} - \lambda_{n''} \hat{B}_{mn''}^p] \quad (38)$$

Equations (36) through (38) have been used in Equation (33).

Equations (31) through (33) are the governing equations for dynamic stability of nonsymmetric modes ( $m \geq 2$ ) of the present system. By using  $N$ -term finite series approximations throughout, these equations can be written in a more compact matrix form as

$$\begin{bmatrix} \tilde{M} \\ 3N \times 3N \end{bmatrix} \begin{Bmatrix} \ddot{a} \\ 3N \times 1 \end{Bmatrix} + \begin{bmatrix} \tilde{K} \\ 3N \times 3N \end{bmatrix} \begin{Bmatrix} a \\ 3N \times 1 \end{Bmatrix} - \begin{bmatrix} \tilde{T} \\ 3N \times 3N \end{bmatrix} X_0 \cos(\omega t) \begin{Bmatrix} a \\ 3N \times 1 \end{Bmatrix} = 0 \quad (39)$$

where the  $3N \times 3N$  matrices are of the form:

$$[\tilde{M}] = \begin{bmatrix} [M_1] \\ [M_2] \\ [M_3] \end{bmatrix}, \quad [\tilde{K}] = \begin{bmatrix} [K_1] \\ [K_2] \\ [K_3] \end{bmatrix}, \quad [\tilde{T}] = \begin{bmatrix} [T_1] \\ [T_2] \\ [T_3] \end{bmatrix} \quad (40)$$

and each submatrix is an  $N \times 3N$  matrix. The elements of these submatrices are given in Appendix A.4. The remaining column matrices are

$$\{\ddot{a}\} = \begin{Bmatrix} \ddot{a}_1 \\ \ddot{a}_2 \\ \vdots \\ \ddot{a}_{3N} \end{Bmatrix}, \quad \{a\} = \begin{Bmatrix} a_1 \\ a_2 \\ \vdots \\ a_{3N} \end{Bmatrix}$$

whose elements are the time-dependent parts of the  $k = 1$  to  $3N$  eigenvectors. Equation (39) can be solved by the method given in Meadows<sup>11</sup>. However, this method requires a lengthy computer program. As an alternative, we resort to a one-mode approximation.

One-Mode Approximation. - An approximation using one mode\* of the eigenvector expansions (29) can be reduced directly from Equation (39). However, to allow a more lucid description, we repeat the procedure of the previous section as it applies to the one-mode case. The shell displacements are taken as

$$U_k = a_k(\tau) \left[ \frac{1}{2} B_{2k} X^2 + B_{1k} \left( X - \frac{\ell}{a} \right) + B_{m0k} + \sum_{n=1}^N B_{mnk} \cos \frac{n\pi x}{\ell} \right] \cos m\theta \quad (41a)$$

$$V_k = a_k(\tau) \sum_{n=1}^N C_{mnk} \sin \frac{n\pi x}{\ell} \sin m\theta \quad (41b)$$

$$W_k = a_k(\tau) \sum_{n=1}^N A_{mnk} \sin \frac{n\pi x}{\ell} \cos m\theta \quad (41c)$$

From these expressions, it is clear that the one-mode approximation refers to the eigenvectors and not to the coordinate functions themselves.

To form an equation governing the dynamic stability of the  $k$ -th eigenvector corresponding to dominantly radial motion, we substitute Equations (41) into Equation (3c) only and, simultaneously, utilize Equations (18) for the apparent mass term, as well as Equations (8)

\*Note that "one mode expansion" or "single eigenvector expansion" is synonymous.



through (11) to eliminate the coefficients of  $U_k$  and  $V_k$ . There results a single equation in terms of the coefficients  $A_{mnk}$  of  $W_k$ . Finally, to this equation is applied the Galerkin procedure with respect to the radial component (41c) of the  $k$ -th eigenvector. There results

$$\begin{aligned} \sum_{s=1}^N A_{ms_k} A_{ms_k} (\tilde{\Omega}^2 \ddot{a}_k + \tilde{\Omega}_k^2 a_k) + \sum_{s=1}^N \sum_{n=1}^N A_{mn_k} A_{ms_k} M_{msn}(\Omega) \tilde{\Omega}^2 \ddot{a}_k \\ + \tilde{\Omega}_k^2 a_k \sum_{s=1}^N \sum_{n=1}^N A_{mn_k} A_{ms_k} M_{msn}(\Omega_k) \\ - a_k \sum_{s=1}^N \sum_{n=1}^N A_{ms_k} T_{sn_k} X_0 \cos(\omega t) = 0 \end{aligned}$$

It may be noted that the above procedure implies that the axial Equation (3a) and circumferential Equation (3b) are approximately satisfied since axial and circumferential displacements are small for the dominantly radial mode (eigenvector).

Changing the subscripts to  $n'$  and rewriting this equation, one has

$$\bar{M} \ddot{a}_k + \bar{K} a_k - \bar{T} X_0 \cos(\omega t) a_k = 0 \quad (42)$$

where the scalar coefficients are

$$\bar{M} = \tilde{\Omega}^2 \sum_{n'=1}^N \left[ A_{mn'_k}^2 + A_{mn'_k} \sum_{n=1}^N A_{mn_k} M_{mn'n}(\Omega) \right]$$

$$\bar{K} = \tilde{\Omega}_k^2 \sum_{n'=1}^N \left[ A_{mn'_k}^2 + A_{mn'_k} \sum_{n=1}^N A_{mn_k} M_{mn'n}(\Omega_k) \right]$$

$$\bar{T} = \sum_{n'=1}^N \sum_{n=1}^N T_{n'n_k} A_{mn'_k}$$

Equation (42) is a Mathieu equation of well-known stability properties. In order to put the above equation in standard form, let

$$z = \frac{1}{2} \tau, \quad \bar{a} = \frac{4\bar{K}}{\bar{M}}, \quad \bar{q} = \frac{2\bar{T}}{\bar{M}} X_0$$

and one obtains

$$\frac{d^2 a_k}{dz^2} + [\bar{a} - 2\bar{q} \cos(2z)] a_k = 0 \quad (43)$$

A linear approximation<sup>7</sup> can be used to predict the stability boundaries of the principal parametric resonance of Equation (43) for small values of  $\bar{q}$ . In terms of input acceleration for the present problem this approximation is

$$g_x = -\frac{(1-\bar{a})}{\bar{q}} \frac{\omega^2 a}{g} \quad \text{for} \quad \frac{\omega}{2\omega_{km}} < 1 \quad (44)$$

$$g_x = \frac{(1-\bar{a})}{\bar{q}} \frac{\omega^2 a}{g} \quad \text{for} \quad \frac{\omega}{2\omega_{km}} > 1$$

## THEORETICAL AND EXPERIMENTAL RESULTS FOR SMALL MODEL

Previous work with cylinders containing liquid has shown that many natural modes, both symmetric and nonsymmetric, exist for practical ranges of system geometry, and much complicated nonlinear behavior results from the interaction of their responses under longitudinal excitation. In the present work, we have focused our attention primarily on the principal parametric resonance. Nevertheless, such a resonance exists for each natural mode of the system. Since the qualitative behavior is similar for each mode, for simplicity, we investigate the interaction of the various symmetric modes ( $m = 0$ ) with the  $k = 1, m = 10$  nonsymmetric mode for various conditions of excitation. Sufficient theoretical and experimental data were obtained to provide a reasonable comparison for the behavior of Tank A. All experimental data are presented in numerical form in Appendix B.

### Natural Frequencies of Tank with Top Mass

The variation of natural frequency with liquid depth for several modes of Tank A is shown in Figure 6, where each of the three parts is for a different top mass. Theoretical computations were performed for the largest mass (Fig. 6a) only. All symmetric modes in the given frequency range were obtained, although only one nonsymmetric mode is indicated. Of course, many other nonsymmetric natural modes existed in this range (note that experimental data for two nonsymmetric modes are given in Figures 6b, c).

Natural frequencies for the symmetric modes were determined experimentally by detecting peaks in the pressure at the center of the tank bottom and/or detecting peaks in the output acceleration of the top mass.

Although Figure 6 indicates a condition of zero ullage pressure, up to  $p_0 = 10$  psig had to be used in order to obtain data for the symmetric modes. This was necessary to prevent the occurrence of instability in some non-symmetric mode, in which a simple linear symmetric response no longer was present. Fortunately, this procedure was possible since the frequencies of symmetric modes were determined to be independent of ullage pressure. We emphasize, however, that frequencies of nonsymmetric modes are highly dependent on ullage pressure, so that data for the  $k = 1, m = 10$  mode (as well as the  $k = 1, m = 13$  mode) in Figure 6 were taken at  $p_0 = 0$ . Data for these modes were taken as peaks in the wall response at the antinode of the axial wave form. Of course, the position of this antinode shifted with different liquid depths.

Theoretical data for Figure 6a were obtained by the use of a five-term ( $n = 1$  to  $5$ ) expansion in Equation (12) and computing the value of the determinant for the resulting  $15 \times 15$  matrix. For computing the determinant, frequencies were selected in the vicinity of the experimentally measured values for a given mode, and the determinant value was plotted as a function of frequency. The zeros of this function were taken as the natural frequencies.

Some deviation between theory and experiment can be seen to exist in Figure 6a. However, the use of more terms in the expansions would reduce this deviation. This can be seen from the single point computed for  $n = 10$  terms for the third symmetric mode at a depth of  $h/l = 0.55$ . Since the five-term expansions appeared to give a sufficiently good comparison between theoretical and experimental results, most of the computations were thereby limited in order to reduce the required digital computer time.

Several interesting observations can be made from the data in Figure 6. Although the frequency of the  $m = 10$  mode is considerably below those of the symmetric modes throughout most of the depth range, pressurizing the tank can raise the nonsymmetric mode above the lowest symmetric mode. Furthermore, to excite the  $m = 10$  mode as a principal parametric response requires an excitation frequency of  $2\omega_{1-10}$  at a given liquid depth, which means an excitation near the first symmetric mode. Thus, strong interaction between the two modes can be expected in determining the dynamic stability of the principal parametric resonance for the  $m = 10$  mode.

For low liquid depths, it can be seen that the first symmetric mode represents the first coupled axial top mass-shell mode with only small liquid effects, while the second symmetric mode represents the first coupled liquid-shell mode with only small top-mass effects. However, these roles of the first two modes are interchanged for greater liquid depths as indicated by the dashed lines in Figure 6a which represent the respective decoupled modes.

From Figure 6, it can be seen that variation in top mass had no effect on the nonsymmetric mode but a strong effect on the first two symmetric

modes for a middepth range of liquid. This is shown further in Figure 7. Finally, the influence of ullage pressure on frequencies of the nonsymmetric linear mode was not measured since this has been determined by various previous investigations.

#### Forced Axisymmetric Response

The linear forced axisymmetric response comprises the initial state for determining dynamic stability of the system. Therefore, theoretical and experimental results are compared for this part of the tank behavior in order to get some idea of the strong influence it has on the instability mechanism.

Figure 8 shows a comparison of theoretical and experimental axisymmetric forced response for a frequency range which includes the first two modes with a liquid depth of  $h/l = 0.69$ . Although the data were taken at  $p_0 = 10$  psig, the results are independent of pressure, as has already been mentioned. Here, the acceleration amplification of the top mass was chosen as a comparison parameter, although the liquid pressure at some point in the tank could have been used just as well. An intermediate liquid depth was chosen as a worst possible condition for using a given number of series terms in the theoretical computations. That is, previous work indicates that the most serious distortions of tank axial mode shape from a half-sine wave occurs at intermediate depth ranges.

Theoretical points were determined from a numerical inversion of Equation (28) by means of a digital computer. Of course, the net sum of the forced axial displacement components  $\hat{u}$  at  $x = l$  form the part of the theoretical solution which is used in Figure 8. Basically, five terms were used, although ten terms were used for part of the range as indicated. It can be seen that more terms reduce the discrepancy between theory and experiment. Also, the location of the theoretical and experimental resonance points corresponds with the location of the respective natural frequencies for the first two symmetric modes in Figure 6a. Thus, the agreement between theory and experiment can be made as good as is desired, and the most terms in the expansions are required at intermediate depths.

It has been mentioned that a plot of axisymmetric pressure response at some point in the liquid looks qualitatively like that of the top mass acceleration response shown in Figure 8. This correspondence is extremely important in understanding the role of this initial state in determining dynamic stability of additional perturbed motion. That is, although longitudinal excitation acceleration amplitude may be held constant as frequency is varied, the magnitude of the actual stress resultants which comprise the parametric forces can vary considerably in amplitude, depending on the input frequency.

It can be surmised that the dynamic force exerted by the top mass on the cylinder contributes dominantly to the axial stress resultant  $N_{xxa}$ , while the corresponding axisymmetric internal pressure contributes dominantly to the circumferential stress resultant  $N_{\theta\theta a}$ . Thus, we have

the two sources of parametric excitation which appear in the stability Equations (39) or (43). Parametric excitation occurs with either or both sources present; however, it will be seen later that the dynamic pressure exerts a stronger influence on stability for the configurations investigated.

### Stability Boundaries

Theoretical stability boundaries for the  $k = 1$ ,  $m = 10$  principal parametric mode were determined by means of a five-coordinate term approximation ( $N = 5$ ) in the single eigenvector approximation ( $k = 1$ ), Equation (43). Actual boundaries were computed by Equation (44). Experimental results were obtained for the corresponding conditions for which numerical results were computed, as well as additional conditions in order to demonstrate the influence of a number of parameters in the system.

Experimental points were determined by holding input acceleration constant and slowly varying frequency in the vicinity of twice the  $k = 1$ ,  $m = 10$  natural mode until the subharmonic wall motion appeared. We emphasize that the frequency of this natural mode depended on both liquid depth and ullage pressure so that the frequency range of its principal parametric resonance varied correspondingly. However, as has been mentioned previously, the frequencies of axisymmetric modes are independent of ullage pressure, and their variation with liquid depth is not the same as that for the nonsymmetric mode, so that a variety of behavior can be experienced with different combinations of the system parameters.

The influence of liquid depth on the stability of the  $k = 1$ ,  $m = 10$  principal parametric mode is shown in Figure 9, where input acceleration amplitude is plotted against the ratio of input frequency to twice the natural frequency  $\omega_{1-10}$  for this mode at the indicated fixed values for the other parameters of the system. For this frequency parameter, the experimental points were normalized to the frequency at the minimum point of the experimental boundary (which occurs essentially at twice the experimental natural frequency), while the theoretical points were normalized to twice the theoretical natural frequency. This procedure allowed a better direct comparison of the boundaries since the theoretical and experimental natural frequency  $\omega_{1-10}$  did not always coincide for the five-term computations (see Fig. 6a).

Theoretical stability boundaries for a principal parametric resonance characteristically converge on zero for the unity value of the frequency parameter used here<sup>7</sup> when damping is not included in the theory. However, the experimental boundaries should fall above and within the theoretical boundary since damping is always present in the experimental system. A higher experimental boundary corresponds to the presence of increased damping.

Note that the three boundaries shown in Figures 9a - c are plotted to a different scale, each being about one order of magnitude apart. This is emphasized in Figure 9d where only the experimental points are plotted on a logarithmic vertical scale. An immediate conclusion can be made that the liquid is very effective in producing the instability in the system for this mode. That is, instability occurs at lower input accelerations with more liquid present. This result is logical if one considers that the parametric action occurs through the interaction of an inplane stress resultant with the curvature of the shell at a given point. Thus, in the stability equations, a term of the type  $N\theta\theta_a (\partial^2 w / \partial \theta^2)$  is much larger than one like  $N_{xxa} (\partial^2 w / \partial \theta^2)$  for the mode being considered, so that mathematical and physical correspondence follows.

Good correspondence between theory and experiment is shown in Figures 9a - b while that in Figure 9c is not so good. This discrepancy for the completely filled cylinder resulted primarily because of experimental error at such low values of input acceleration. Although a narrow band dynamic analyzer filter was used for measuring the input at nearly a single frequency, the input was within the mechanical noise level of the cooling fans of the electrodynamic shaker so that the actual input was more wide band than desired. Hence, the experimental boundary falls outside that for the theory because of the extraneous input energy. This problem was not so significant for the data of Figures 9a - b since the input was above 0.01 g, which is about the noise level in the shaker system. The overall agreement between theory and experiment is quite good.

The effects of ullage pressure on dynamic stability are shown in Figure 10. These data can be used with those of Figure 9a to show a fairly wide range of pressure effects. The three boundaries are shown for comparison on a logarithmic scale in Figure 10c. In Figures 10a-b, the experimental value of  $\omega_{1-10}$  was used for normalizing the theoretical points since the theoretical natural frequency was not computed for this case.

Deviation between theory and experiment occurs for two different reasons in Figures 10a-b. The left side of the experimental boundary in Figure 10a rises much more rapidly than that for the theory. This occurred because of the presence of coupling with the next lower nonsymmetric mode in the system. This type of coupling is quite prevalent in a practical system since many modes are present, and the modal density is quite high. Such coupling can be predicted theoretically only if stability is studied by the coupled set of Mathieu Equations (39) rather than the single eigenvector term approximation, Equation (43).

Deviation between theory and experiment occurred for another reason for the data in Figure 10b. Here, the excitation frequency virtually coincides with the theoretical frequency for the third symmetric mode (see Fig. 6a). Thus, the influence of this mode was strongly felt in the shape of the stability

boundary. However, the experimental third mode occurs at a somewhat higher frequency, so that its effects are not so pronounced on the experimental curve. The use of more terms (i. e.,  $N > 5$ ) in Equation (43) probably would produce a better correspondence for this case.

The above explanation based on the interaction of linear symmetric and parametric nonsymmetric modes can also be applied to the relative position of the three boundaries in Figure 10c. Note it does not simply follow that in all cases an increase in ullage pressure will tend to increase stability (i. e., raise the stability boundary). The boundary for 3 psig is somewhat higher than that for 6 psig. This probably occurs because the integrated dynamic pressure loading of the initial state can be larger at the frequency  $2\omega_{1-10}$  for 3-psig ullage than it is at 6-psig ullage. That is, the total dynamic pressure loading is determined by the dynamic pressure distribution at the driving frequency, as well as the proximity of the driving frequency to a natural frequency of a symmetric mode.

The above arguments can also be applied to explain the location of the stability boundaries in Figure 11, in which the influence of top mass on stability has been determined. Zero liquid depth was used to eliminate the influence of the liquid. In general, one might expect that the smallest mass would produce the least parametric force. However, the force is a function of both the mass and its acceleration for a given parametric mode so that the tank with the lighter mass is more unstable for the given conditions. A glance at Figures 6a - c shows that excitation at  $2\omega_{1-10}$  is much nearer the first symmetric mode frequency for the smallest mass than for the other two in the case of the empty tank. Further, the boundary for the intermediate mass with intermediate location of the first symmetric mode frequency in Figure 6 is correspondingly intermediate in its position in Figure 11. The behavior of the system with the largest mass then falls at the opposite extreme.

It appears that the single eigenvector term approximation, Equation (43), is quite useful for determining a reasonably good approximation for dynamic stability in the system investigated. However, even for the limited data obtained in this study, it is apparent that the more exact representation, Equation (39), is required for an overall investigation. This will be emphasized further by subsequent data to be presented.

### Nonlinear Response

Although no nonlinear analysis capable of predicting subharmonic response in the principal parametric mode was formulated in this study, some experimental observations of this type of response were carried out in order to present a better overall picture of parametric behavior in a liquid-shell system coupled with a top mass. These results showing the influence of several parameters on the principal parametric response in the  $k = 1$ ,  $m = 10$  mode are shown for Tank A in Figures 12 through 14, where

wall response is plotted as a function of frequency ratio. These curves display the usual character of a principal parametric response<sup>3, 7</sup> in that they are either nonlinear softening (bend to the left) or nonlinear hardening (bend to the right) and include jump phenomena where the response suddenly appears and jumps up to a finite value or suddenly disappears as a result of damping.

Figure 12 shows the influence of liquid depth on the subharmonic response. These curves correspond to the stability boundaries given in Figure 9. An increasing bend in the response indicates the presence of greater nonlinearity as long as input acceleration is held constant or is a lower value for the curves with greater bend. Thus, it may be concluded that the largest nonlinearity was present at the largest liquid depth. That is, the largest nonlinear interaction (which is distinct from the parametric interaction discussed in the previous section) between the liquid and shell occurs at the largest liquid depth.

Similar response curves showing the influence of ullage pressure are shown in Figure 13. These data correspond to the stability boundaries given in Figure 10. Here, it is most interesting to note that at zero pressure the response is softening, at 3 psig, it becomes hardening, and, at 6 psig, it again becomes softening. It may be noted from Figure 9a that the frequency of  $2\omega_1 - 10$  has changed its position relative to the first two symmetric modes and probably is the reason for the changing behavior.

Response curves for different top masses on an empty tank are shown in Figure 14. These responses correspond to the stability boundaries in Figure 11. Here, no particularly dramatic change in the curves takes place for different masses. Apparently, the top mass does not have so pronounced an effect on the response as the liquid for the mode investigated. This behavior is similar to the effect of these parameters on the parametric action itself, which has been discussed earlier.

It must be emphasized that response in a principal parametric mode is probably the simplest kind of nonlinear response (and the only one that has been explained analytically to date) that can be observed in the system under consideration. Many other types of nonlinear response, such as beating, amplitude modulation, superharmonics, etc., can be observed experimentally. In the present investigation, we have seen that liquid surface motion did not enter the basic problem. However, Figure 15 shows a nonlinear response in the present system in which nonlinear liquid surface coupling does occur. The lower trace is also the tank wall response but is expanded on a greater time scale. The tank was being excited under the indicated conditions so that it was responding basically in the  $k = 1, m = 10$  principal parametric mode. However, in addition the high frequency tank motion, it sustained a steady-state, low frequency amplitude modulation, and, simultaneously, the liquid surface was excited at a large amplitude in its first symmetric mode. Such nonlinear coupling between the liquid surface and high frequency tank



wall motion has been explained previously by Chu and Kana<sup>12</sup> in a partially filled tank which is subject to lateral excitation and which sustains basically harmonic wall response. The present case is even more complicated since the wall sustains basically 1/2-subharmonic wall response.

Only nonlinear wall responses were shown in Figures 12 through 15. It must be emphasized that similarly complicated responses occur in pressure as well. Some details of pressure changes, as well as other types of complicated wall responses, are given in the next section for various configurations of the larger model tank.

## EXPERIMENTAL RESULTS FOR LARGE MODEL WITH STIFFENERS

Many types of nonlinear response besides subharmonic motion could be observed while testing Tank A. However, it was decided to perform detailed observations of such responses in the larger, more representative model in order to get a better physical feel for their significance in space vehicle systems. In addition, the effects of ring stiffeners are determined by including different numbers of rings so that some judgment can be made about the possibility of such responses occurring in Saturn-type launch vehicles. Examples of stability boundaries are given for those cases which appeared to be the most unstable in each respective tank, that is, where the tank became unstable with the least input acceleration amplitude. Only typical results are presented in this section. For the most part, it will be seen that the results provoke more questions than answers, which emphasizes that only the surface has been scratched in the study of the general area of nonlinear response of a liquid-tank system.

Results from Tank S-0 are shown in Figures 16 and 17. Considerable detail on subharmonic motion in this tank has already been presented in our earlier work<sup>2</sup>. Here, we have included only enough additional results to compare with that which follows for tanks with rings installed.

Stability boundaries for several principal parametric modes in Tank S-0 are shown in Figure 16, while an example of principal parametric response is shown in Figure 17, for the  $k = 1$ ,  $m = 8$  mode. The wall response was measured at an antinode of the motion. A great density of unstable regions can readily be seen from the occurrence of three unstable regions between 68 and 75 cps. A similar density occurs throughout the frequency domain for this tank. Thus, at any appreciable value of input acceleration, the most usual type of response by far occurs as some nonlinear form.

From Figure 17, it can be seen that the subharmonic wall response is hardening for the example given. At the same time, however, the bottom pressure first decreases and then increases as the frequency is increased.

Phases between the various parameters can readily be determined. The amplitude of the center trace is proportional to input acceleration which was held constant by the shaker control system. However, this trace is in-phase with input displacement; therefore, it is out-of-phase with input acceleration. Jump phenomena are not indicated in these photographs, although, of course, they do accompany such responses. Thus, sudden changes in wall displacement and pressure amplitudes can readily occur. Many other kinds of nonlinear responses also can occur in Tank S-0. However, we will present examples of their occurrence in the ring-tanks in order to emphasize that they still occur for these tank configurations, although not to such a great extent, depending on the number of rings present.

Figures 18 through 21 show results obtained in Tank S-1. Three stability boundaries are shown in Figure 18. Note, however, that two different ones are given for the  $k = 2$ ,  $m = 11$  mode. A split natural frequency for this mode causes the double boundary. Actually, one mode is proportional to  $\cos m\theta$  and the other to  $\sin m\theta$ . The shift in spatial distribution in displacement between the two responses could be observed experimentally. Normally, both responses should occur at the exact same frequency. In this case, eccentricities in the tank geometry cause the split.

Wall displacements corresponding to two of the boundaries in Figure 18 are shown for two subharmonic responses in Figure 19, while photographs for the  $k = 1$ ,  $m = 12$  principal parametric motion are shown in Figure 20. Both wall responses are nonlinear softening. Complete data for increasing wall amplitudes could not be obtained for either mode because of two different reasons, as is indicated in Figure 19.

Prohibitively large responses began to occur at larger amplitudes for the  $k = 1$ ,  $m = 12$  mode. That is, the audible response from the tank indicated, at best judgment, that large tank stresses were eminent, and the observations were discontinued. On the other hand, at large responses, the  $k = 2$ ,  $m = 1$  mode began to change into an even more interesting behavior, as indicated by the region marked POGO.

Figure 21 gives an example of POGO behavior which occurred within the region indicated in Figure 20, and which could occur quite readily for many different input conditions in the present system. Although the shaker was set on automatic constant acceleration control for this case, the acceleration actually produced by the control system was not held at constant amplitude because of the interaction between the pressure response and the control system. This interaction occurs in such a way that the amplitude modulated forms result. Since the output of the automatic control system represents thrust in a launch vehicle, it can be seen that a form of POGO behavior is occurring where an oscillatory deviation results between the simulated thrust (which itself is oscillatory at a higher frequency here) and its intended values. In an actual vehicle, such oscillatory deviations can become superposed on the steady thrust which is present and produce catastrophic failures.

It must be emphasized that the laboratory example of POGO behavior in Figure 21 applies only to the closed-loop interaction of the present model system with the presently used shaker control system. One can only conclude that similar behavior would occur in a launch vehicle only if its closed-loop hydraulic-structural system were dynamically similar to that of the present experiments. An exact similarity would, of course, be highly unlikely; however, it is well known that certain types of POGO instabilities can readily occur in typical systems. Thus, Figure 21 merely serves as a cautious reminder that such POGO behavior is possible in complicated liquid-structural systems and must be given due consideration.

Typical results obtained from Tank S-2 are shown in Figures 22 and 23. Several stability boundaries for principal parametric motion are shown in Figure 22, while photographs of corresponding nonlinear responses for each respective region are shown in Figure 23. Note that still another type of response corresponding to an entirely different form of instability is shown in Figure 23. For this response, both pressure and input acceleration are relatively constant in amplitude, but wall displacement sustains a form of amplitude modulation or beating within the region marked "Beating" in Figure 22. Thus, a definite region of instability for this form of response occurs similar to those for principal parametric motion. Closer observation showed that the response is basically a beat between the  $k = 3, m = 17$  and the  $k = 3, m = 18$  modes, and is excited at an input frequency which is near  $f_{3-17} + f_{3-18}$ . This type of unstable region has been predicted for systems which are governed by coupled Mathieu equations but, to the authors' knowledge, have never been observed previously in any experimental system.

In addition to the above configurations, the large model tank was tested in a three-ring configuration. However, for this tank, it is at this point that the previously described nonlinear responses are no longer prevalent for reasonable input accelerations. Thus, for the case of three or more rings, the basic response to longitudinal excitation becomes axisymmetric and linear, such as that for the initial state. In general, increasing the number of ring baffles, then, increases the stability of the system. This can be seen more directly from Figures 16, 18 and 22, where an increased acceleration input is required to produce instability as more ring baffles are present. Further, those modes in which a ring baffle coincides with a nodal circle appear to be most unstable.

#### GENERAL DISCUSSION AND RECOMMENDATIONS FOR FURTHER WORK

It is readily apparent that the problem studied in the present work is highly complicated in nature and encompasses interactions between various types of responses, each of which, when studied alone, poses quite a formidable

problem. In this light, the scope of the present program was planned and executed in a logical sequence.

A theoretical and experimental study has been conducted for a longitudinally excited, flat-bottom, pressurized cylinder which is partially filled with liquid and supports a rigid top mass. This appears to be the simplest possible system which gives a good description of parameters that are significant in launch vehicle systems. The detailed results which have been presented indicate that all parameters considered have a significant influence on initial-state axisymmetric responses, dynamic instability, and subsequent nonlinear responses. Although the model comprising Tank A is idealized in several respects, it is still sufficiently realistic so that the resulting theory, as verified by the experiments, can now be applied to systems of actual-size parameters in order to obtain at least an estimate of conditions which can produce parametric instabilities.

The second phase of the program has sought to answer questions which arise from the use of the idealized system in the first phase. In particular, it now appears that parametric instabilities are not likely to occur in tanks of Saturn-type vehicles, so long as the tanks are stiffened to an extent which is similar to that of the three-ring model tank of the present study. However, in this regard, it is realized that considerable uncertainty remains as to what type of responses will be prevalent in tanks where such a degree of stiffening is not present. In fact, the "degree" of stiffening present cannot even be defined precisely from the present results. Certainly, a better physical feeling for the required stiffness has been presented, but a more exact answer can come only from additional work. In particular, the significance of effective anisotropic properties of stiffened tanks must be explored theoretically along the lines of the work of Bagdasaryan and Gnuni<sup>5</sup>, and experimental verification should be provided. It must be recalled that some upper stage tanks in Saturn vehicles have very little, if any, wall stiffeners.

When using the developed theory for design estimates, one should bear in mind that bottom elasticity, as well as stiffening effects, have been neglected. At present, there is no simple means whereby these bottom effects on pressure distribution can be determined. The development of a membrane solution appears highly desirable. However, it appears that nothing short of finite difference methods will produce a suitable prediction of axisymmetric linear responses in a more representative tank. This, of course, has a profound bearing on the stability problem since this type of response represents the initial state of the system.

The present results indicate that parametric responses in the tank systems occur over quite narrow bandwidths of frequency, although the modal density of these narrow bands is very high. Thus, it is not clear from the present work just how readily parametric responses can occur in a system that is subject to excitation energy spread over some band rather

than at a single discrete frequency. The answer to this question must come from a study of the response of models such as those herein when subject to random inputs having various bandwidths. Thus, a more representative input can be achieved. Such a study can readily be performed and is highly recommended.

Eventually, the various types of nonlinear responses which have been observed will have to be catalogued and each considered as a possible potential problem. Needless to say, only questions remain in this regard, with very little of the present results being of much help in explaining the behavior. From an analytical point of view, nonlinear forms of the equations will be required in determining the responses, and, without doubt, coupled stability equations must be utilized, even for linear approximations. Much remains in the study of the stability of coupled Mathieu-Hill equations.

The importance of dynamic response in the present system is vividly demonstrated by the occurrence of a POGO-like behavior under controlled excitation. One is tempted to say that apparently the liquid-tank system is highly prone to display such behavior when coupled with almost any control system (such as it is in an actual vehicle). This probably results from the fact that the total pressure, whether linear or nonlinear, when integrated over the tank bottom, results in a very significant apparent mass, and the sensitivity of this apparent mass to frequency intuitively indicates the possibility of such instabilities being present. Again, very little is known about this type of interaction.

Various other comments and recommendations could be set forth in view of the results of the present study. However, for the sake of brevity, only one more will be illuminated. The present results indicate that a strong coupling occurs between wall motion, liquid pressures, bottom effects, end mass, etc., all of which are present as multiple systems in a composite vehicle. Therefore, it appears highly desirable to investigate a single system, such as that studied herein, from a mechanical impedance (preferably transmission matrix) point of view, so that the dynamics of tandem systems could be studied simply by combining the tandem elements. The development of the transmission matrix, which will be frequency dependent for a single liquid tank system, is itself no easy task. But, once it is accomplished, it can then be used for design purposes in general. It must be emphasized, however, that the mechanical impedance methods are applicable only where linear responses are anticipated, such as for sufficiently stiffened tanks.

## ILLUSTRATIONS

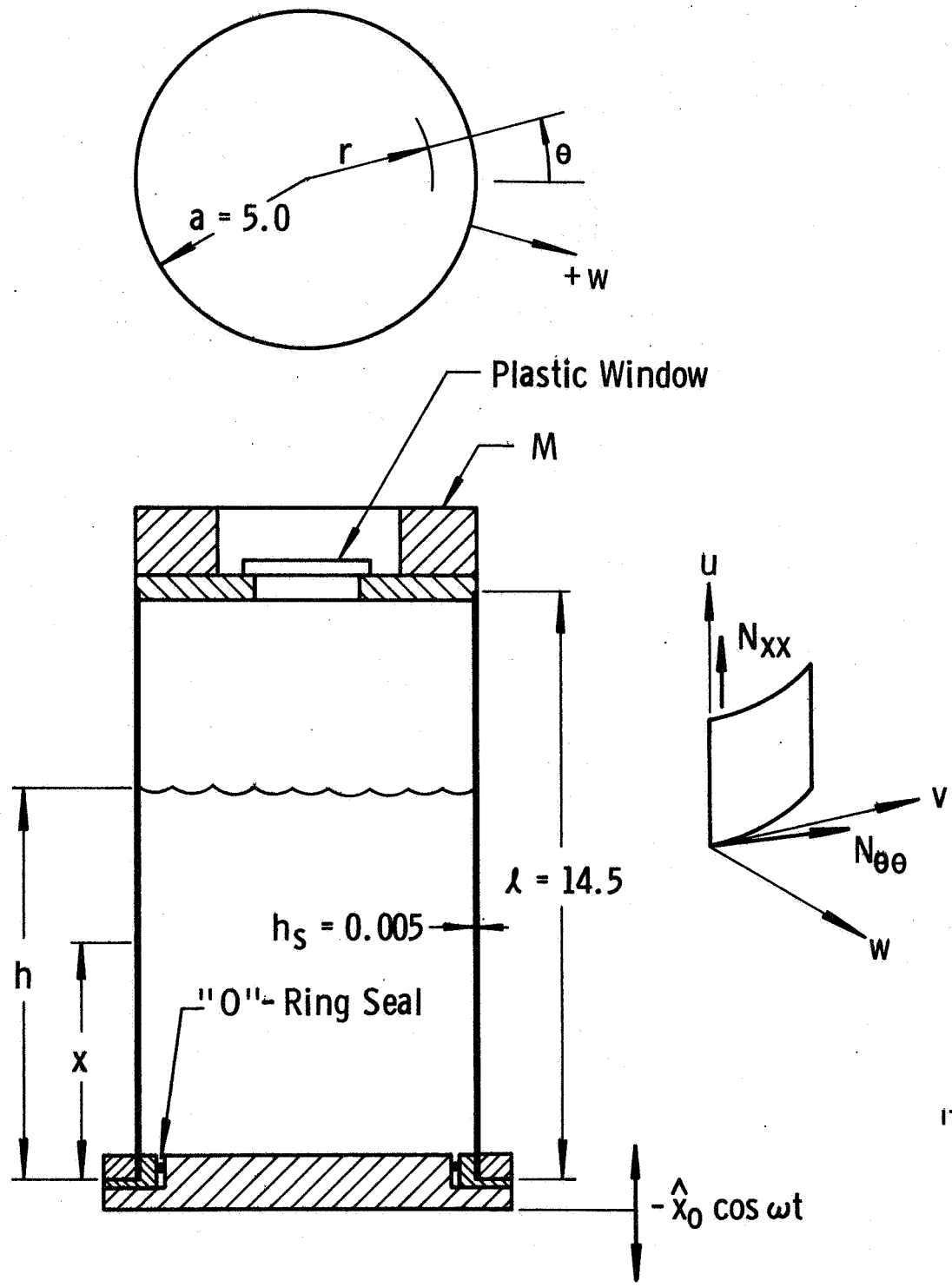


Figure 1. Coordinate System For Small Model

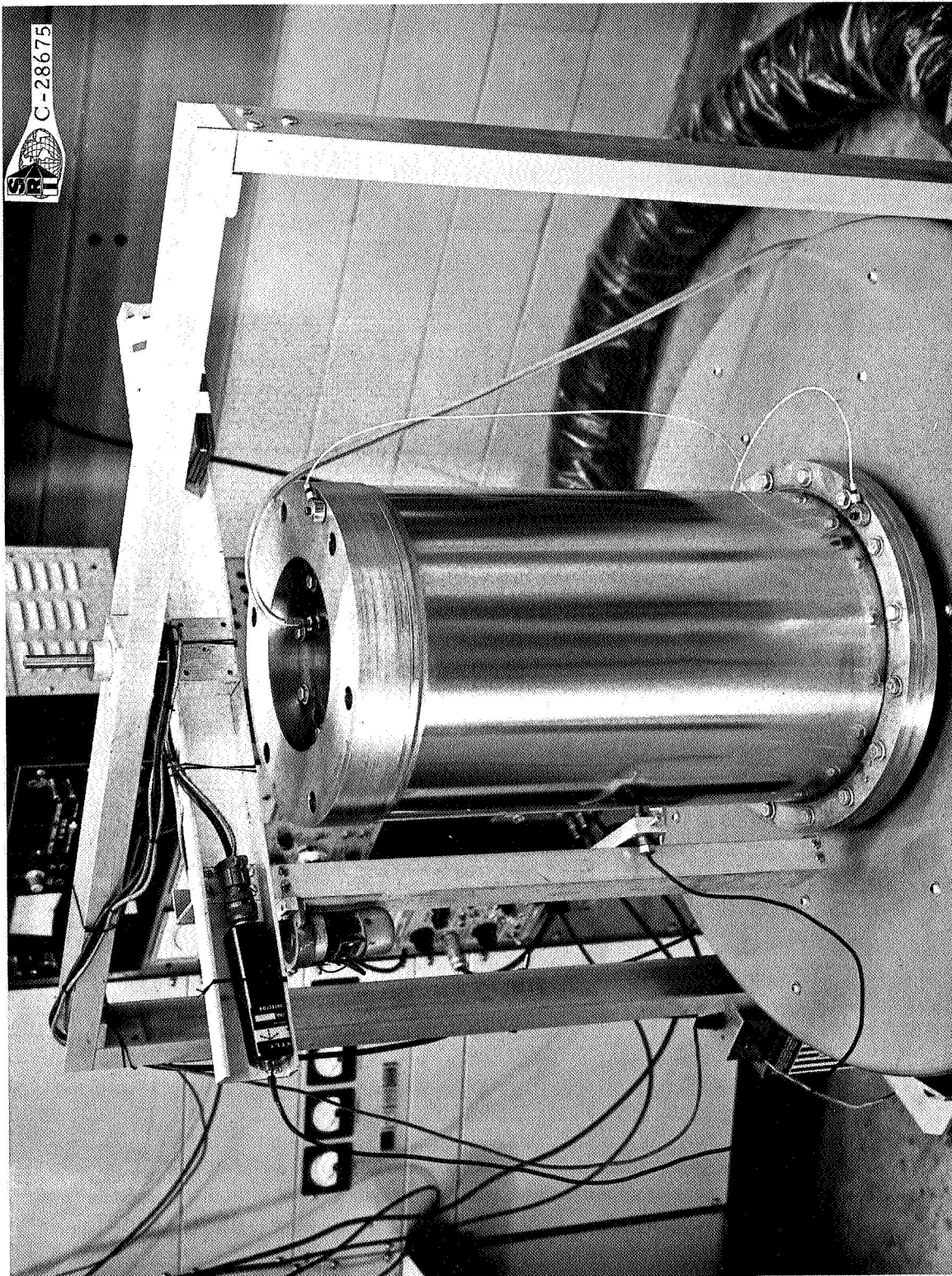


Figure 2. Dynamic Stability Apparatus For Small Model



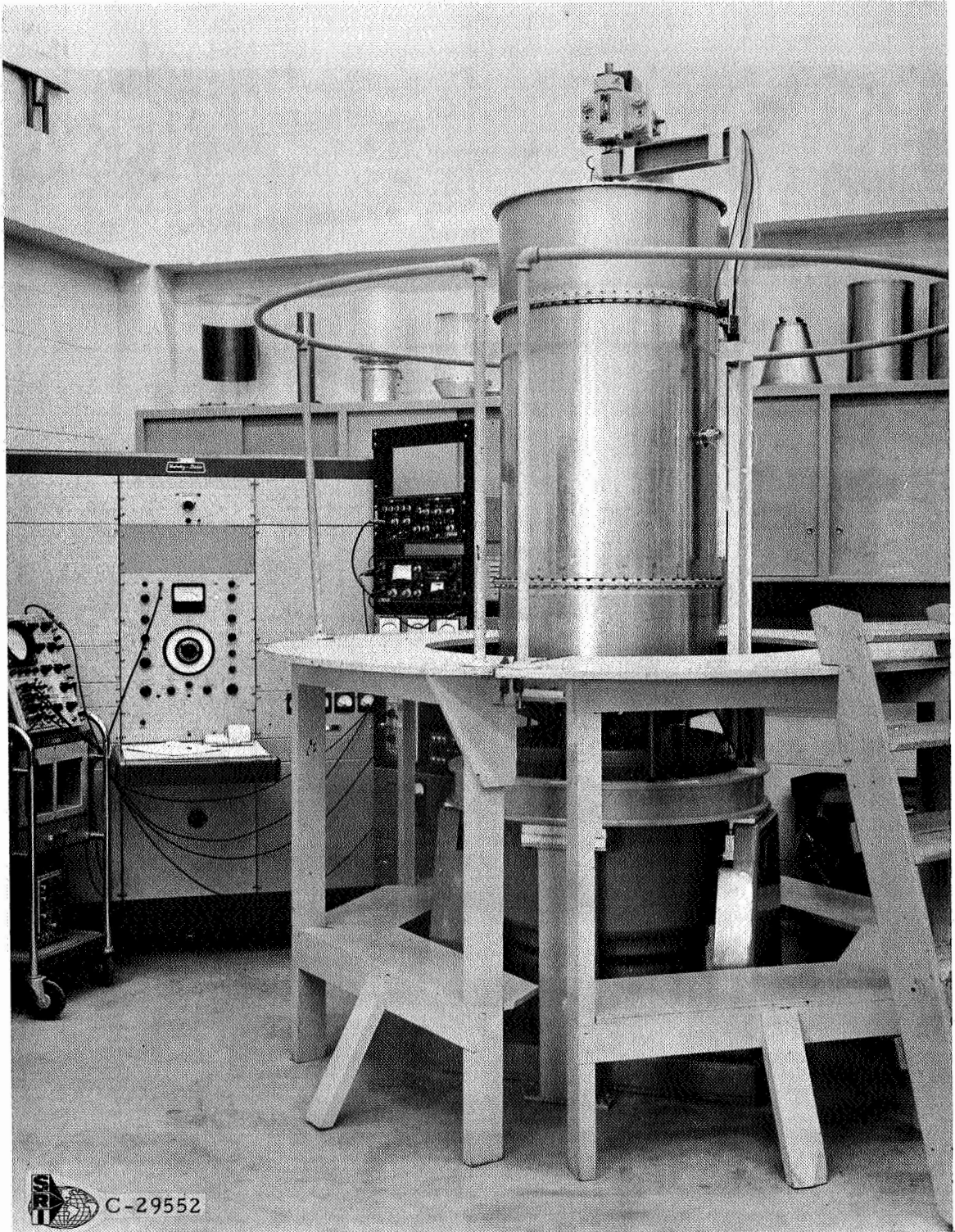
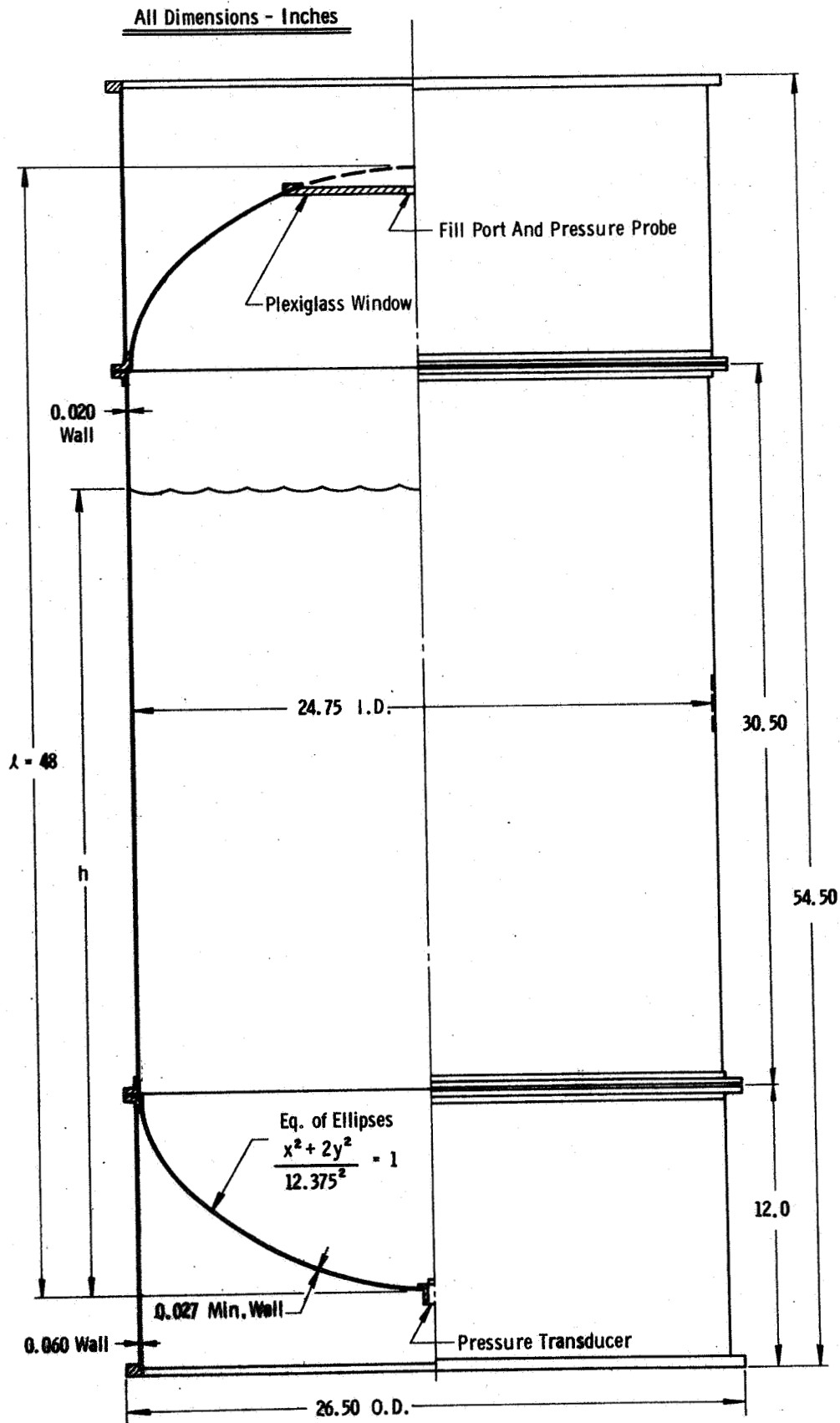


Figure 3. Dynamic Stability Apparatus For Large Model



939

Figure 4. Layout Of Large Tank

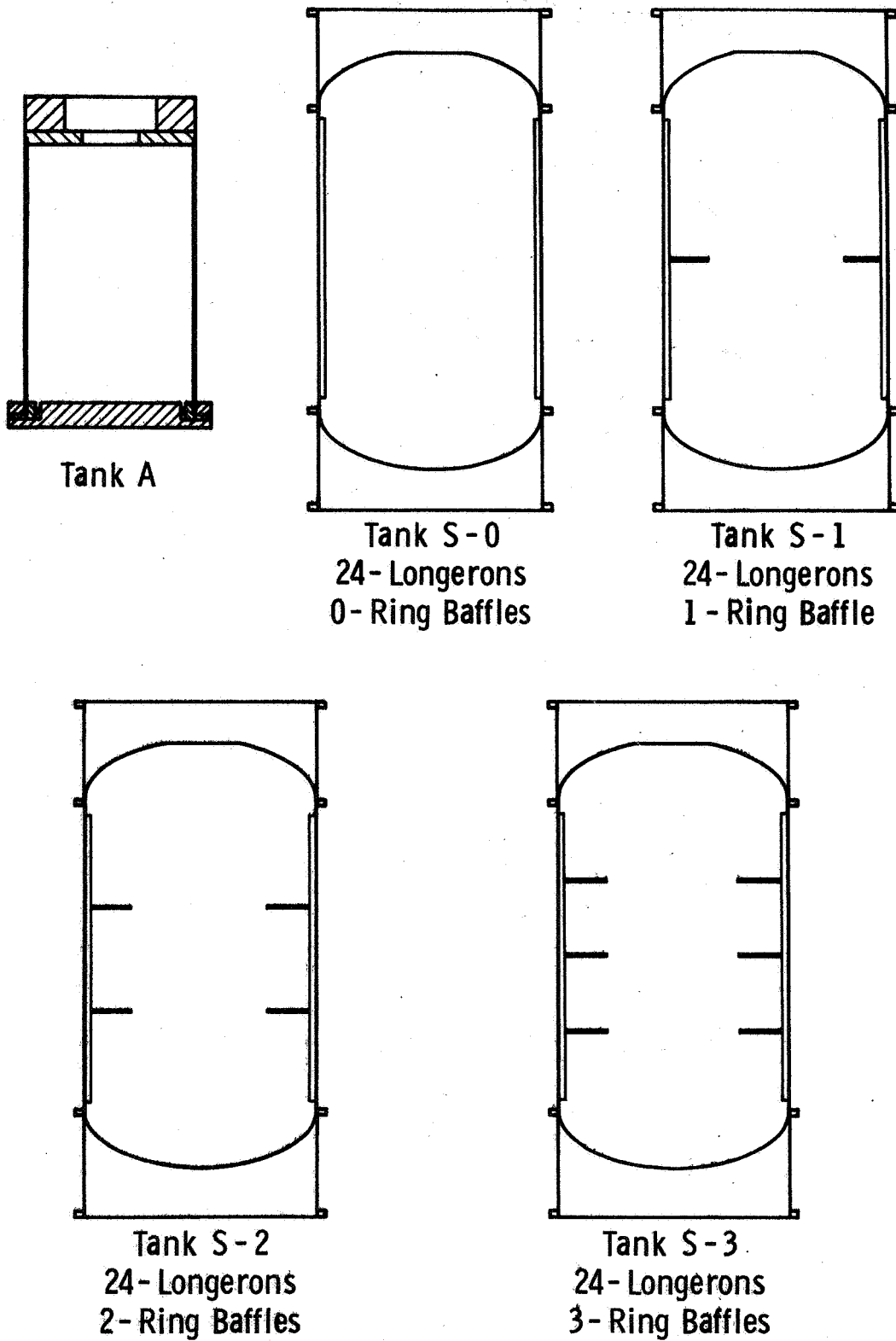
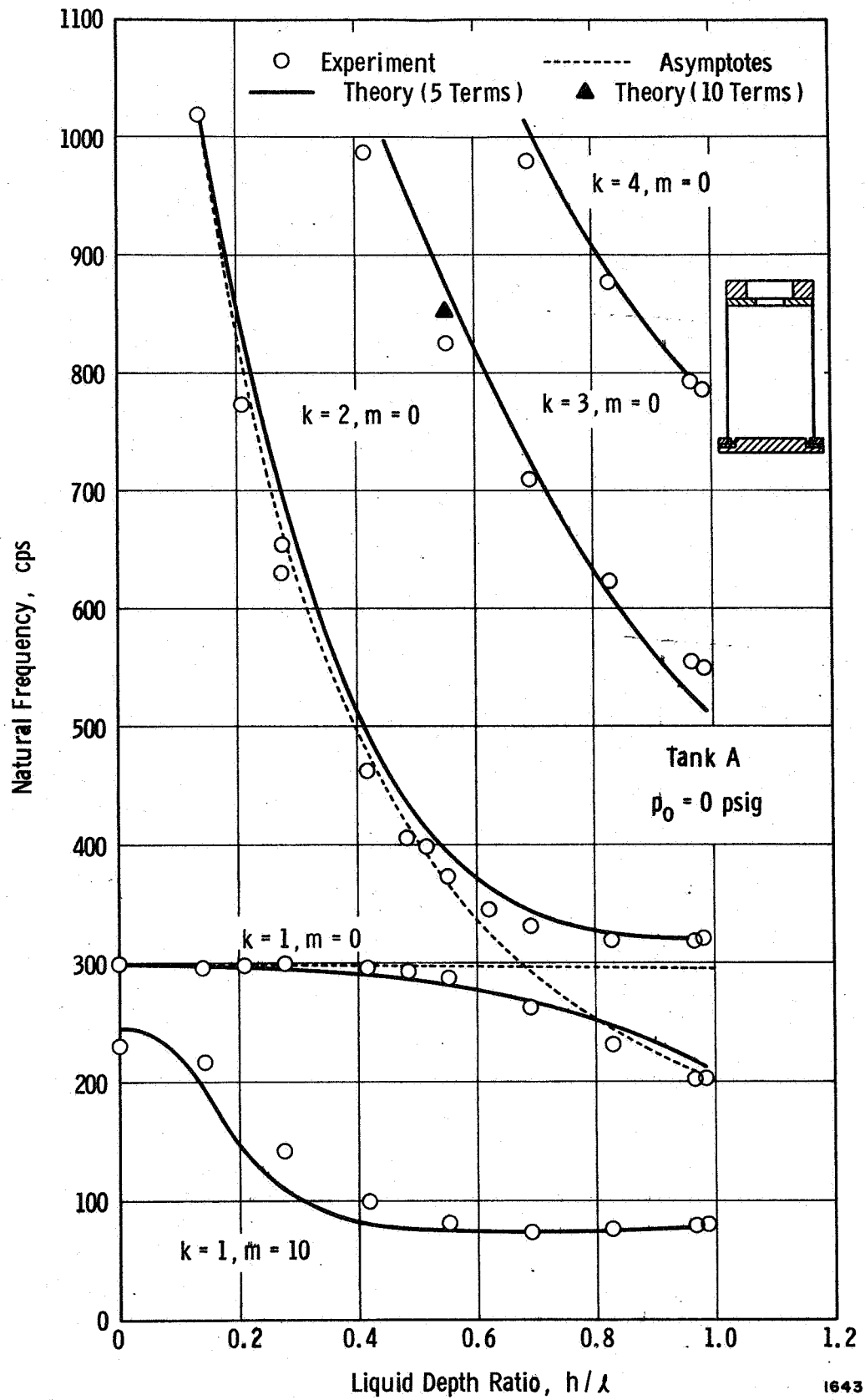


Figure 5. Configurations Of Model Tanks

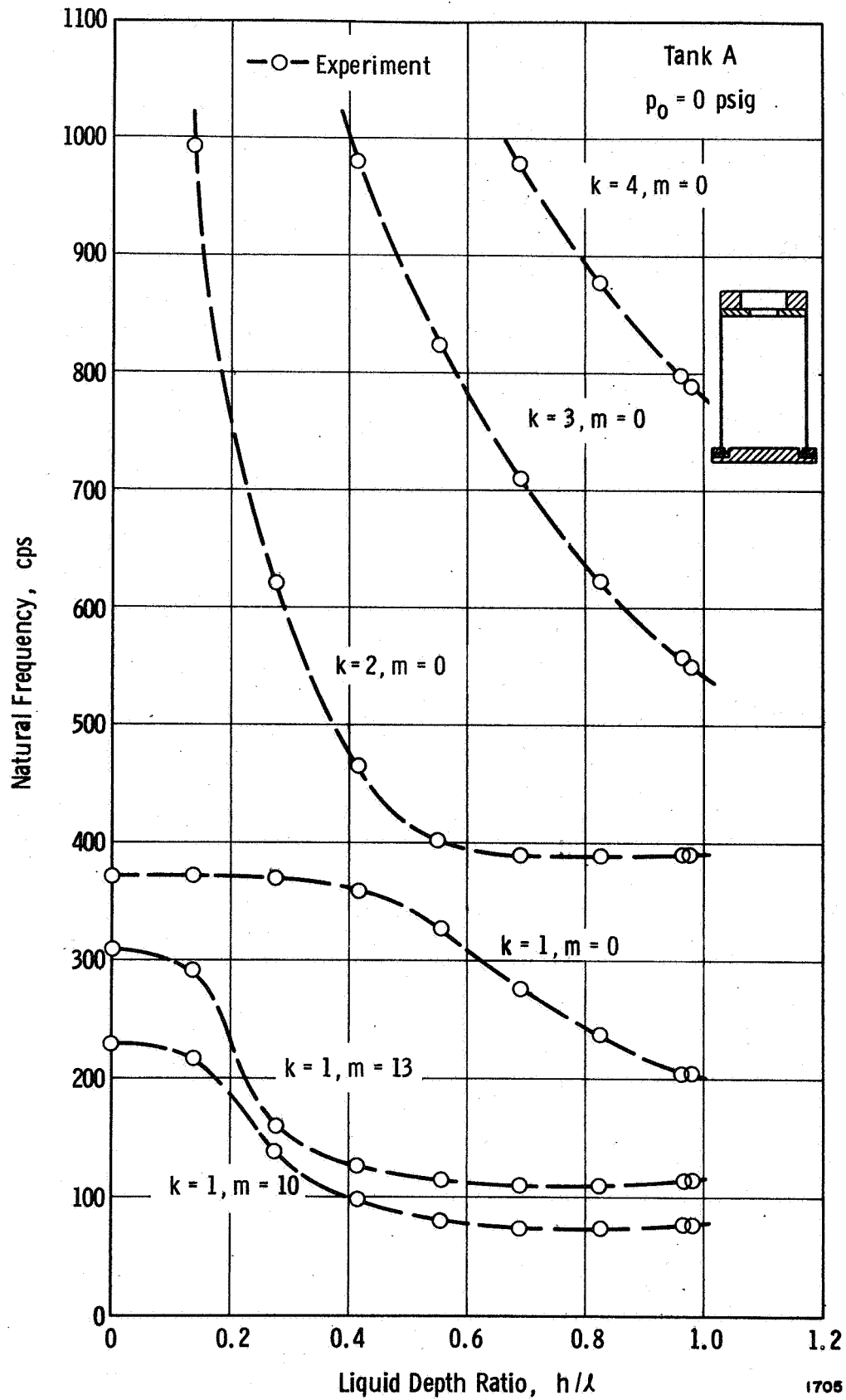
1725



1643

a.  $W_0 = 34.53$  lb.

Figure 6. Natural Frequencies Of Partially Filled Tank With Top Mass



b.  $W_0 = 22.32$  lb.

Figure 6. Natural Frequencies Of Partially Filled Tank With Top Mass

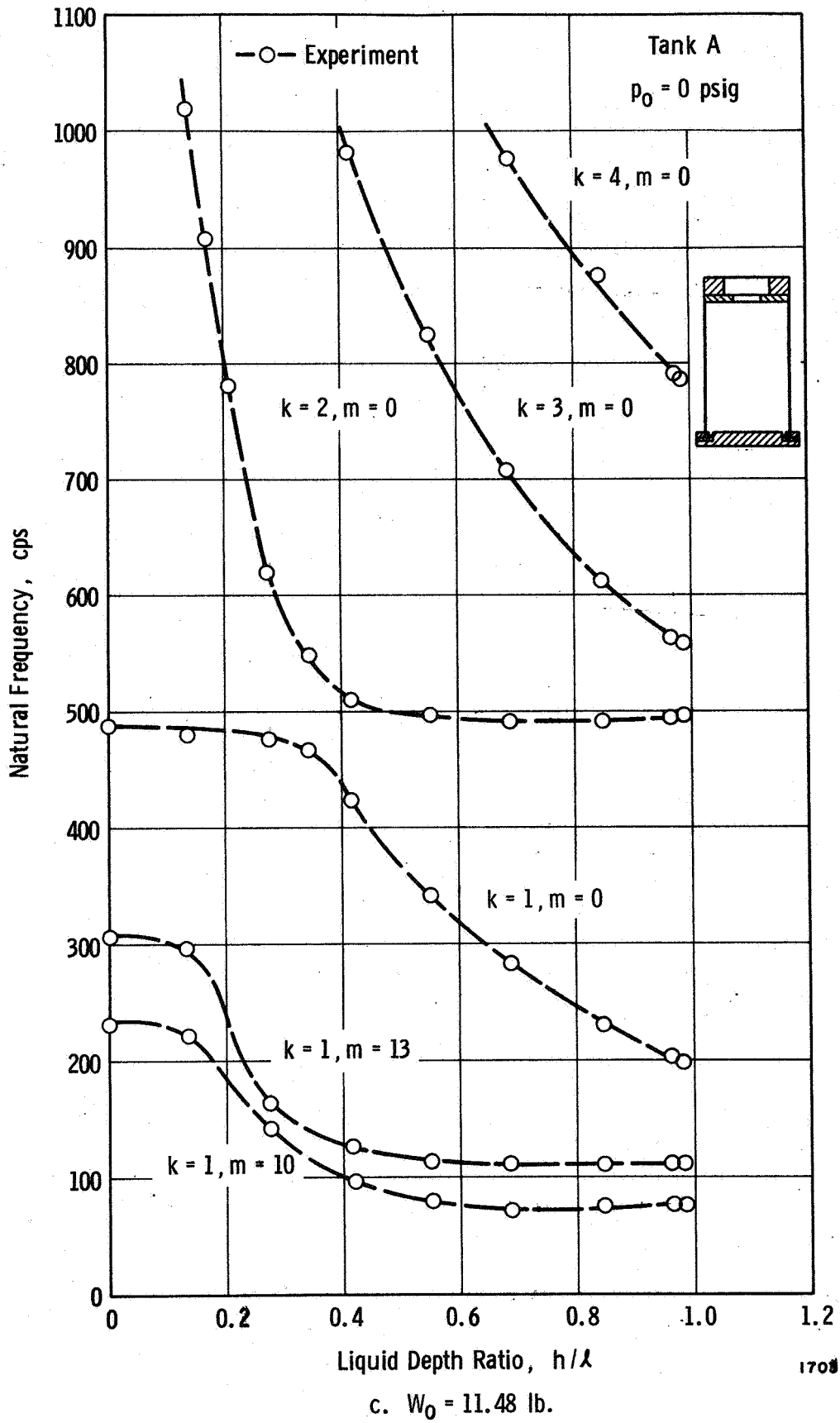


Figure 6. Natural Frequencies Of Partially Filled Tank With Top Mass

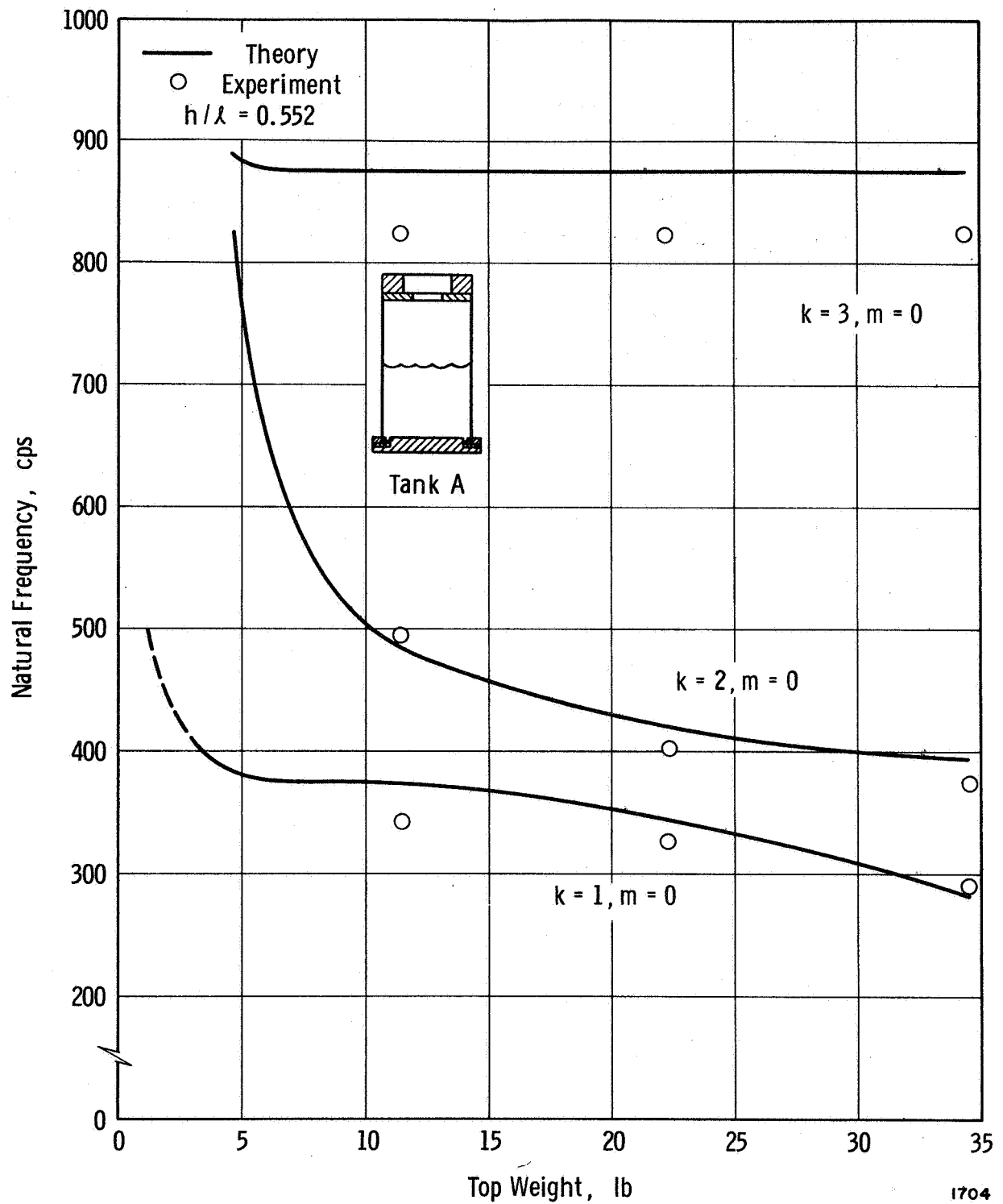
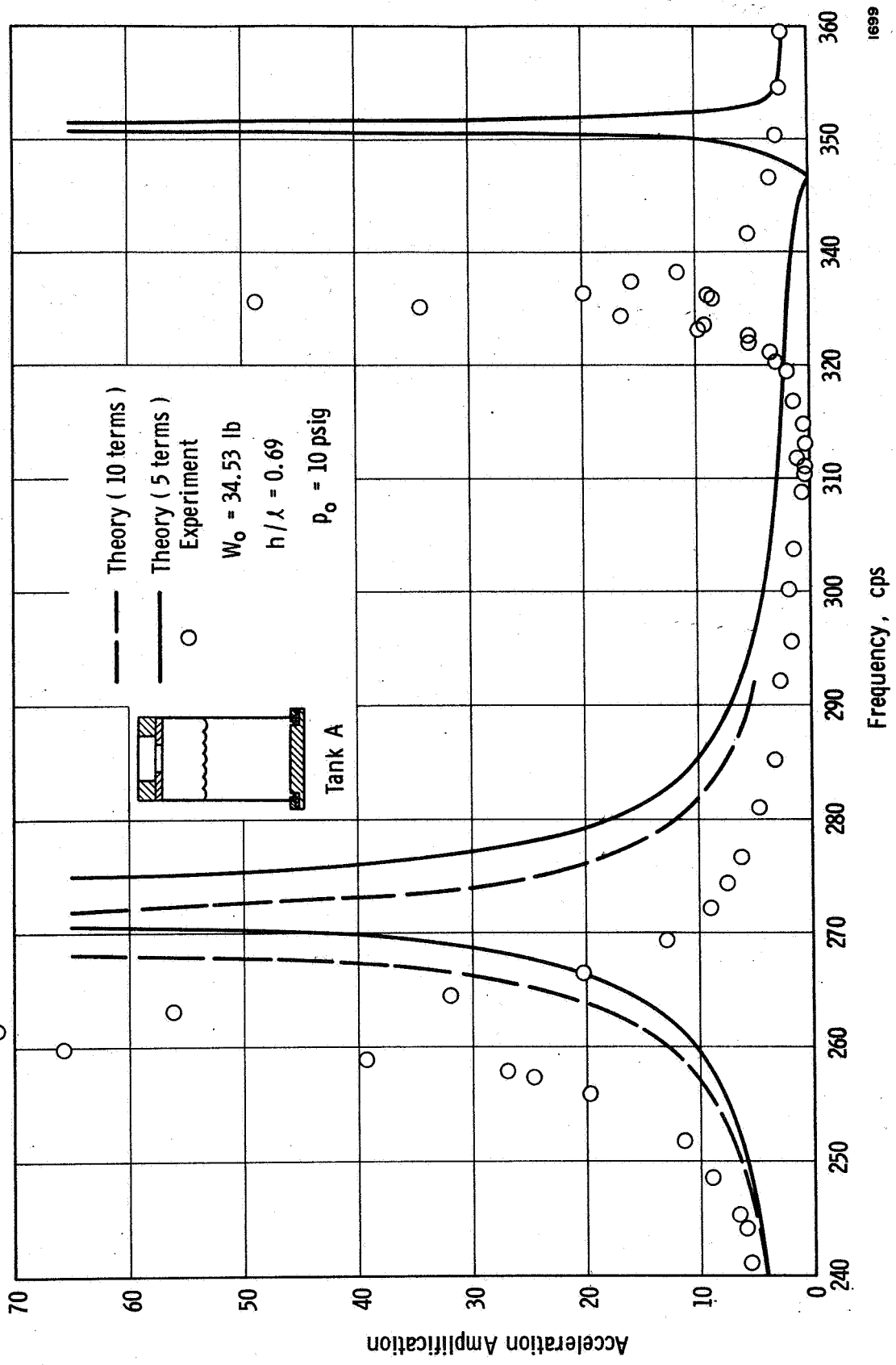


Figure 7. Effect Of Top Mass On Natural Frequencies

98.4



1699

Figure 8. Response Of Top Mass Relative To Input Acceleration For Axisymmetric Wall Response



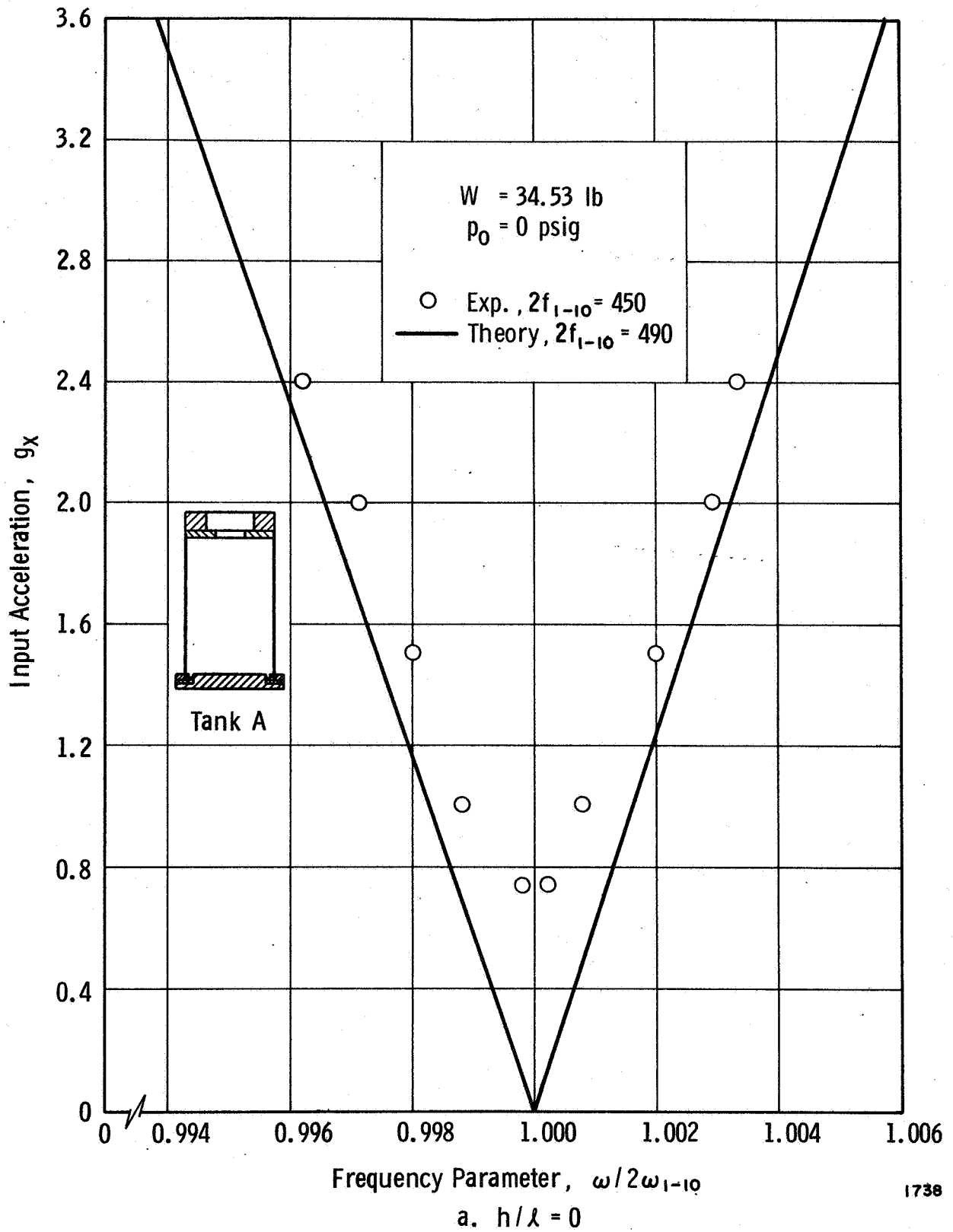
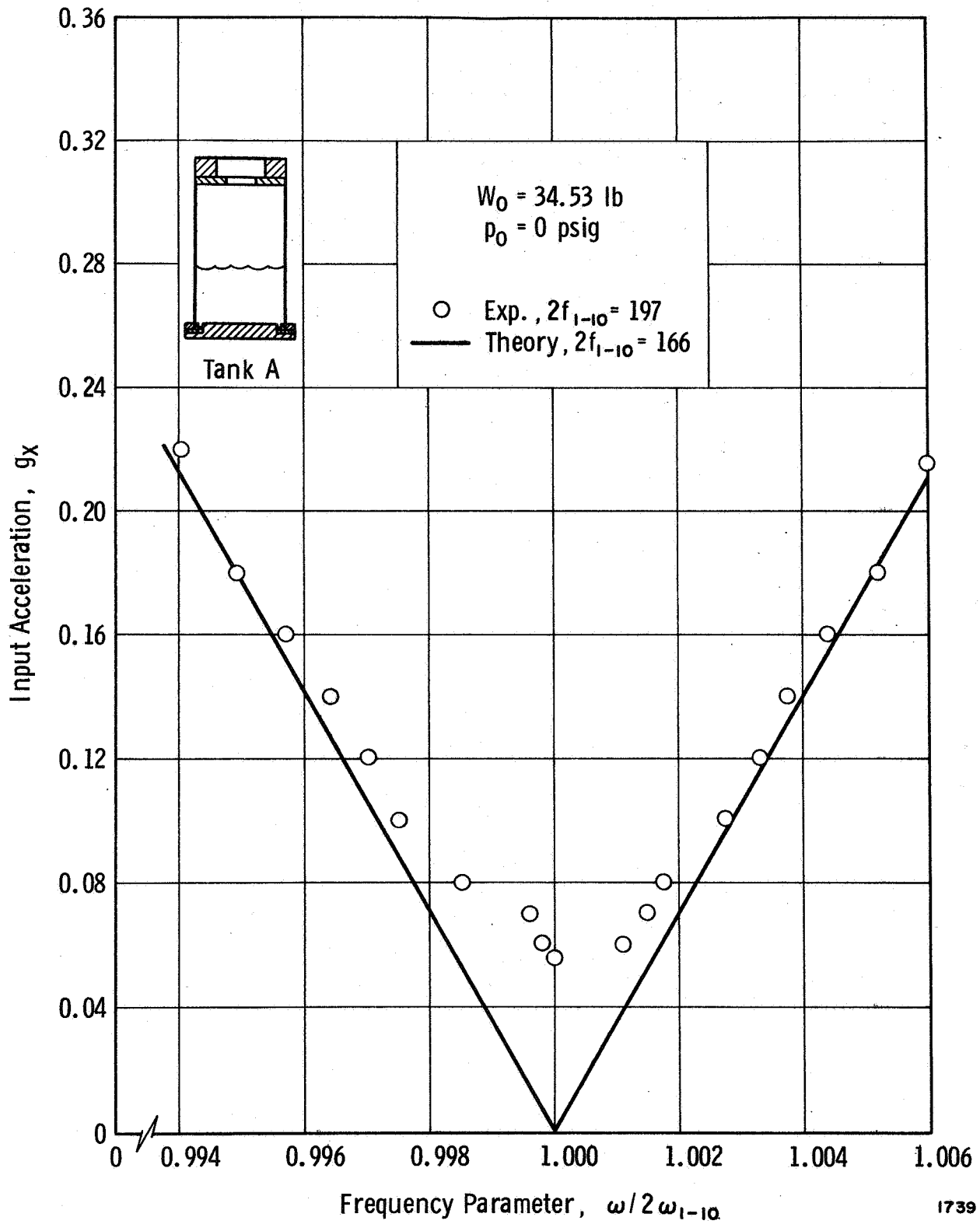


Figure 9. Influence Of Liquid Depth On Stability



b.  $h/\lambda = 0.414$

Figure 9. Influence Of Liquid Depth On Stability

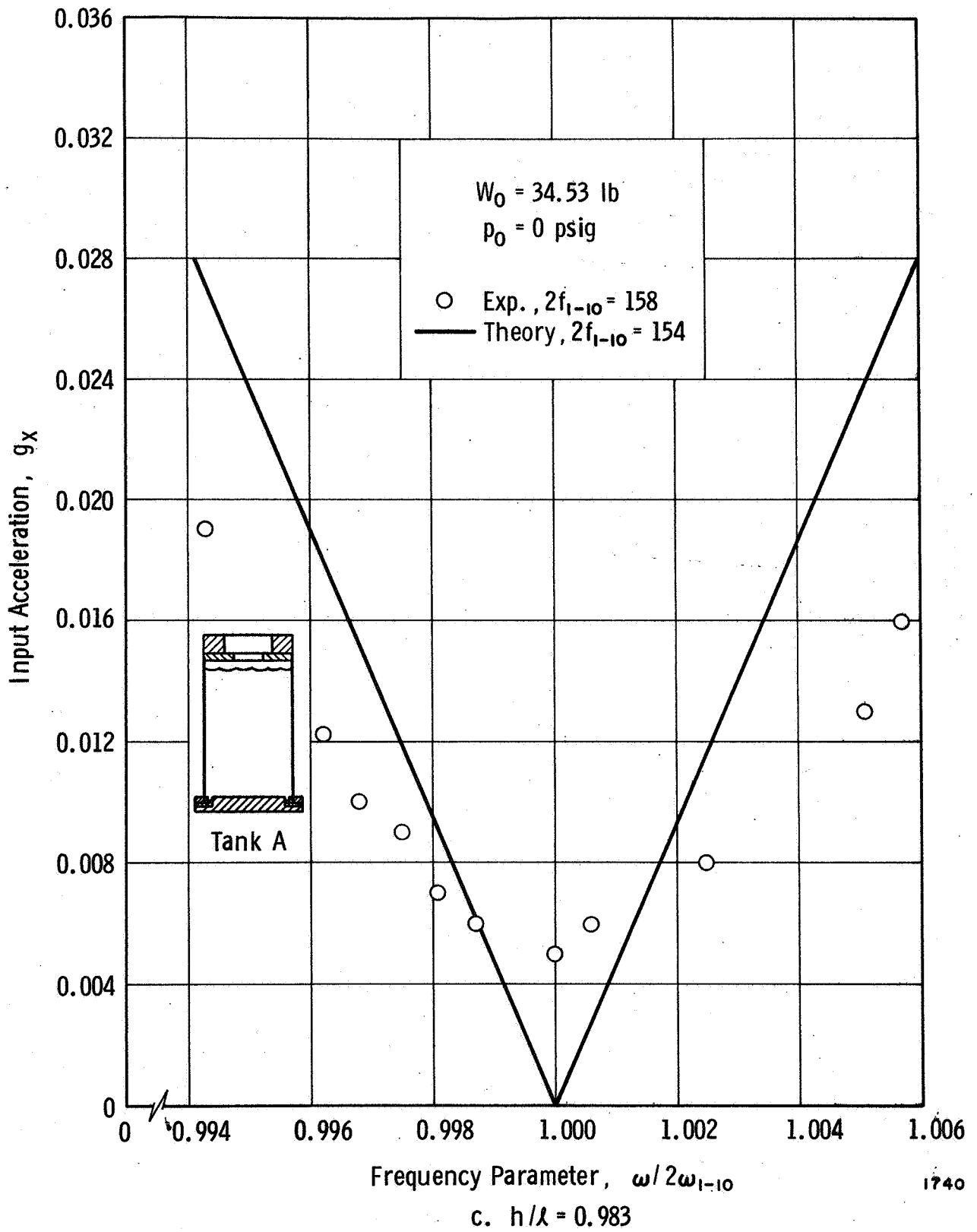
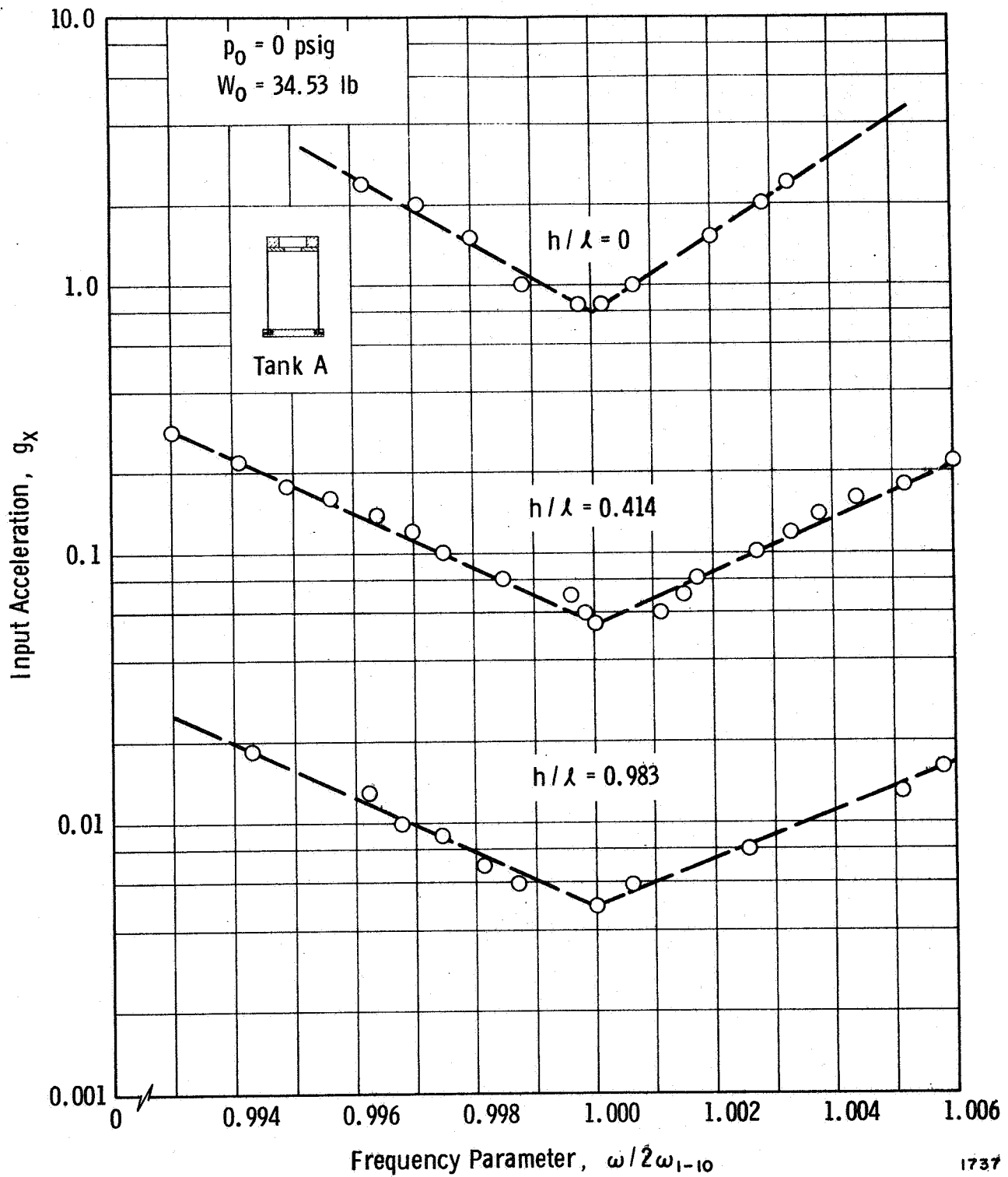


Figure 9. Influence Of Liquid Depth On Stability



d. Logarithmic Plot

Figure 9. Influence Of Liquid Depth On Stability

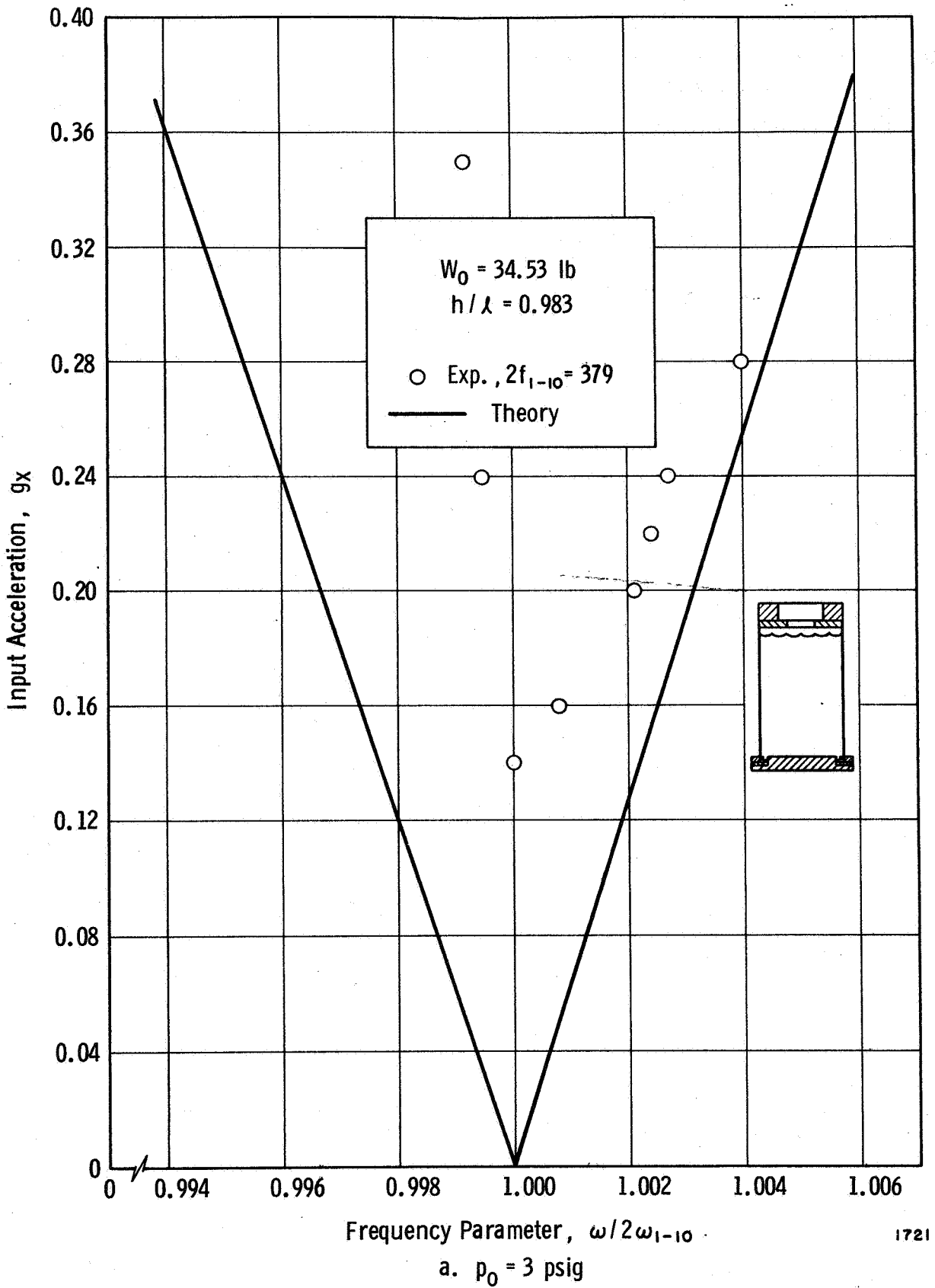
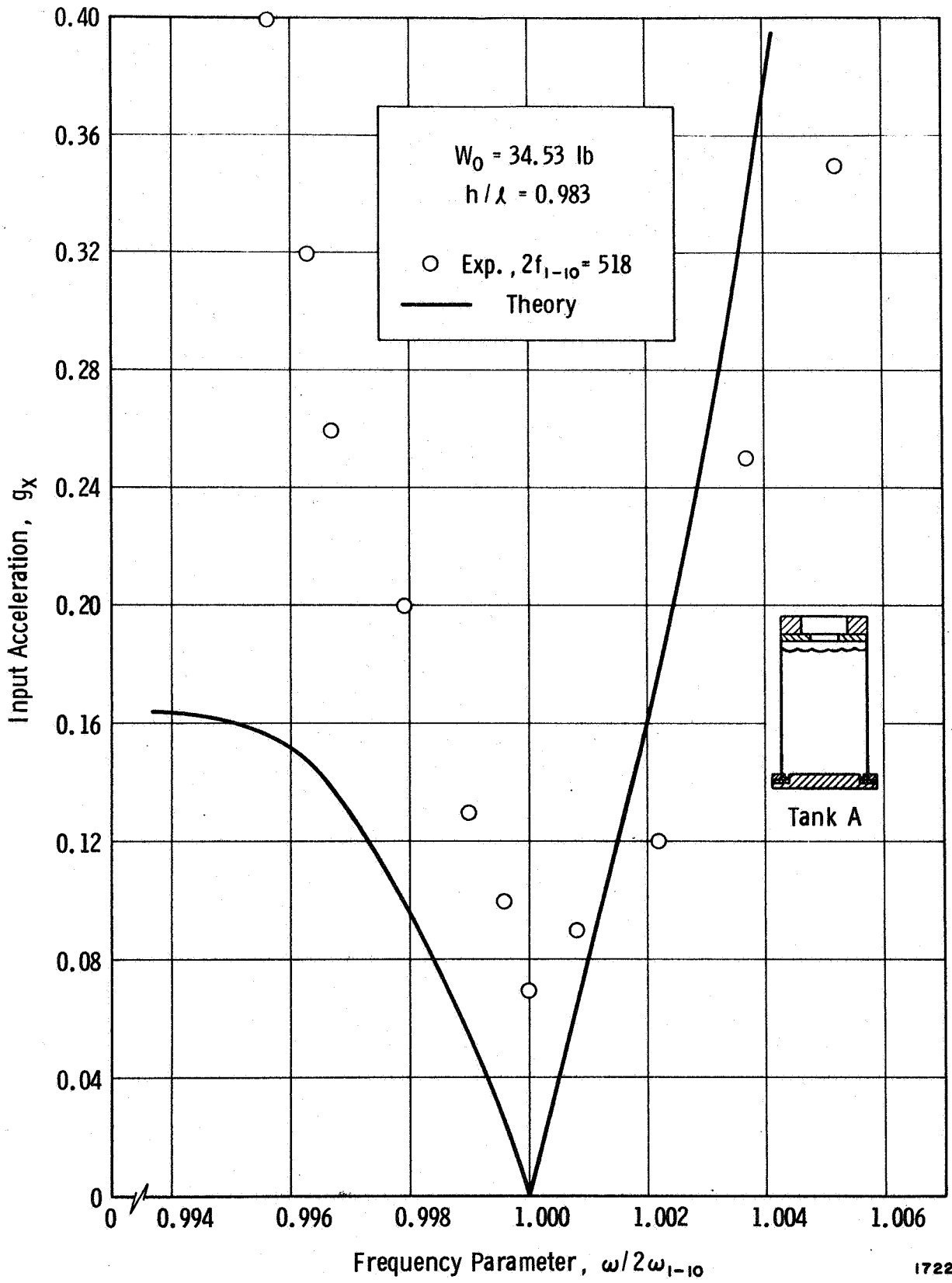


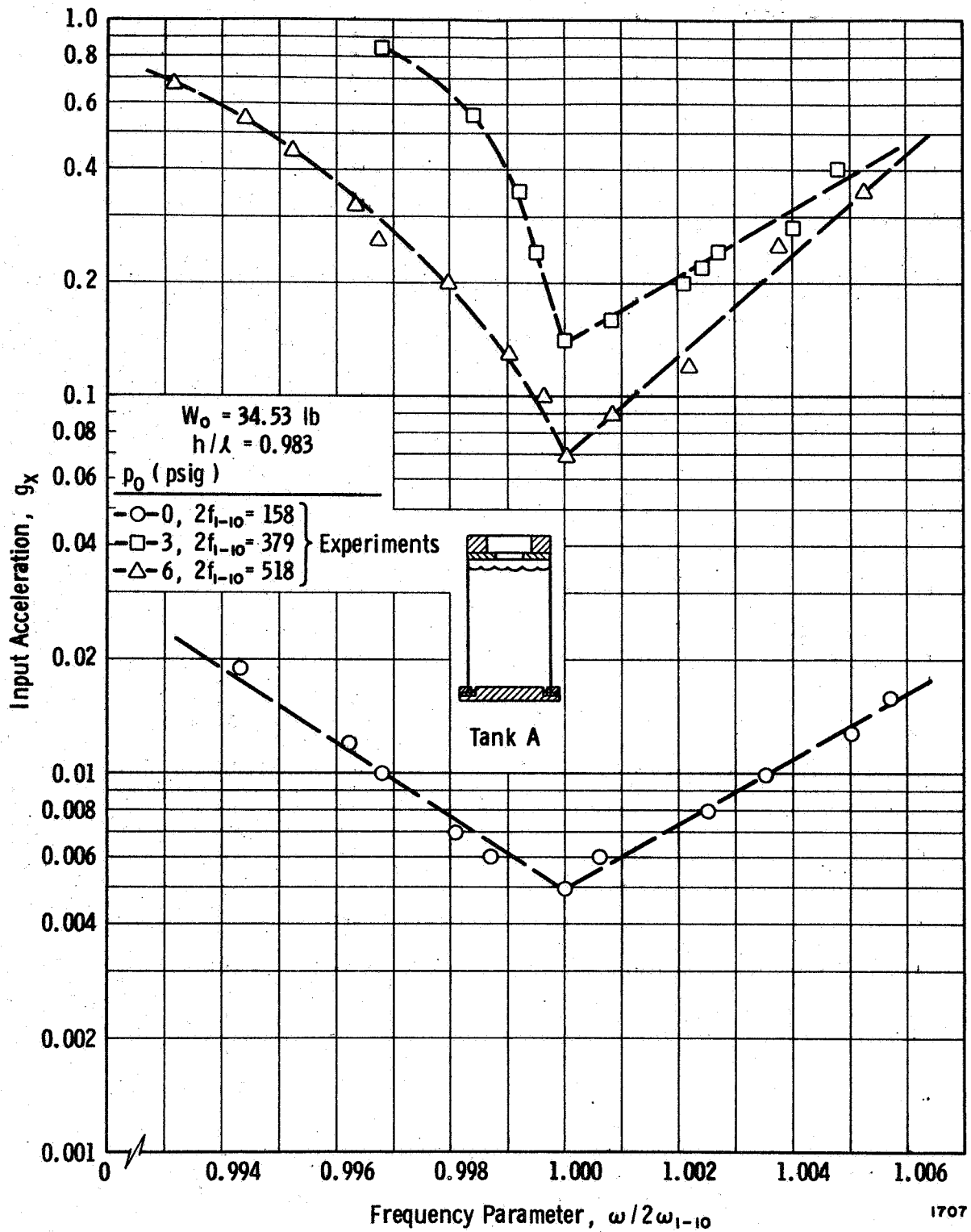
Figure 10. Influence Of Ullage Pressure On Stability



1722

b.  $p_0 = 6 \text{ psig}$

Figure 10. Influence Of Ullage Pressure On Stability



c. Logarithmic Plot

Figure 10. Influence Of Ullage Pressure On Stability

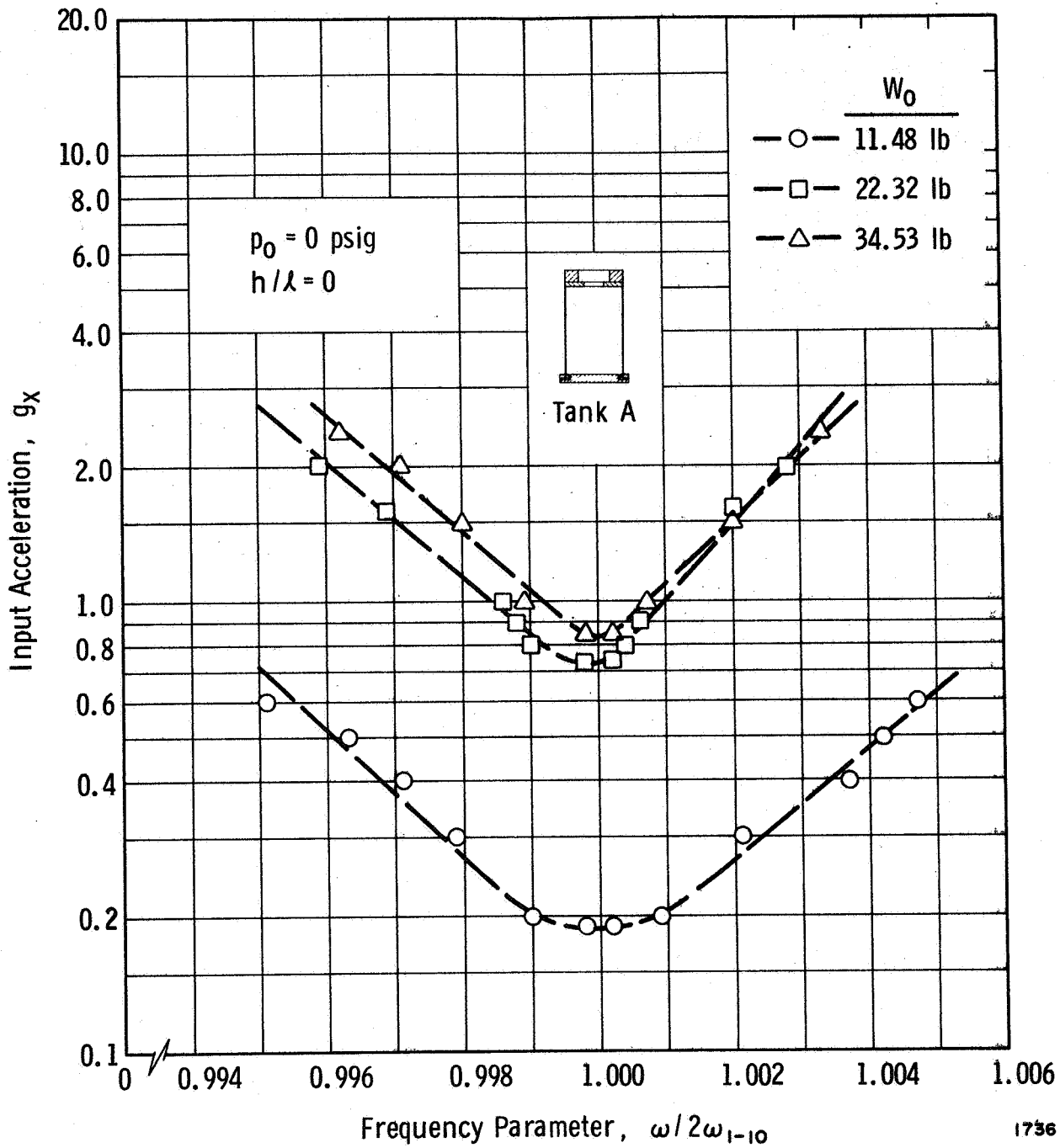


Figure 11. Influence Of Top Mass On Stability



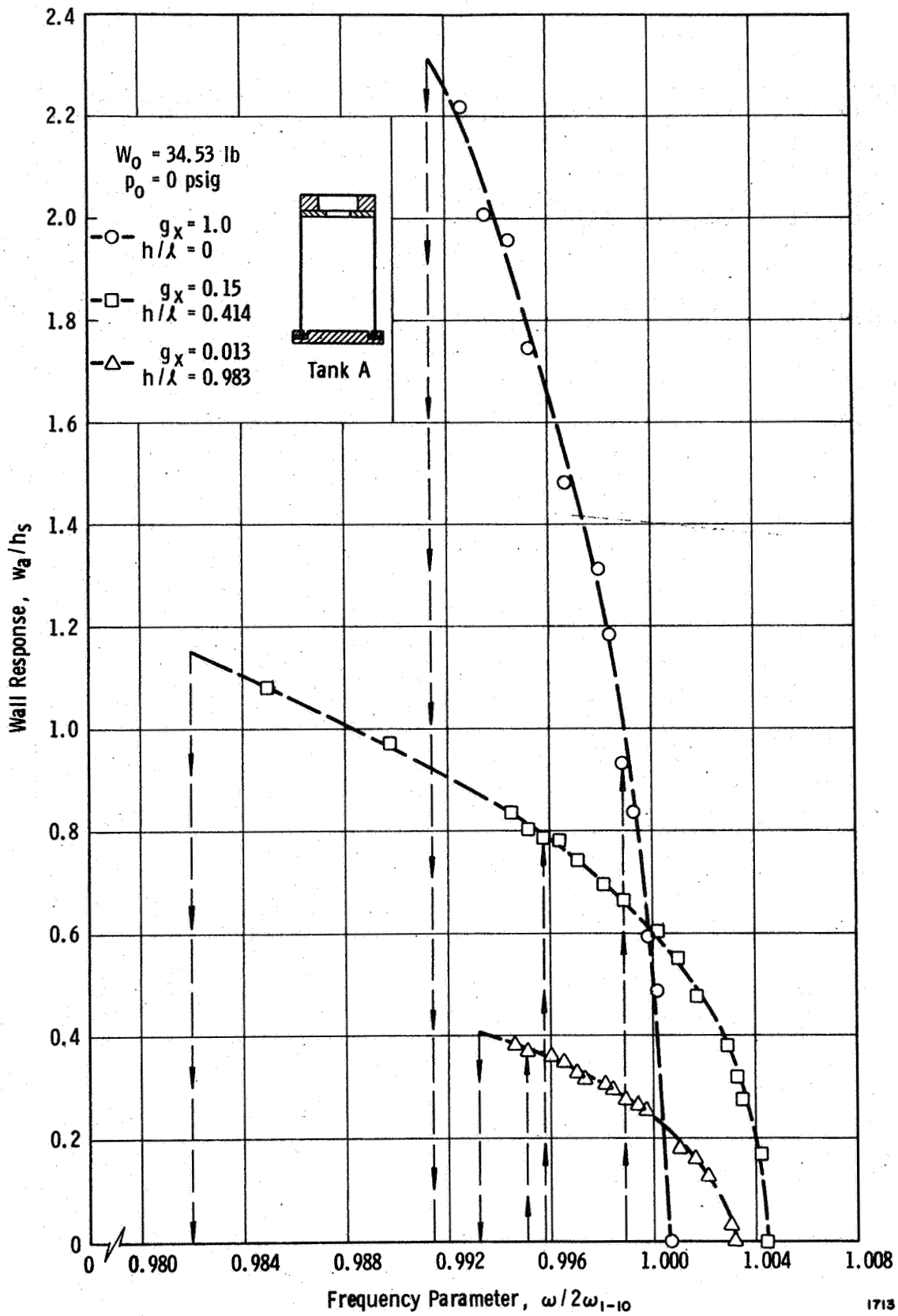


Figure 12. Influence Of Liquid Depth On Subharmonic Wall Response

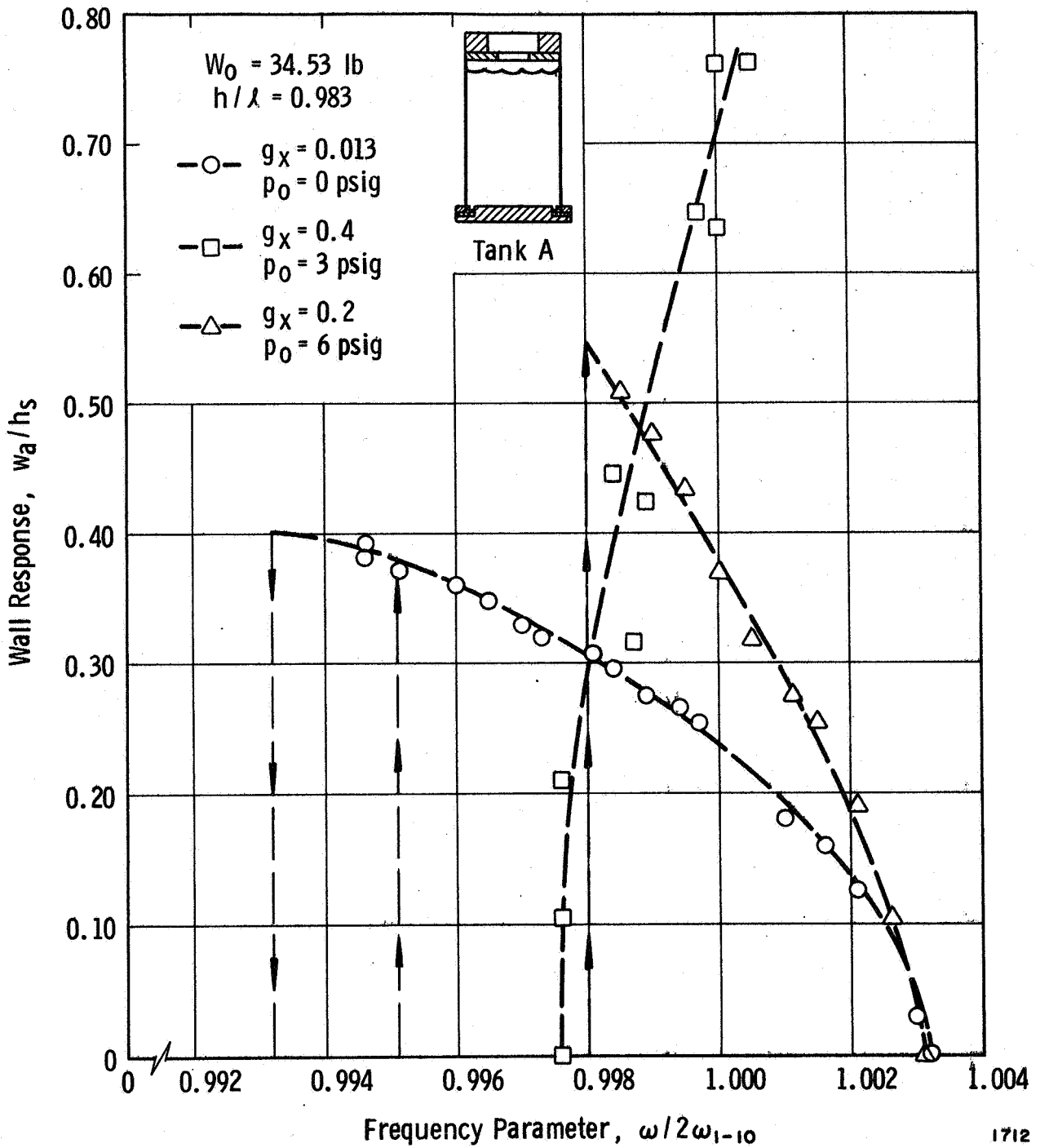


Figure 13. Influence Of Ullage Pressure On Subharmonic Wall Response

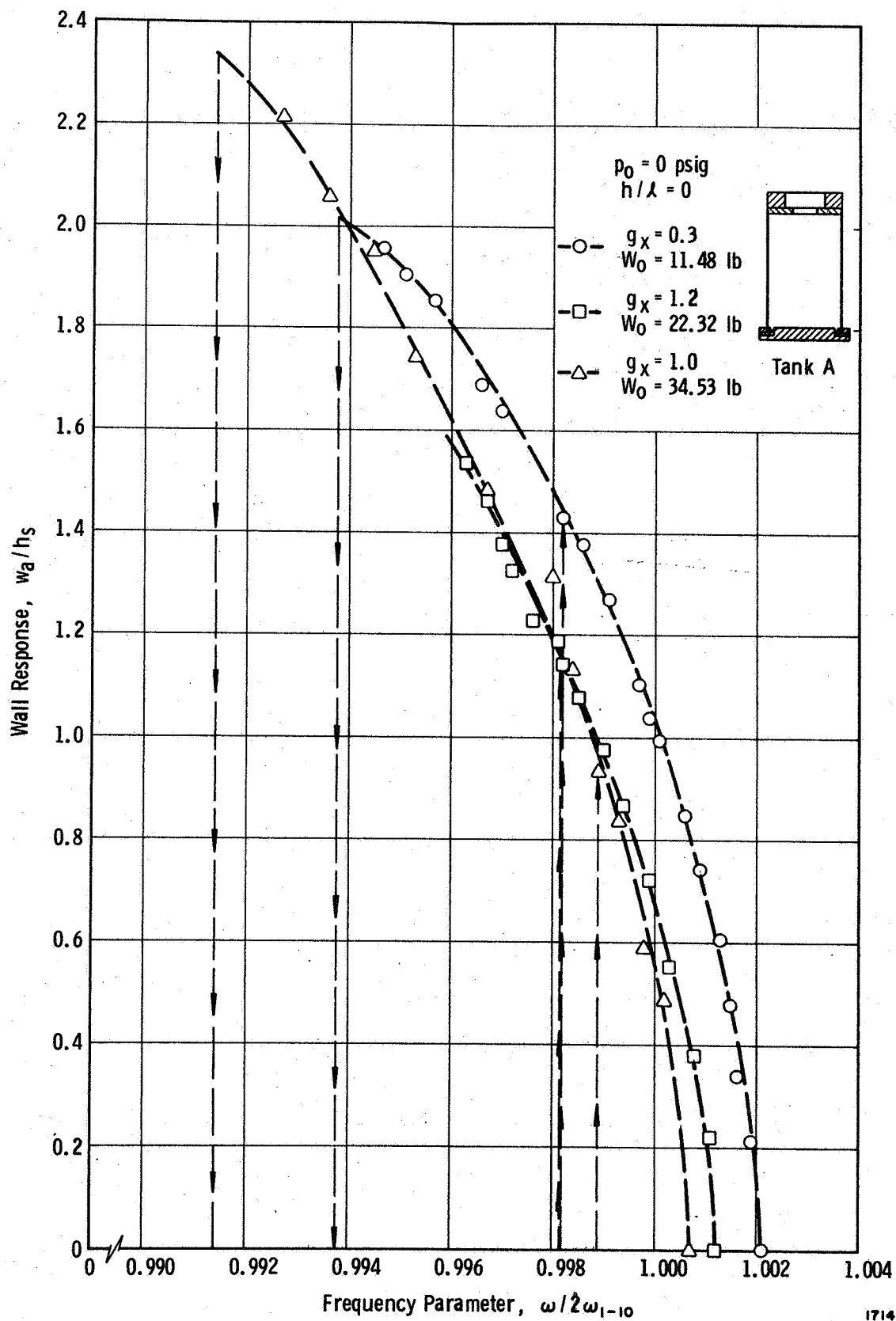
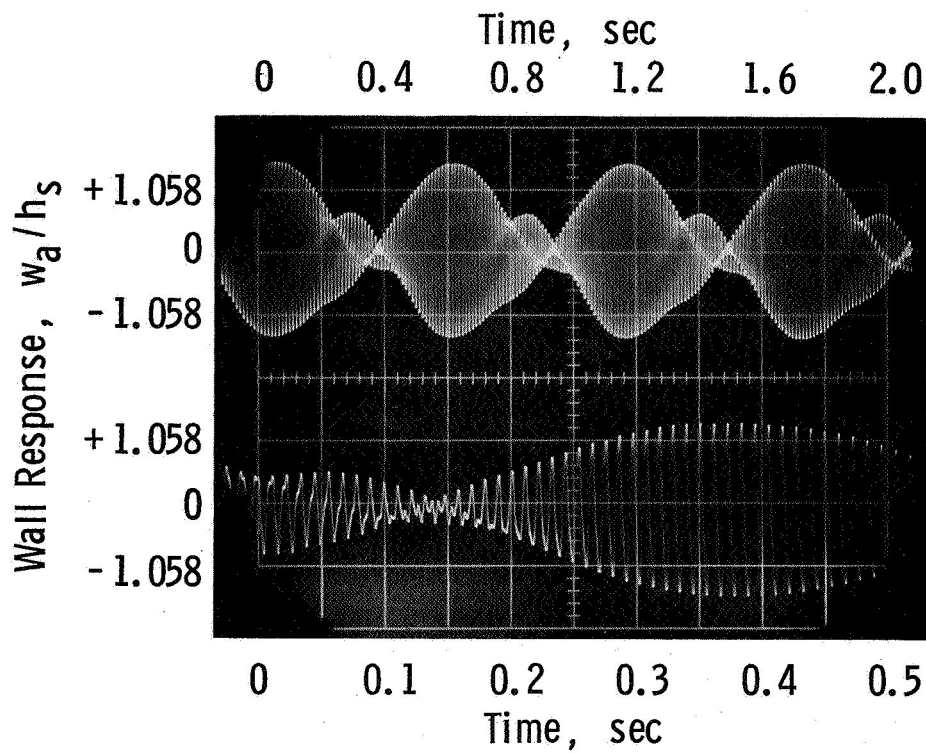


Figure 14. Influence Of Top Mass On Subharmonic Wall Response



1731

$W_0 = 34.53 \text{ lb}$   
 $h/\lambda = 0.414$   
 $p_0 = 0 \text{ psig}$   
 $g_x = 0.4$   
 $f = 197.3 \text{ cps}$   
 $2f_{1-10} = 197 \text{ cps}$



Tank A

Figure 15. Nonlinear Coupling Of Tank Wall And Liquid Surface

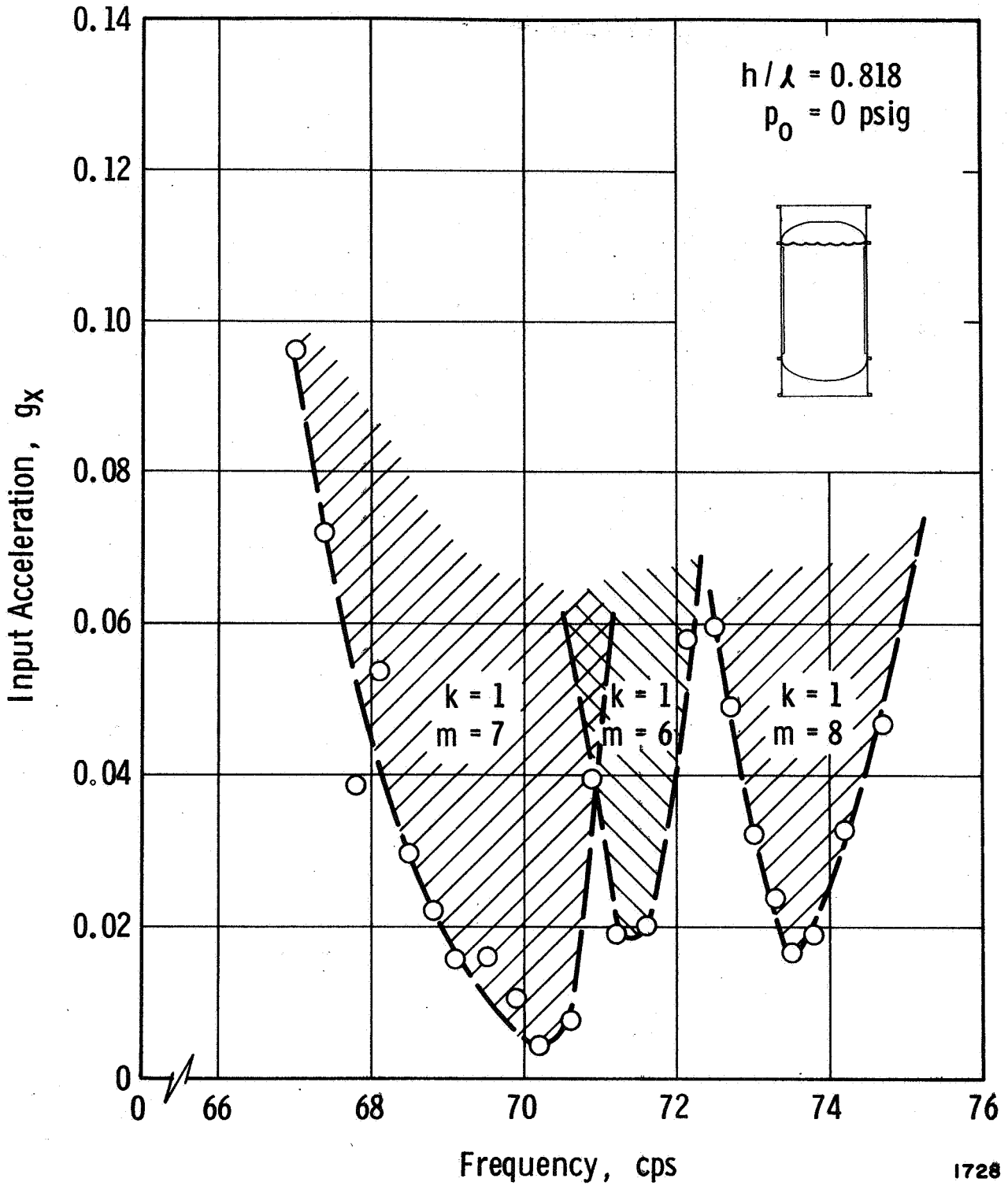
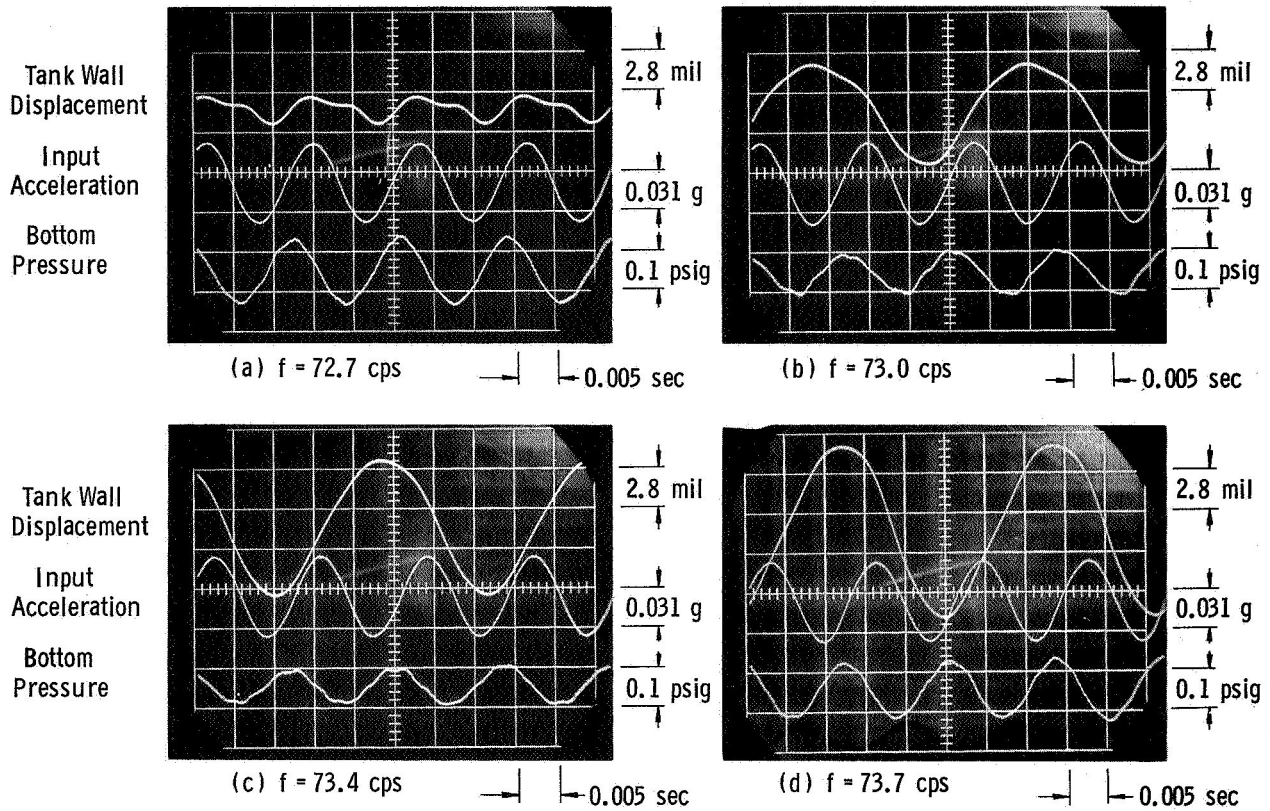
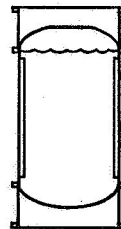


Figure 16. Stability Boundaries For Tank S-0



$p_0 = 0$  psig  
 $h/\lambda = 0.818$   
 $k = 1$   
 $m = 8$



1735

Figure 17. Nonlinear Response For Tank S-0

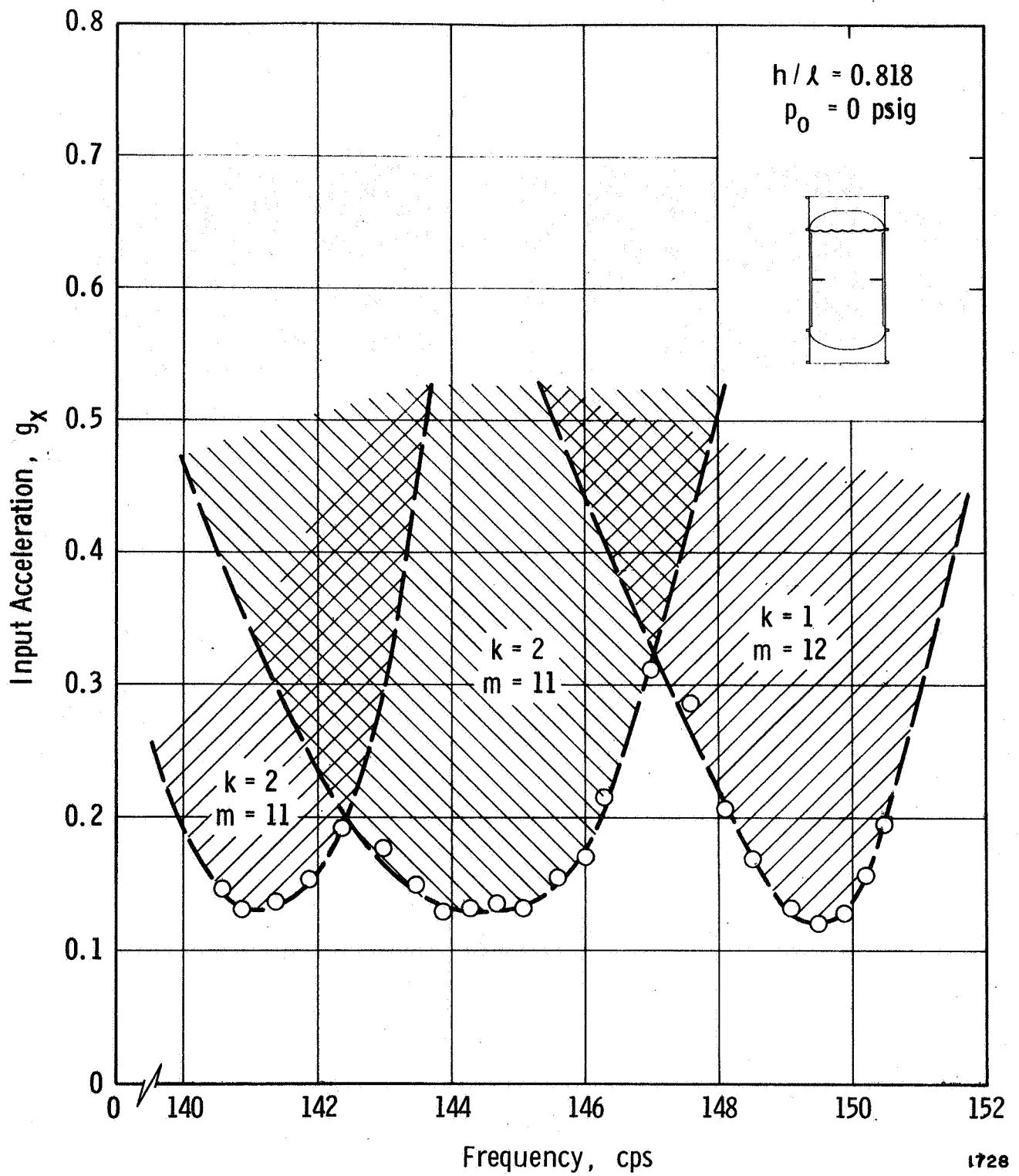


Figure 18. Stability Boundaries For Tank S-1

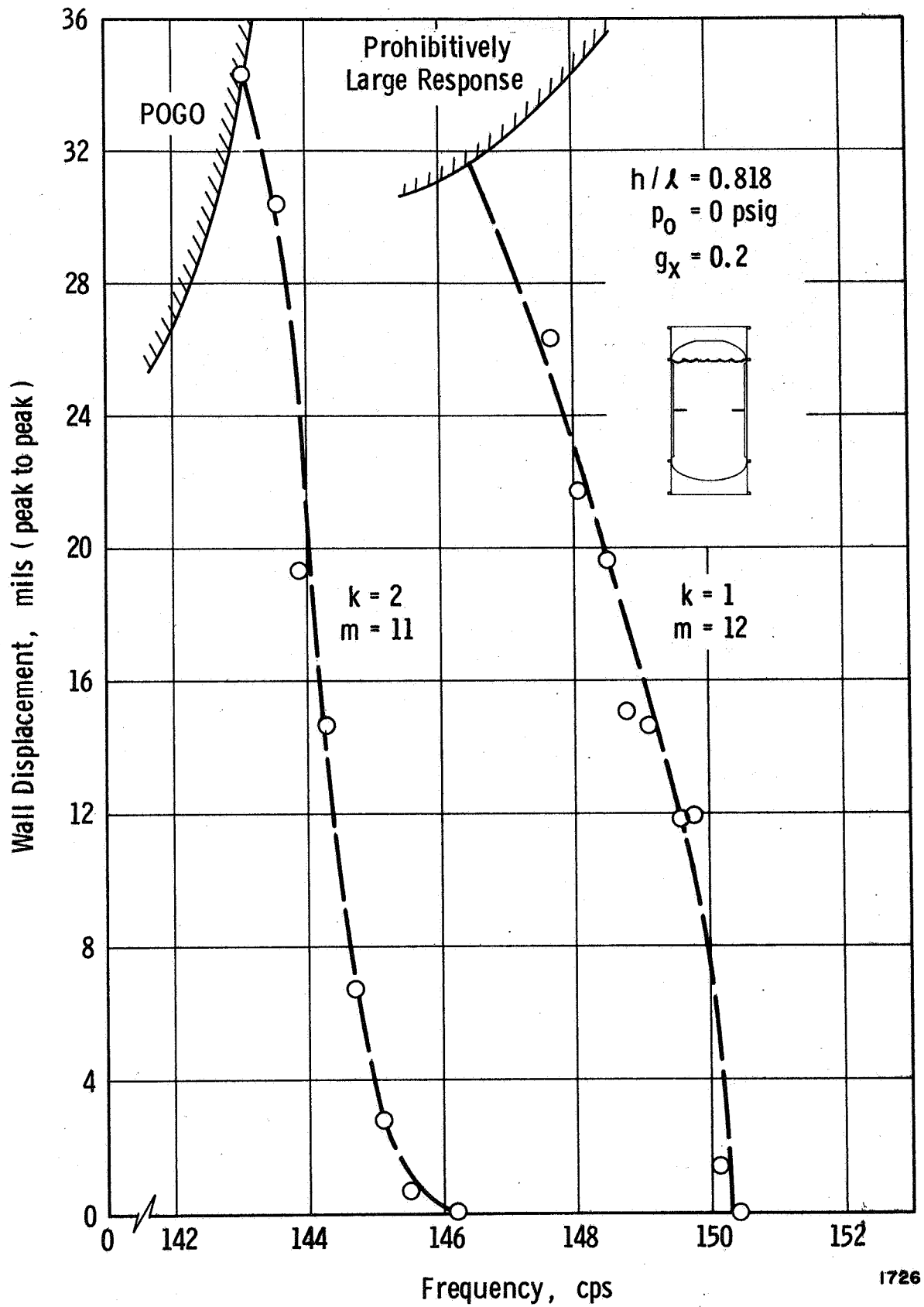
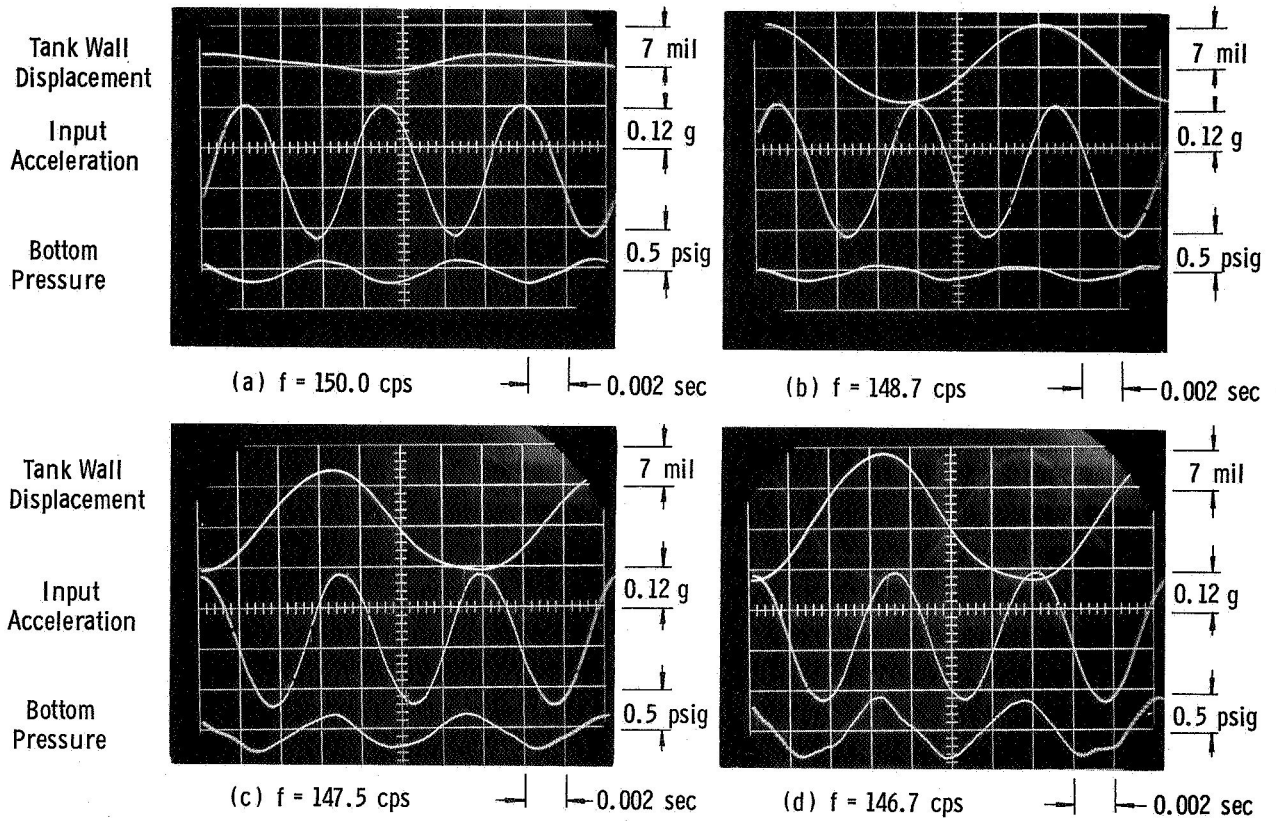


Figure 19. Nonlinear Wall Response For Tank S-1





1733

$p_0 = 0$  psig  
 $h/\lambda = 0.818$   
 $k = 1$   
 $m = 12$

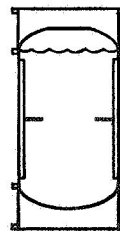
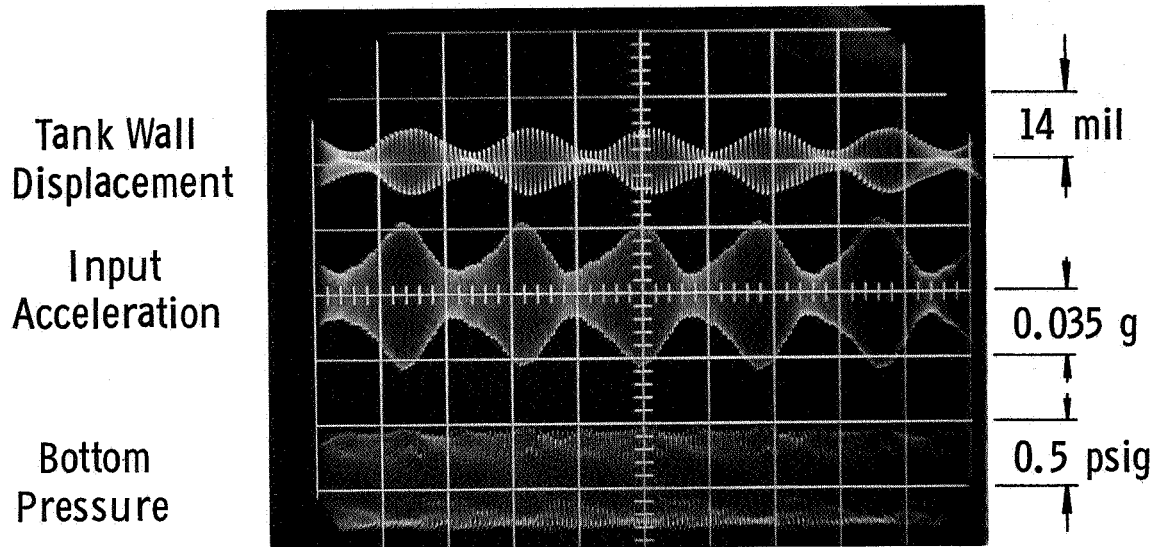


Figure 20. Nonlinear Response For Tank S-1



$f = 140.0 \text{ cps}$

0.100 sec

$p_0 = 0 \text{ psig}$   
 $h / \lambda = 0.818$



1732

Figure 21. POGO Behavior For Tank S-1

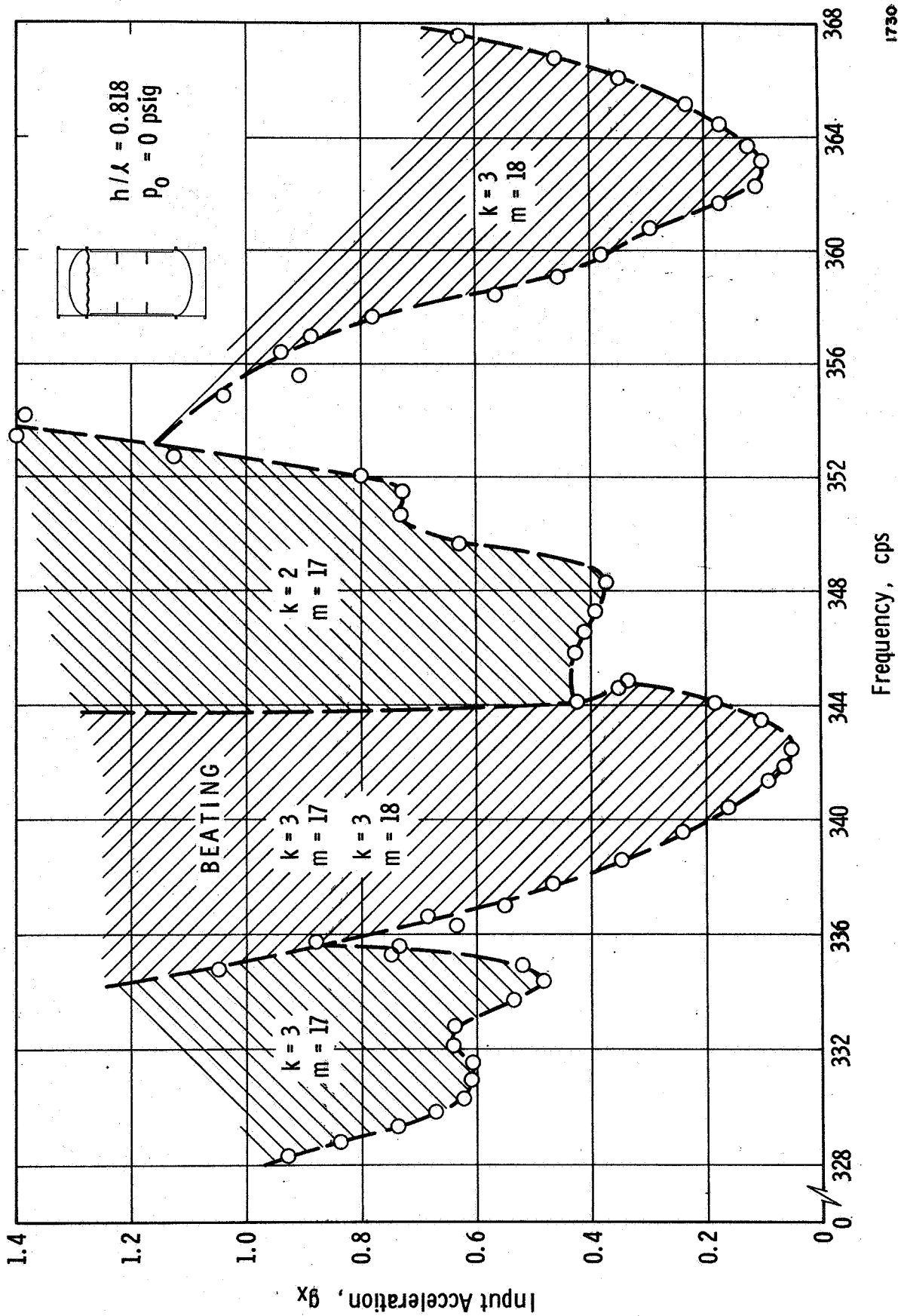
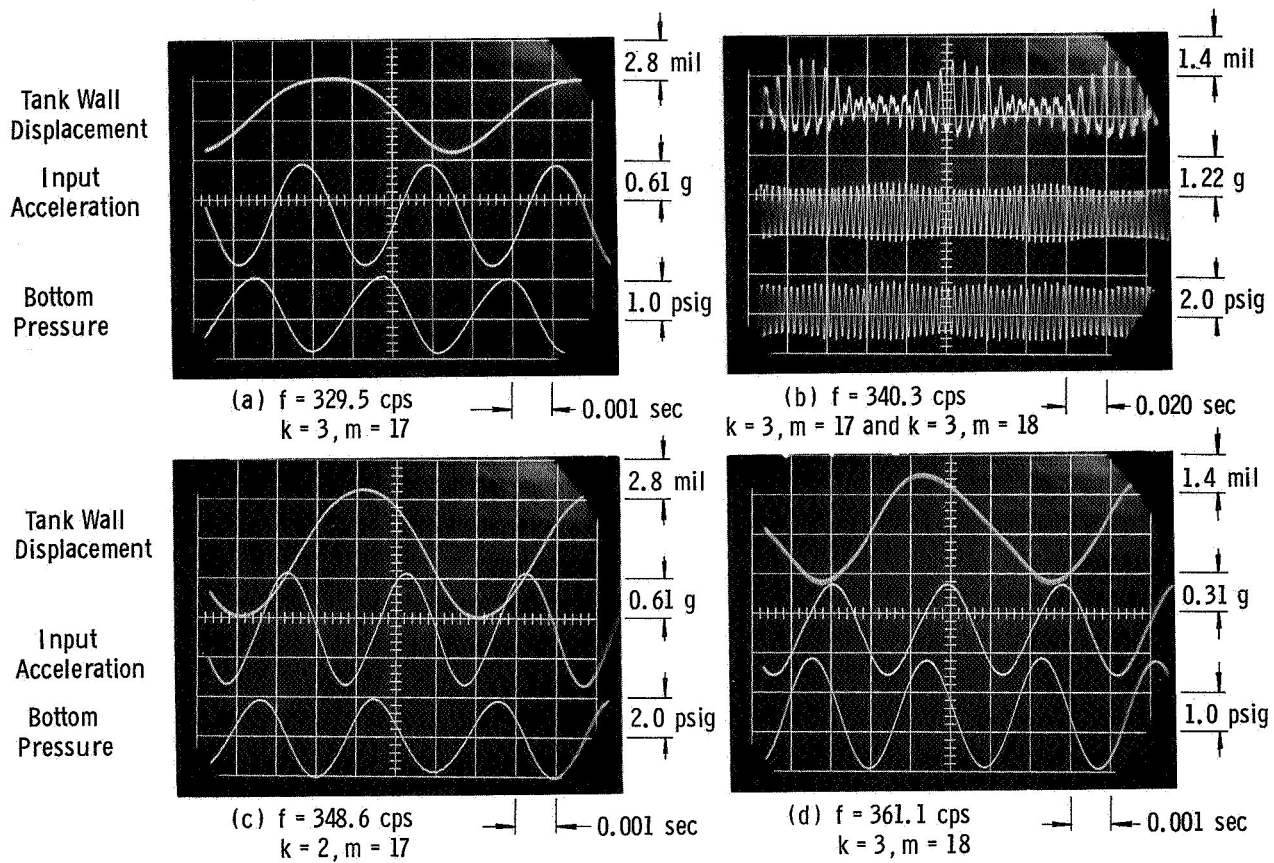
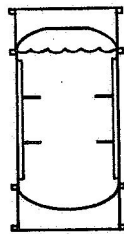


Figure 22. Stability Boundaries For Tank S-2



$p_0 = 0$  psig  
 $h/\lambda = 0.818$



1734

Figure 23. Nonlinear Response For Tank S-2



APPENDIX A  
THEORETICAL EXPRESSIONS

PRECEDING PAGE BLANK NOT FILMED.

APPENDIX A

A.1 Elements of Square Submatrices in Equation (12)

$$R_{1n'n} = \delta_{n'n} + M_{mn'n}, \quad S_{1n'n} = 0, \quad T_{1n'n} = 0$$

$$R_{2n'n} = 0, \quad S_{2n'n} = \frac{1}{2} N_{2mn} \chi_{2n'} + N_{1mn} \chi_{1n'} + \delta_{n'n}, \quad T_{2n'n} = 0$$

$$R_{3n'n} = 0, \quad S_{3n'n} = 0, \quad T_{3n'n} = \delta_{n'n}$$

$$U_{1n'n} = \left[ 1 + \frac{H_s^2}{12} (\lambda_n^2 + m^2)^2 \right] \delta_{n'n} + \frac{1-\nu^2}{H_s} \left\{ \frac{p_0}{E} \left( \frac{\lambda_n^2}{2} + m^2 \right) \delta_{n'n} - \frac{Mg\lambda_n^2}{2\pi a^2 E} \delta_{n'n} + \frac{\rho g a}{E} m^2 \chi_{3n'n} \right\}$$

$$V_{1n'n} = \nu [\tilde{\chi}_{1n'} N_{2mn} + \tilde{\chi}_{0n'} N_{1mn} - \lambda_n \delta_{n'n}]$$

$$W_{1n'n} = m \delta_{n'n}$$

$$U_{2n'n} = -\nu \lambda_n \delta_{n'n}$$

$$V_{2n'n} = \left( \lambda_n^2 + \frac{1-\nu}{2} m^2 \right) \delta_{n'n} + \frac{m^2(1-\nu)}{2} \left( \frac{1}{2} N_{2mn} \chi_{2n'} + N_{1mn} \chi_{1n'} \right)$$

$$W_{2n'n} = -\frac{1+\nu}{2} m \lambda_n \delta_{n'n}$$

$$U_{3n'n} = m \delta_{n'n}$$

$$V_{3n'n} = \frac{1+\nu}{2} m (\tilde{\chi}_{1n'} N_{2mn} + \tilde{\chi}_{0n'} N_{1mn}) - m \frac{1+\nu}{2} \lambda_n \delta_{n'n}$$

$$W_{3n'n} = \left( \frac{1-\nu}{2} \lambda_n^2 + m^2 \right) \delta_{n'n}$$

A.2 Coefficients for Equations (21) through (23)

Coefficients for Equation (21):

$$n \geq 1$$

$$U_{2n'n} = -\nu \lambda_n \delta_{n'n} ,$$

$$V_{2n'n} = \left( \lambda_n^2 + \frac{1-\nu}{2} m^2 \right) \delta_{n'n} + m \frac{1-\nu}{2} \left( \frac{1}{2} N_{2mn} \chi_{2n} + N_{1mn} \chi_{1n} \right)$$

$$W_{2n'n} = -\frac{1+\nu}{2} m \lambda_n \delta_{n'n} , \quad R_{2n'n} = 0 , \quad T_{2n'n} = 0$$

$$S_{2n'n} = \frac{1}{2} N_{2mn} \chi_{2n} \delta_{n'n} + N_{1mn} \chi_{1n} \delta_{n'n} + \delta_{n'n}$$

$$F_{an'} = \left\{ -m^2 \frac{1-\nu}{2} \left( \frac{1}{2} X_{m2} \chi_{2n'} + X_{m1} \chi_{1n'} \right) + (1-\nu^2) \Omega^2 \left[ X_{m2} \frac{\chi_{2n'}}{2} + X_{m1} \chi_{1n'} \right] \right\}$$

Coefficients for Equation (22):

$$U_{3n'n} = m \delta_{n'n} , \quad V_{3n'n} = m \frac{1+\nu}{2} [N_{2mn} \tilde{\chi}_{1n'} + N_{1mn} \tilde{\chi}_{0n'} - \lambda_n \delta_{n'n}]$$

$$W_{3n'n} = \left( \frac{1-\nu}{2} \lambda_n^2 + m^2 \right) \delta_{n'n} , \quad R_{3n'n} = 0 , \quad S_{3n'n} = 0 , \quad T_{3n'n} = \delta_{n'n}$$

$$F_{cn'} = -m \frac{1+\nu}{2} [X_{m2} \tilde{\chi}_{1n'} + X_{m1} \tilde{\chi}_{0n'}]$$

Coefficients for Equation (23):

$$U_1 = \delta_{n'n} + \frac{H_s^2}{12} (\lambda_n^2 + m^2)^2 \delta_{n'n} + \frac{1-\nu^2}{H_s} \left\{ \left[ \left( \frac{\lambda_n^2}{2} + m^2 \right) \frac{p_0}{E} - \frac{Mg}{2\pi a^2 E} \lambda_n^2 \right] \delta_{n'n} + m^2 \frac{\rho g a}{E} \chi_{3n'n} \right\}$$

$$V_1 = \nu [N_{2mn} \tilde{\chi}_{1n'} + N_{1mn} \tilde{\chi}_{0n'} - \lambda_n \delta_{n'n}] , \quad W_1 = m \delta_{n'n} , \quad R_1 = \delta_{n'n} + M_{mn'n}$$

$$S_1 = 0 , \quad T_1 = 0 , \quad F_{rn'} = -\nu [X_{m2} \tilde{\chi}_{1n'} + X_{m1} \tilde{\chi}_{0n'}] + (1-\nu^2) \hat{Q}_{0n'}^B$$



A.3 Elements of  $n \times 1$  Column Submatrices in Equations (27)

$$\hat{A}_{mn}^p = \frac{A_{mn}^p}{X_0} , \quad \hat{B}_{mn}^p = \frac{B_{mn}^p}{X_0} , \quad \hat{C}_{mn}^p = \frac{C_{mn}^p}{X_0}$$

$$\hat{F}_{r_n} = F_{r_n} , \quad \hat{F}_{a_n} = F_{a_n} , \quad \hat{F}_{c_n} = F_{c_n}$$

A.4 Elements of the Matrices in Equations (40)

Elements of  $[M_1]$ :

$$\tilde{M}_{1n'k} = \tilde{\Omega}^2 \sum_{n=1}^N [\delta_{n'n} + M_{mn'n}(\Omega)] A_{mn_k}$$

Elements of  $[M_2]$ :

$$M_{2n'k} = \tilde{\Omega}^2 \sum_{n=1}^N \left[ \frac{1}{2} B_{2k} \chi_{2n'} + B_{1k} \chi_{1n'} + B_{mn_k} \delta_{n'n} \right]$$

Elements of  $[M_3]$ :

$$M_{3n'k} = \tilde{\Omega}^2 \sum_{n=1}^N C_{mn_k} \delta_{n'n}$$

Elements of  $[K_1]$ :

$$K_{1n'k} = \tilde{\Omega}_k^2 \sum_{n=1}^N [\delta_{n'n} + M_{mn'n}(\Omega_k)] A_{mn_k}$$

Elements of  $[K_2]$ :

$$K_{2n'k} = \tilde{\Omega}_k^2 \sum_{n=1}^N \left[ \frac{1}{2} B_{2k} \chi_{2n'} + B_{1k} \chi_{1n'} + B_{mn_k} \delta_{n'n} \right]$$

Elements of  $[K_3]$ :

$$K_{3n'k} = \tilde{\Omega}_k^2 \sum_{n=1}^N C_{mn_k} \delta_{n'n}$$

Elements of  $[T_1]$ :

$$T_{1n'k} = \sum_{n=1}^N \left[ \sum_{n''=1}^N \left( N_{1n''} \lambda_n^2 + \lambda_n N_{3n''} \frac{e_{n''n'n}}{d_{n''n'n}} + m^2 N_{2n''} \right) d_{n''n'n} + \lambda_n \tilde{B}_2^p e_{0n'} \right] A_{mnk}$$

Elements of  $[T_2]$ :

$$T_{2n'k} = 0$$

Elements of  $[T_3]$ :

$$T_{3n'k} = 0$$

where, for each of the above matrices,

$$n' = 1 \text{ to } N$$

$$k = 1 \text{ to } 3N$$

A. 5. The first five roots\* of the equation in

$$J'_m(\mu_{mj}) = 0 \quad , \quad m = 10$$

<u>j</u>	<u><math>\mu_{mj}</math></u>
1	11.77088
2	16.44785
3	20.22304
4	23.76071
5	27.18202

---

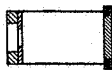
\*These roots are obtained by interpolation with a Bessel function subroutine accurate to five or six figures. In addition, the first five roots for  $m = 0$  to 8 are given in W. H. Chu, "Breathing Vibrations of a Partially Filled Cylindrical Shell-Linear Theory," J. Appl. Mech., Vol. 30, No. 4, pp. 532-536, December 1963.



APPENDIX B  
EXPERIMENTAL DATA FOR TANK A

PRECEDING PAGE BLANK NOT FILMED

TABLE B.1. EXPERIMENTAL NATURAL FREQUENCIES OF  
PARTIALLY FILLED TANK



(Tank A)

Liquid Depth: $h/L$ ; $W_0 = 34.53 \text{ lb}$		14.25	14.0	12.25	12.0	10.0	8.0	7.5	7.0	6.0	5.0	4.0	3.0	2.0	0	Plotted on Fig. No.
Mode $\frac{k}{m}$		0.983	0.966	0.845	0.828	0.690	0.552	0.517	0.483	0.414	0.345	0.276	0.207	0.138	0	
1	10	79	78	-	75	73	81	-	-	99	-	141	-	214	247	6(a)
1	13	115	115	-	110	112	115	-	-	127	-	164	-	288	309	6(a)
1	0	202	202	-	230	262	282*	290	292	296	-	300	297	297	297	6(a)
2	0	320	319	-	320	331	372*	399	405	462	-	630	772	1020	-	6(a)
3	0	549	555	-	622	710	824*	-	-	985	-	-	-	-	-	6(a)
4	0	785	792	-	876	980	-	-	-	-	-	-	-	-	-	6(a)
$W_0 = 22.32 \text{ lb}$																
Mode $\frac{k}{m}$		79 <th>79 <th>-</th> <th>75</th> <th>74</th> <th>81</th> <th>-</th> <th>-</th> <th>99</th> <th>-</th> <th>138</th> <th>-</th> <th>219</th> <th>230</th> <td>6(b)</td> </th>	79 <th>-</th> <th>75</th> <th>74</th> <th>81</th> <th>-</th> <th>-</th> <th>99</th> <th>-</th> <th>138</th> <th>-</th> <th>219</th> <th>230</th> <td>6(b)</td>	-	75	74	81	-	-	99	-	138	-	219	230	6(b)
1	10	116	115	-	112	112	115	-	-	126	-	158	-	-	310	6(b)
1	13	205	206	-	237	276	328*	-	-	359	-	470	-	371	371	6(b)
2	0	392	391	-	391	392	403*	-	-	465	-	621	-	993	-	6(b)
3	0	551	558	-	623	710	823*	-	-	981	-	-	-	-	-	6(b)
4	0	788	797	-	876	978	-	-	-	-	-	-	-	-	-	6(b)
$W_0 = 11.48 \text{ lb}$																
Mode $\frac{k}{m}$		80 <th>79 <th>76</th> <th>-</th> <th>74</th> <th>82</th> <th>-</th> <th>-</th> <th>100</th> <th>-</th> <th>142</th> <th>-</th> <th>222</th> <th>231</th> <td>6(c)</td> </th>	79 <th>76</th> <th>-</th> <th>74</th> <th>82</th> <th>-</th> <th>-</th> <th>100</th> <th>-</th> <th>142</th> <th>-</th> <th>222</th> <th>231</th> <td>6(c)</td>	76	-	74	82	-	-	100	-	142	-	222	231	6(c)
1	10	114	114	113	-	112	115	-	-	127	-	164	-	292	312	6(c)
1	0	199	205	232	-	284	345*	-	-	423	-	476	-	482	489	6(c)
2	0	496	494	495	-	494	498*	-	-	510	-	622	-	781	1020	6(c)
3	0	560	564	614	-	701	825*	-	-	984	-	-	-	-	-	6(c)
4	0	786	793	876	-	977	-	-	-	-	-	-	-	-	-	6(c)

\*Also plotted on Fig. 7.

TABLE B.2. AMPLITUDE AMPLIFICATION

Tank A

$W_0 = 34.53 \text{ lb}$

$p_0 = 10 \text{ psi}$

$h/l = 0.69$



<u>f,</u> <u>cps</u>	<u><math>\hat{u}_l \omega^2 / g_x</math></u>	<u>f,</u> <u>cps</u>	<u><math>\hat{u}_l \omega^2 / g_x</math></u>
241.1	5.6	319.5	1.7
244.2	6.0	320.4	2.7
245.3	6.7	321.2	3.4
248.5	9.0	322.0	5.3
251.7	11.4	322.6	5.3
255.9	19.7	323.6	9.1
257.4	24.6	324.4	16.3
257.7	26.8	325.2	34.2
258.8	39.2	325.6	48.7
259.9	65.9	325.9	8.4
261.4	98.4	326.2	8.9
263.0	56.2	326.3	19.7
264.5	31.9	327.5	15.5
266.5	20.2	328.3	11.5
269.3	12.9	331.6	5.3
272.2	9.0	336.5	3.4
274.3	7.5	340.3	2.9
276.7	6.2	344.6	2.4
281.0	4.6	349.5	2.2
285.1	3.2	356.7	1.8
292.2	2.6	368.6	1.5
295.6	1.7		
300.3	1.6		
303.8	1.2		
308.8	0.5		
310.5	0.2		
311.3	0.3		
311.7	0.9		
313.2	0.1		
314.8	0.6		
316.8	1.4		

Note: Plotted on Figure 8.



TABLE B.3. STABILITY BOUNDARIES

(Tank A)

$k = 1; m = 10$  Mode

$h/l = 0$ (Figs. 9 and 11)		$W_0 = 34.53$ lb; $P_0 = 0$ psi $h/l = 0.414$ (Fig. 9)		$h/l = 0.983$ (Figs. 9 and 10)		$W_0 = 34.53$ lb; $h/l = 0.983$ $P_0 = 3$ psi (Fig. 10)		$P_0 = 6$ psi (Fig. 10)		$W_0 = 11.48$ lb (Fig. 11)		$P_0 = 0$ psi; $h/l = 0$ $W_0 = 22.32$ lb (Fig. 11)	
$\omega/2\omega_{krm}$	$g_x$	$\omega/2\omega_{krm}$	$g_x$	$\omega/2\omega_{krm}$	$g_x$	$\omega/2\omega_{krm}$	$g_x$	$\omega/2\omega_{krm}$	$g_x$	$\omega/2\omega_{krm}$	$g_x$	$\omega/2\omega_{krm}$	$g_x$
0.9962	2.4	0.9930	0.28	0.9943	0.019	0.9968	0.84	0.9931	0.67	0.9951	0.6	0.9959	2.0
0.9971	2.0	0.9941	0.22	0.9962	0.012	0.9984	0.56	0.9944	0.55	0.9963	0.5	0.9969	1.6
0.9980	1.5	0.9949	0.18	0.9968	0.010	0.9992	0.35	0.9952	0.45	0.9971	0.4	0.9981	1.3
0.9989	1.0	0.9956	0.16	0.9975	0.009	0.9995	0.24	0.9963	0.32	0.9979	0.3	0.9986	1.0
0.9998	0.85	0.9964	0.14	0.9981	0.007	1.0000	0.14	0.9967	0.26	0.9990	0.2	0.9988	0.9
1.0002	0.85	0.9970	0.12	0.9987	0.006	1.0008	0.16	0.9979	0.20	0.9998	0.19	0.9990	0.8
1.0007	1.0	0.9975	0.10	1.0000	0.005	1.0021	0.20	0.9990	0.13	1.0002	0.19	0.9998	0.74
1.0020	1.5	0.9985	0.08	1.0006	0.006	1.0024	0.22	0.9996	0.10	1.0009	0.2	1.0002	0.74
1.0029	2.0	0.9996	0.07	1.0025	0.008	1.0027	0.24	1.0000	0.07	1.0021	0.3	1.0004	0.8
1.0033	2.4	0.9998	0.06	1.0050	0.013	1.0040	0.28	1.0008	0.09	1.0037	0.4	1.0006	0.9
		1.0000	0.055	1.0057	0.016	1.0048	0.40	1.0021	0.12	1.0042	0.5	1.0009	1.0
		1.0011	0.06					1.0037	0.25	1.0047	0.6	1.0015	1.3
		1.0015	0.07					1.0052	0.35			1.0020	1.6
		1.0017	0.08									1.0028	2.0
		1.0027	0.10										
		1.0033	0.12										
		1.0038	0.14										
		1.0044	0.16										
		1.0052	0.18										
		1.0060	0.22										

TABLE B. 4. SUBHARMONIC WALL RESPONSE



(Tank A)

k = 1; m = 10 Mode

		$W_0 = 34.53 \text{ lb}; p_0 = 0 \text{ psi}$				$W_0 = 34.53 \text{ lb}; h/l = 0.983$				$p_0 = 0 \text{ psi}; h/l = 0$			
		$g_x = 1.0$ $h/l = 0$ (Figs. 12 and 14)		$g_x = 0.15$ $h/l = 0.414$ (Fig. 12)		$g_x = 0.013$ $h/l = 0.983$ (Figs. 12 and 13)		$g_x = 0.4$ $p_0 = 3 \text{ psi}$ (Fig. 13)		$g_x = 0.2$ $p_0 = 6 \text{ psi}$ (Fig. 13)		$g_x = 0.3$ $W_0 = 11.48$ (Fig. 14)	
$\omega/2\omega_{kn}$	$w_a/h_s$	$\omega/2\omega_{kn}$	$w_a/h_s$	$\omega/2\omega_{kn}$	$w_a/h_s$	$\omega/2\omega_{kn}$	$w_a/h_s$	$\omega/2\omega_{kn}$	$w_a/h_s$	$\omega/2\omega_{kn}$	$w_a/h_s$	$\omega/2\omega_{kn}$	$w_a/h_s$
1.0007	0	1.0044	0	1.0032	0	0.9976	0	1.0031	0	0.9938	0	0.9963	1.535
1.0002	0.487	1.0042	0.169	1.0030	0.032	0.9976	0.106	1.0026	0.106	0.9947	1.958	0.9967	1.460
0.9998	0.593	1.0035	0.275	1.0021	0.127	0.9976	0.212	1.0021	0.191	0.9951	1.905	0.9970	1.376
0.9993	0.836	1.0033	0.318	1.0016	0.159	0.9984	0.445	1.0015	0.254	0.9957	1.852	0.9972	1.323
0.9989	0.931	1.0029	0.381	1.0010	0.180	0.9987	0.317	1.0011	0.275	0.9966	1.693	0.9976	1.270
0.9984	1.185	1.0017	0.476	0.9997	0.254	0.9989	0.423	1.0005	0.318	0.9970	1.640	0.9981	1.185
0.9980	1.312	1.0010	0.550	0.9994	0.265	0.9997	0.646	1.0000	0.370	0.9982	1.429	0.9982	1.143
0.9967	1.482	1.0002	0.603	0.9989	0.275	1.0000	0.635	0.9995	0.434	0.9986	1.376	0.9985	1.079
0.9953	1.746	0.9989	0.667	0.9984	0.296	1.0000	0.762	0.9990	0.476	0.9991	1.270	0.9990	0.974
0.9945	1.958	0.9981	0.699	0.9981	0.307	1.0005	0.762	0.9985	0.508	0.9997	1.101	0.9994	0.868
0.9936	2.064	0.9971	0.741	0.9973	0.318	1.0005	0.116	0.9980	Beat-	0.9999	1.037	0.9999	0.720
0.9927	2.222	0.9964	0.783	0.9970	0.328	1.0005	0	0.9980	ing	1.0001	0.995	1.0003	0.550
0.9914	0	0.9958	0.783	0.9965	0.349	1.0005	0	0.9980	0	1.0006	0.847	1.0008	0.381
		0.9952	0.804	0.9960	0.360					1.0009	0.741	1.0011	0.222
		0.9945	0.836	0.9951	0.370					1.0013	0.603	1.0012	0
		0.9897	0.974	0.9946	0.381					1.0015	0.476		
		0.9850	1.080	0.9946	0.391					1.0016	0.339		
		0.9820	0	0.9932	0					1.0019	0.212		
										1.0021	0		






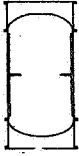
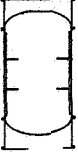
APPENDIX C

EXPERIMENTAL DATA FOR LARGE MODEL WITH STIFFENERS

PRECEDING PAGE BLANK NOT FILMED.

TABLE C.1. STABILITY BOUNDARIES

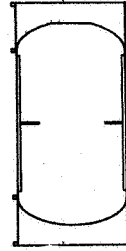
$P_0 = 0$  psi,  $h/l = 0.818$

Tank S-0		Tank S-1		Tank S-2			
							
(Fig. 16)		(Fig. 18)		(Fig. 22)			
Frequency, cps	Input Acceleration, g	Frequency, cps	Input Acceleration, g	Frequency, cps	Input Acceleration, g	Frequency, cps	Input Acceleration, g
67.0	0.0960	140.6	0.146	320.1	1.46	346.6	0.409
67.4	0.0717	140.9	0.131	321.3	1.37	347.3	0.391
67.8	0.0384	141.4	0.137	322.0	1.31	348.3	0.372
68.1	0.0534	141.9	0.153	324.1	1.27	348.9	0.421
68.5	0.0293	142.4	0.192	325.2	0.98	349.7	0.625
68.8	0.0214	143.0	0.177	326.0	0.83	350.7	0.732
69.1	0.0156	143.5	0.149	327.1	0.854	351.5	0.726
69.5	0.0159	143.9	0.128	327.8	0.945	352.0	0.800
69.9	0.0101	144.3	0.131	328.3	0.930	352.8	1.128
70.2	0.0043	144.7	0.134	328.8	0.838	353.5	1.401*
70.6	0.0073	145.1	0.131	329.3	0.738	354.2	1.388*
70.9	0.0397	145.6	0.155	329.8	0.671	354.9	1.038*
71.2	0.0189	146.0	0.171	330.3	0.625	355.6	0.906*
71.6	0.0201	146.3	0.216	330.9	0.610	356.4	0.940*
72.1	0.0580	147.0	0.311	331.5	0.610	357.0	0.885*
72.5	0.0595	147.6	0.286	332.1	0.640	357.7	0.778†
72.7	0.0488	148.1	0.207	332.8	0.640	358.5	0.565†
73.0	0.0317	148.5	0.169	333.7	0.537	359.1	0.451†
73.3	0.0238	149.1	0.131	334.4	0.482	359.9	0.378†
73.5	0.0165	149.5	0.119	334.8	1.050*	360.8	0.293
73.8	0.0189	149.9	0.128	334.9	0.519	361.7	0.171
74.2	0.0327	150.2	0.156	335.3	0.747	362.3	0.110
74.7	0.0465	150.5	0.195	335.6	0.733	363.2	0.098
		151.0	0.195	335.7	0.880*	363.7	0.122
		151.5	0.165	336.3	0.635	364.5	0.171
				336.6	0.687*	365.2	0.229
				337.0	0.550	366.1	0.348
				337.9	0.464*	366.8	0.458
				338.6	0.345*	367.6	0.625
				339.6	0.238*	368.7	0.975
				340.4	0.159*		
				341.4	0.089*		
				341.9	0.063*		
				342.5	0.048*		
				343.5	0.104*		
				344.1	0.183*		
				344.1	0.421		
				344.6	0.348		
				344.9	0.335*		
				345.9	0.427		

\*Beating subharmonic  
 †Large amplitude wall motion

TABLE C.2. SUBHARMONIC WALL RESPONSE

Tank S-1  
 $p_0 = 0$  psi  
 $h/l = 0.818$   
 $g_x = 0.2$



(Fig. 19)

Frequency, cps	Wall Displacement, mils (p-p)
151.9*	--
151.2	2.24
150.7	7.56
150.4*	--
150.1	1.40
149.8	11.90
149.6	11.76
149.1	14.60
148.8	15.00
148.5	19.60
148.1	21.70
147.7	26.30
147.4**	--
146.2*	--
145.5	0.70
145.1	2.80
144.7	6.72
144.3	14.60
143.9	19.32
143.6	30.40
143.1	34.30
142.5†	--
141.9	9.66
141.4	10.92
141.0	11.90
140.7	3.50
140.1*	--

\*No subharmonic

\*\*Complicated response

†Beating



## REFERENCES

1. Pinson, L. D.; Leonard, H. W.; and Raney, J. P.: Analyses of Longitudinal Dynamics of Launch Vehicles with Application to a 1/10-Scale Saturn V Model. AIAA Journal of Spacecraft and Rockets, Vol. 5, No. 3, March 1968, pp. 303-308.
2. Kana, D. D.; Gormley, J. F.; Garza, L. R.; and Abramson, H. N.: Vibrational Characteristics of a Model Space Vehicle Propellant Tank. Tech. Summary Rept., Part II, Contract No. NAS8-20329, Southwest Research Institute, San Antonio, Texas, January 20, 1967. (Also, Kana, D. D.; and Gormley, J. F.: Longitudinal Vibration of a Model Space Vehicle Propellant Tank. AIAA Journal of Spacecraft and Rockets, Vol. 4, No. 12, December 1967, pp. 1585-1591.)
3. Kana, D. D.; and Craig, R. R., Jr.: Parametric Oscillations of a Longitudinally Excited Cylindrical Shell Containing Liquid. AIAA Journal of Spacecraft and Rockets, Vol. 5, No. 1, January 1968, pp. 13-21.
4. Kana, D. D.: Parametric Oscillations of a Longitudinally Excited Cylindrical Shell Containing Liquid. Final Rept., Internal Project No. 02-1786, Southwest Research Institute, San Antonio, Texas, January 1967. Also Ph.D. Dissertation, University of Texas, January 1967.
5. Bagdasaryan, G. Ye.; Gnuni, V. Ts.: Dynamic Stability of a Closed Anisotropic Cylindrical Shell. Tech. Translation No. 1, Contract No. NAS8-20329, Southwest Research Institute, San Antonio, Texas, November 17, 1967.
6. Grigorev, E. T.: Stability of Longitudinal Oscillations of a Shell with a Liquid. Tech. Translation No. 2, Contract No. NAS8-20329, Southwest Research Institute, San Antonio, Texas, November 17, 1967.
7. Bolotin, V. V.: The Dynamic Stability of Elastic Systems. Holden Day, Inc., San Francisco, 1964.
8. Sanders, J. L., Jr.: Nonlinear Theories for Thin Shells. Q. Appl. Math., Vol. XXI, No. 1, 1963, pp. 21-36.
9. Sanders, J. L., Jr.: An Improved First Approximation Theory for Thin Shells. NASA Rept. 24, June 1959.
10. Bieniek, M. P.; Fan, T. C.; and Lackman, L. M.: Dynamic Stability of Cylindrical Shells. AIAA Jour., Vol. 4, No. 3, March 1966, pp. 495-500.

11. Meadows, H. E.: Solution of Systems of Linear Ordinary Differential Equations with Periodic Coefficients. Bell System Tech. Journal, Vol. 41, July 1962, pp. 1275-1294.
12. Chu, W. H.; and Kana D. D.: A Theory for Nonlinear Transverse Vibrations of a Partially Filled Elastic Tank. AIAA Jour., Vol. 5, No. 10, October 1967, pp. 1828-1835.